Materials Today Sustainability 30 (2025) 101115

Contents lists available at ScienceDirect

Materials Today Sustainability

journal homepage: www.journals.elsevier.com/materials-today-sustainability

BiOX(X=Cl, Br, I)-based S-scheme heterostructure photocatalysts for environmental remediation and energy conversion

Tunde L. Yusuf [a,*], Benjamin O. Orimolade [b], Daniel Masekela [c], Kayode A. Adegoke [d], Kwena D. Modibane [c], Seshibe S. Makgato [e]

[a] Department of Chemistry, Faculty of Natural and Agricultural Sciences, University of Pretoria, Private Bag X20, Hatfield, 0028, Pretoria, South Africa
[b] School of Chemistry, University of Glasgow, Glasgow, UK
[c] Department of Chemistry, University of Limpopo, Sovenga, Polokwane, 0727, South Africa
[d] LAUTECH SDG 11 Sustainable Cities and Communities Research Group, Department of Pure and Applied Chemistry, Ladoke Akintola University, P. M. B. 4000, Ogbomoso, Nigeria
[e] Department of Chemical & Materials Engineering, College of Science, Engineering and Technology, University of South Africa (UNISA), c/o Christiaan de Wet & Pioneer Avenue, Florida Campus Johannesburg, 1710, South Africa

ARTICLE INFO

Keywords:
Photocatalysis
Heterojunction
S-Scheme
BiOX
Energy conversion
Organic and inorganic pollutants

ABSTRACT

Over the past decade, photocatalysis has gained recognition as a powerful tool for environmental remediation and sustainable energy production. Bismuth oxyhalides (BiOX, where X = Cl, Br, I) have attracted particular interest as efficient photocatalysts due to their excellent visible-light harvesting capabilities, straightforward-synthesis, and high photostability. S-scheme heterojunctions have been developed to further improve their performance, which enhances electron-hole separation and significantly increases photocatalytic efficiency. This review examines recent advancements in BiOX-based S-scheme heterostructures, focusing on their diverse applications in pollutant degradation, CO_2 reduction, and H_2 production. An evaluation of the effectiveness, benefits, and limitations of various synthesis methods has been carried out in this article in addition to various strategies to improve the photocatalytic activity of BiOX. This study also compares the suitability of the synthesized methods for removing emerging organic and inorganic pollutants, including dyes, pharmaceuticals, and other contaminants of environmental concern. The performances of various BiOX catalysts for H_2 production and CO_2 conversion to chemicals and fuels were discussed to point out the strengths, weaknesses, and the need for high-performance BiOX catalysts for energy conversion. Also, an analysis of the specific mechanisms driving the photocatalytic activity and strategies to address current challenges have been presented in the article. Finally, this review identifies key knowledge gaps and presents recommendations for scaling BiOX photocatalysts toward large-scale and industrial applications.

1. Introduction

The exponential growth of the world population, coupled with rising water pollution and energy consumption, has led to substantial greenhouse gas emissions, contributing to environmental degradation and climate change. Advanced technologies, including energy conversion, storage, and enhanced water, air, and soil purification, are critical in addressing these global challenges. In recent years, various materials—such as polymers, metal-organic frameworks, zeolites, and activated carbon— have been applied in energy and environmental technology to mitigate these impacts [1,2]. High population density is frequently linked to environmental issues like water scarcity, deforestation, and food shortages. For instance, the typhus epidemic in 1915 caused 150,000 deaths, and the H1N1 Spanish influenza pandemic in 1918 led to 40,000,000 fatalities following World War I [3]. Additionally, industrial sectors, particularly pharmaceuticals, generate significant byproducts, toxic gases, and pollutants, contributing to disease spread and ecosystem contamination. As a result, the world is now grappling with severe energy limitations and escalating levels of pollutants, underscoring the urgent need for innovative materials and methods to remediate pollutants and meet energy demands sustainably.

Photocatalysis is one of the advanced oxidation processes (AOPs) that harnesses solar energy to its maximum capacity and is an efficient approach for tackling worldwide energy scarcity and environmental

* Corresponding author.
E-mail address: yusuf.tl@up.ac.za (T.L. Yusuf).

https://doi.org/10.1016/j.mtsust.2025.101115
Received 10 October 2024; Received in revised form 5 March 2025; Accepted 5 April 2025
Available online 8 April 2025
2589-2347/© 2025 The Authors. Published by Elsevier Ltd. This is an open access article under the CC BY-NC-ND license (http://creativecommons.org/licenses/by-nc-nd/4.0/).

challenges, owing to its properties of being both harmless and non-hazardous or non-toxic byproducts and ecologically beneficial [4,5]. To address the current global need for clean energy and environmental sustainability, photocatalysis is a potential solution that facilitates the production of solar fuel, decreasing CO_2 emissions and mitigating contaminants [6–9]. Therefore, with the ever-increasing human population and urbanization, there is a serious concern about combating challenges such as water pollution and continuous demands for clean energy. Since the 1970s, many semiconductors such as TiO_2, SnO_2, MoS_2, AgBr, CdS, g-C_3N_4, etc., have been produced and demonstrated their promise in diverse applications [4,8,9].

In particular, significant strides have been accomplished in the application of bismuth-based photocatalysts, including bismuth oxyhalides, due to their fascinating properties, such as non-toxicity, low band gap energy, non-complex synthesis routes, and easy modifications. Hence, much literature is available on the use of bismuth-based photocatalysts in wastewater treatments and energy conversion, and these have prompted many authors to present research on their applications [10–16]. Nevertheless, the performance of bismuth halides and other bismuth-based photocatalysts is hindered by some inherent properties of bismuth compounds. For example, these compounds generally have low band gap energy, and this often leads to fast recombination of charge carriers, which hinders the availability of sufficient radicals to oxidise organic pollutants present in water. Consequently, numerous approaches have been implemented to enhance charge separation in bismuth-based photocatalysts. These techniques include nanostructuring, doping, controlling morphology, and creating heterojunctions [17–19]. The construction of heterojunction is especially appealing because other desired properties can also be incorporated into the bismuth-based photocatalysts. The heterojunction can be of different charge separation mechanisms, including Type II, Type-I, Z-scheme, and most recently, the SS-scheme.

Layered materials, including transition metal dichalcogenides, graphene, and boron nitride, often possess a high specific surface area, a greater fraction of exposed surface atoms, and exceptional mechanical and physical properties [20–23]. The distinctive structural characteristics of layered materials make them highly appealing in environmental and energy conversion applications. Bismuth oxyhalides and their derivatives are a type of layered material that exhibit bifunctional properties in the conversion of solar energy through photocatalysis. These materials have an open-crystal structure, a high proportion of catalytically active sites, and are easily modifiable. They also possess good charge separation and mobility properties, as well as exceptional optical and chemical stability. Additionally, they are cost-effective and non-toxic [24]. In addition, the construction of photoelectrocatalytic devices using bismuth oxyhalides is crucial for promoting industrial applications.

Recently, Bismuth oxyhalides (BiOX, X = Cl, Br, and I) have gained remarkable attention as effective photocatalysts under visible light and are extensively utilized in many environmental and energy applications that exploit solar energy. According to the DFT investigations, the Bi 6p orbital can regulate the conduction band (CB), while the O2p and X np (n = 2, 3, 4, and 5) orbitals influence the valence band (VB) of BiOX [25,26]. In addition, the atomic number of X can be increased, causing the peak in the VB of X np density to shift toward the CB of BiOX. Therefore, the band gap diminishes while transitioning from BiOCl to BiOI. The crystal structure of BiOX (Fig. 1) is formed by stacking alternating layers of $[Bi_2O_2]$ slabs and double slabs of halogen, Bi–O, and Bi-X links [27–30]. These bonds are connected by a strong covalent bond and weak van der Waals forces involving X and X [17,31,32]. The layered ultrathin structures of BiOX are primarily formed by van der Waals interactions between BiOX molecules. BiOX has significant photocatalytic activity due to its indirect bandgap (optical transition) and layered crystalline structures [33,34]. This indirect transition refers to the movement of excited electrons in a specific region of k-space, which can slow down the rate at which photo-induced electrons recombine [35,36]. Therefore, BiOX demonstrates highly elevated photocatalytic capabilities.

The growing popularity of BiOX materials has attracted significant attention due to their effectiveness in pollutant removal from water and wastewater, as well as their potential in energy conversion applications. This review explores recent advancements in the use of BiOX materials with step heterojunctions (S-scheme heterojunctions) in photocatalysis. The selection of BiOX for environmental remediation and energy conversion is driven by their dimensional-dependent properties, such as abundant active sites, intrinsic tunability, and suitable microstructures for low-dimensional frameworks. Despite ongoing applications, a comprehensive evaluation of BiOX S-scheme heterojunctions' performance in both remediation and energy conversion remains lacking, highlighting the need for an in-depth assessment of these advancements.

This study reviews the applications and effectiveness of BiOX

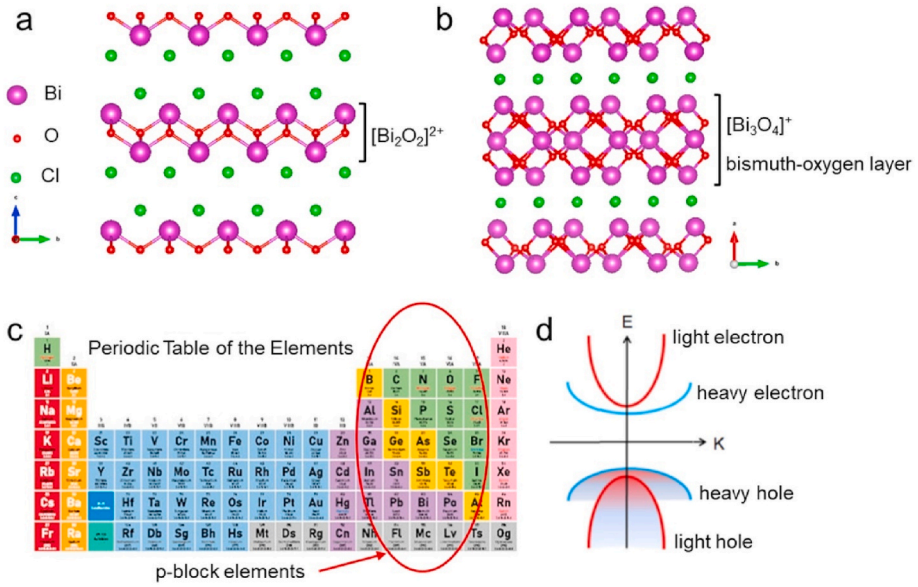


Fig. 1. (a) Diagrammatic representation of the crystal BiOCl structure. (b) Diagrammatic representation of crystal Bi_3O_4Cl structure. (c) The periodic table of elements, highlighting the p-block elements. (d) Illustration depicting the correlation between the geometry of a band and the effective mass of electrons and holes [37].

materials with S-scheme heterojunction in environmental cleaning and energy conversion. An introduction to S-scheme heterojunctions and the porous nature of BiOX is introduced by emphasizing the importance of selecting semiconductors with high reduction or oxidation capacity. Preparation techniques and characterization methods for BiOX s-sheme heterojunction are then discussed, along with the advantages and limitations of current synthesis approaches. The report then examines the remarkable potential of BiOX composites with S-scheme heterojunctions for CO_2 reduction, H_2 production, and the removal of emerging organic and inorganic pollutants, enabling a deeper understanding of their mechanisms and synergistic effects. Furthermore, this review identifies current limitations, strategies for enhancing photocatalytic efficiency, and treatment options, as well as knowledge gaps and directions for scaling BiOX technologies for large-scale or industrial applications.

In essence, the novelty in this review article can be identified from the various theories and technologies identified. This includes a detailed analysis of the strategies to improve the photocatalytic activity of BiOX photocatalysis. The identified strategies discussed in the review include enriching the bismuth, oxygen vacancy, doping, and S-scheme heterojunction, which is the major area of review of this article. To elucidate on the S-scheme heterojunction theory, this article provided details on the preparation of the S-scheme heterojunction of BiOX. The review also provided details on recent advancements in the photodegradation of organic pollutants using BiOX S−scheme heterojunction. To achieve this, various schemes under the S-scheme heterojunction BiOX-based systems (BiOBr, BiOCl, and BiOI) were reviewed to provide details on the performance of these schemes for the remediation of organic pollutants. This article also presented a critical review of the removal of heavy metals using the BiOX S-scheme heterojunction in the photocatalysis process. The review also provided a detailed analysis on the reduction of CO_2 and production of H_2 using the BiOX S-scheme heterojunction which serves as means of energy conversion applications. In conclusion, the review article provides a future perspective in the aspects of design and characterization protocols of charge separation mechanisms and the use of direct sunlight as the light source for photocatalytic applications. Other future perspective includes the application of BiOX-based photocatalysts to real wastewater effluents, and other energy applications, including photocatalytic hydrogen production and CO_2 reduction.

2. Strategies to improve the photocatalytic activity of BiOX

2.1. Enriching the bismuth

The photocatalytic process is greatly influenced by the band edge potentials and reduction/oxidation potentials of the adsorbate. The maximum valence band (VB) and minimum conduction band (CB) energies of BiOX materials may be adjusted by increasing the amount of bismuth (Bi) and oxygen (O) and decreasing the amount of element X. Consequently, the band edge potentials of BiOX materials have been adjusted by changing the amount of Bi to meet the specific potential needs for hydrogen evolution, CO_2 reduction and dye degradation processes. Authors have reported the importance of increasing Bi content in various BiOX photocatalysts [38–44]. Typically, the optical band gap decreases as the amount of Bi increases in BiOBr and BiOCl materials [45]. However, the opposite tendency has been seen for BiOl material. The influence of the Bi content on the band edge locations of 1BiOX may be elucidated in the following manner: (a) BiOCl undergoes a reduction in the lowest energy levels of the conduction band and a rise in the highest energy levels of the valence band. (b) BiOBr experiences an increase in both the lowest energy levels of the conduction band and the highest energy levels of the valence band. (c) BiOI experiences an increase in the lowest energy levels of the conduction band and a decrease in the highest energy levels of the valence band.

Based on the theoretical and experimental understanding of the mechanisms involved, Li et al. [46] have put up a potential bulk-charge separation (BCS) process facilitated by an internal electric field (IEF), as shown in Fig. 2. Initially, IEF facilitated the movement of electrons and holes from the places where they were separated to the [Bi_3O_4] and [Cl] layers of Bi_3O_4Cl. Furthermore, the differences in band alignments between the {010} and {110} facets serve as a catalyst for the movement of individual holes and electrons from the interior of Bi_3O_4Cl to its surface. In this operation, the separated electron and hole were kept between [Bi_3O_4] and [Cl] slices by IEF to prevent their recombinations. A larger IEF allows for increased separation of electron and hole, as well as stronger confinement capability throughout their transfer from the bulk to the surface. This results in high bulk efficiency (ηbulk) and, therefore, more holes and electrons reaching the surface for photocatalytic water oxidation.

2.2. Oxygen vacancy

Oxygen vacancies in semiconductors significantly influence their electrical and optical properties by enabling broad wavelength light absorption and enhancing photocatalytic activity. These vacancies act as electron scavengers, improving charge carrier separation and forming impurity bands that narrow the optical band gap. This promotes electron excitation and increases light absorption. In BiOX materials, oxygen vacancies boost photocatalytic performance. Oxygen vacancies serve as centers that capture photoinduced electrons, so increasing the separation of electron-hole pairs instead of undergoing radiative recombination with valence holes [47,48].

Zhao et al., [27]. demonstrated that BiOCl single-crystalline nanosheets exhibit surface structure-dependent molecular oxygen activation characteristics when exposed to UV radiation (Fig. 3a) [27]. The (001) surface of BiOCl has a preference for reducing O_2 to O_2^- through a one-electron transfer process. On the other hand, the (010) surface tends to facilitate the formation of O_2^{2-} through a two-electron transfer process. This behavior was influenced by the surface atom exposure and the characteristics of the oxygen vacancies generated on the (001) and (010) surfaces under UV light irradiation.

Li et al. [49]. demonstrated that the high concentration of oxygen on the BiOCl {001} facets leads to the rapid formation of oxygen vacancies in ethylene glycol when exposed to microwave radiation (Fig. 13b) [49]. This process allows for the spontaneous formation and development of silver (Ag) on the {001} facets of BiOCl single-crystalline nanosheet. The selective deposition of Ag BiOCl single-crystalline nanosheet demonstrates significantly enhanced reactivity and stability in sodium pentachlorophenate oxidation and Cr(VI) reduction under visible light. This improvement could be attributed to the close contact between the Ag and BiOCl {001} facets, which is achieved through selective deposition of Ag that induces oxygen vacancy.

2.3. Doping

The high recombination rate of photoinduced charge carriers in BiOX limits their photocatalytic efficiency. To improve their capabilities, researchers have focused on adjusting the optical band gap of these materials. A common approach is doping with metal ions, which introduces impurities into the band structure without affecting crystallinity. This doping reduces the optical band gap, extending light absorption to longer wavelengths and enhancing both optical and electrical properties. Additionally, the metal ions act as electron traps, promoting effective electron-hole separation and improving photocatalytic activity. The transition metal dopants introduce acceptor and donor energy levels that are situated below and above the CB and VB of the photocatalyst, respectively. For example, the synthesis of Sn-doped BiOBr materials by the solvothermal process for photocatalysis has been reported [91]. The produced compounds were evaluated for their photocatalytic activity using rhodamine B and bisphenol A as model indicators.

Also, the addition of noble metals to BiOX hinders the recombination

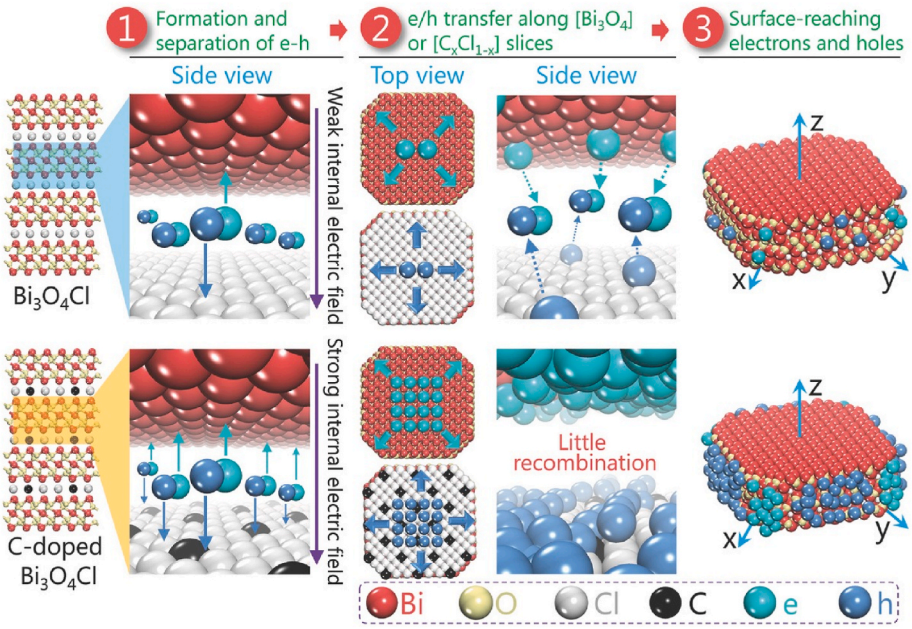


Fig. 2. Schematic illustration of the separation and migration of electrons and holes in the bulk of the pure and C-doped Bi_3O_4Cl [46].

of electron-hole pairs and enhances the photocatalytic activity when exposed to visible light [50]. The metal ions also function as active catalytic centers. Earlier studies indicate that the work function of noble metals is often greater than that of BiOX. As a result, charge carriers go over a Schottky barrier from the conduction band of the photocatalyst to the noble metal, where they are captured. For example, Ag-doped BiOBr photocatalyst has been reported [51]. The enhanced photocatalytic activity of Ag/BiOBr was attributed to its ability to absorb light across a wider range of wavelengths due to the presence of Ag.

Similarly, rare earth elements are considered appropriate dopants for BiOX photocatalysts. The presence of these metal ions greatly enhances the photocatalyst stability by leveraging their redox capacities. Numerous studies have shown the significant photocatalytic effectiveness of BiOX photocatalysts doped with rare earth elements. This is attributed to the crucial function of the rare earth dopants as shallow trap center(s), which enhance the separation of electron-hole pairs and thus enhance the photocatalytic activity. For instance, Saraf and his co-authors prepared nanoflakes of BiOX doped with Eu^{3+} using a microwave-assisted technique [52]. The optical characteristics of both Eu^{3+}-doped BiOBr and BiOCl samples were found to be favorable in the presence of Bi^{3+} and Eu^{3+}. The photocatalytic activity of the BiOX photocatalyst was enhanced by the addition of Eu^{3+}, resulting in increased degradation of rhodamine B dye during visible light exposure, in comparison to the undoped BiOX. The Eu^{3+}-doped BiOCl photocatalyst exhibited complete degradation of rhodamine B dye due to its impressive, layered crystal structure, large surface area, and decreased optical band gap, which resulted in enhanced light absorption.

In another similar study, a colloidal poly(vinyl alcohol) (PVA)-coated europium (Eu^{3+})-doped bismuth oxyhalide (BiOX; X = Cl, Br, I) nanoflakes was prepared [53]. It was observed that the doping of Eu^{3+} with BiOBr and BiOCl nanoflakes have robust optical characteristics associated with Bi^{3+} and Eu^{3+}. However, these features are diminished in the Eu^{3+}-doped BiOI matrix. Furthermore, the photocatalytic performance of Eu^{3+}-doped BiOX (X = Cl, Br, I) nanoflakes have band gaps of 3.36, 2.74, and 1.67 eV, respectively, for rhodamine B dye degradation under visible light exposure (Fig. 4). The nanoflakes demonstrated 100 % degradation of the dye when exposed to visible light. The efficiency of BiOCl nanoflakes doped with Eu^{3+} was greater than that of other matrices. This significant increase in efficiencies may be attributed to their layered crystalline structures, large surface area to volume ratios, indirect band gap nature, and capability to harness wide bands in the solar spectrum.

Non-metals have also been identified as effective BiOX dopants due to their high ionization energy and electronegativity. For instance, sulphur-doped BiOCl has been reporyed [54]. The Sulphur particles were evenly distributed throughout the BiOCl without the formation of separate phases. The results demonstrated that the photocatalytic activity of the S-doped BiOCl photocatalyst was superior to that of pristine BiOCl. The improved photocatalytic activity was ascribed to the improved light absorption and superior segregation of photoinduced electrons and holes. Boron has been utilized to alter BiOBr materials. Apart from sulphur, boron and carbon has been employed for the doping of BiOX [54,55]. Li et al., [56] developed a method for introducing carbon into BiOCl (Fig. 5) [56]. This process entails the initial adsorption of the dopant precursor and is influenced by the surface atomic structure, followed by the diffusion of carbon dopants, which was influenced by the arrangement of bulk atoms on different facets. The carbon doping behavior of BiOCl nanosheets is influenced by the facets, and the conversion of solar energy to hydrogen is reliant on the concentration of dopants. These insights suggest that implanting dopant precursors into the shallow lattices of host nanocrystals is essential for achieving uniform and effective doping. This approach differs from traditional methods that depend on the adsorption of organic ligands or gas molecules on the nanocrystal surface, which often leads to surface-only doping.

2.4. S–Scheme heterojunction

In efforts to boost the photocatalytic efficiency of semiconductor's visible light-response photocatalysts through the reduction of the spontaneous recombination of photogenerated charge carriers, the formation of heterojunctions has shown to be successful. Typically, a semiconductor-semiconductor heterojunction is created by combining two different semiconductors with mismatched band gaps. This combination aligns the bands of the two semiconductors to facilitate charge separation [57]. Heterojunctions are generally classified based on the mechanism of charge separation, and accordingly, they include the Type I, conventional Type II, Z-scheme, and S–Scheme [58–60]. The mechanism of charge separation within these heterojunctions is illustrated in Fig. 6. The Type-II heterojunction gained much attention from the onset

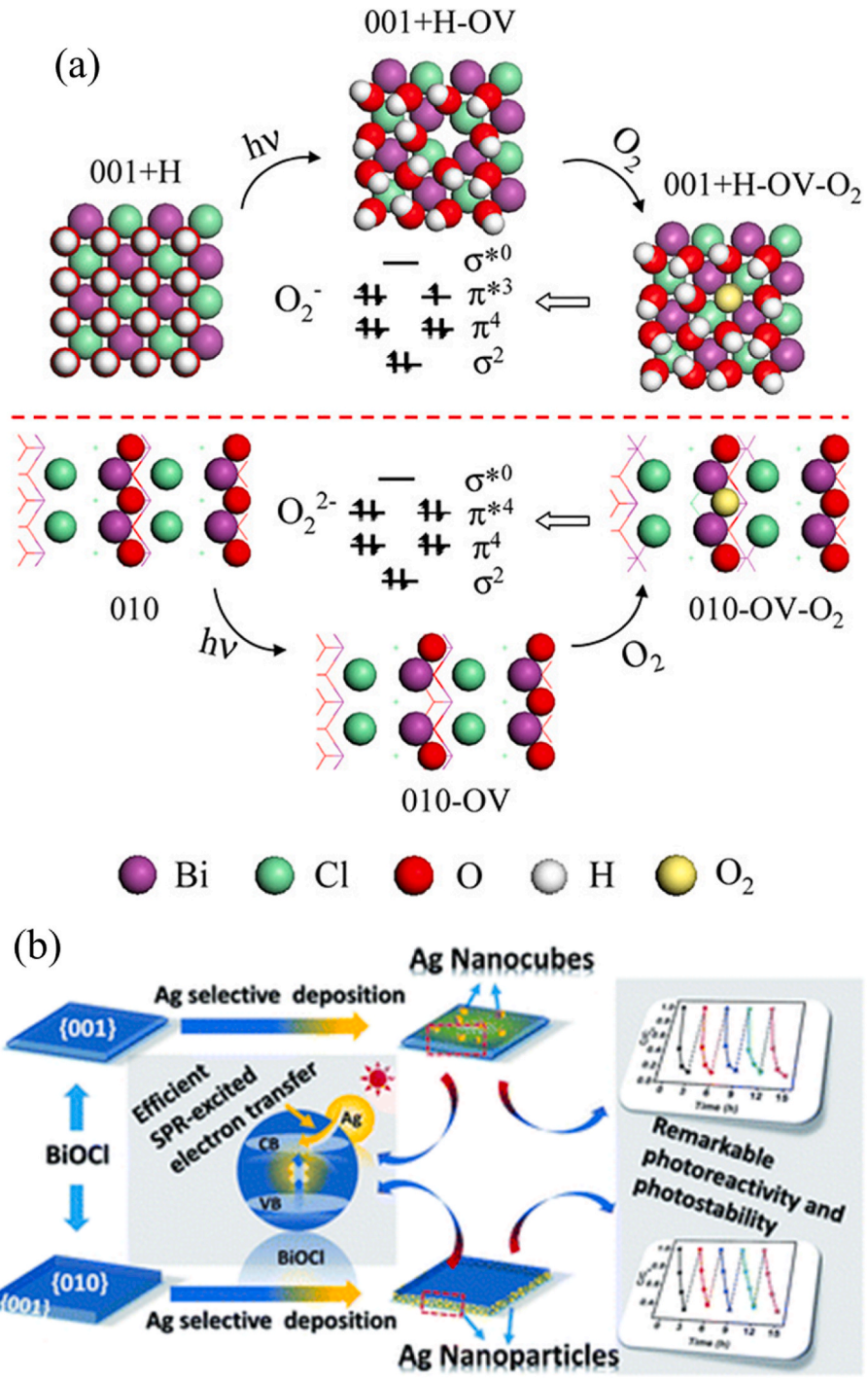


Fig. 3. (a) Proposed molecular oxygen activation processes on BOC-001 and BOC-010 surfaces [27] (b) Ag deposition on the {001} facets of BiOCl single-crystalline nanosheet enhanced photocatalytic activities [49].

because it offers efficient charge separation. After all, holes and electrons are separated into valence bands and conduction bands of two different semiconductors that form the heterojunction. However, Type II heterojunctions are limited, and some systems cannot fully explain the charge separation mechanism. In a Type II heterojunction, electrons transfer from a conduction band (CB) with a higher reduction potential to another CB with a lower one. In contrast, holes move in the opposite direction. Although this arrangement effectively reduces the quick recombination of charge carriers, it results in electron-hole pairs possessing weaker redox potentials, rendering them less suitable for highly active photocatalytic reactions [61,62]. Moreover, attaining a continuous transfer of the carrier is challenging because of the potent Coulomb forces between charges having similar electrical properties. To address the shortcomings of Type II heterojunctions, the Z-scheme heterojunction system has been developed. Based on the compositional characteristics of the photocatalytic system, it can be classified into three types: the conventional Z-scheme, the all-solid Z-scheme, and the direct Z-scheme. [63–65]. Z-scheme heterojunction shares an energy band structure identical to type-II, but the carrier migration paths for these two types of heterojunction differ significantly [66]. However, in some reported traditional Z-scheme heterojunctions, the electron transfer did not thermodynamically follow the Z-scheme pathway,

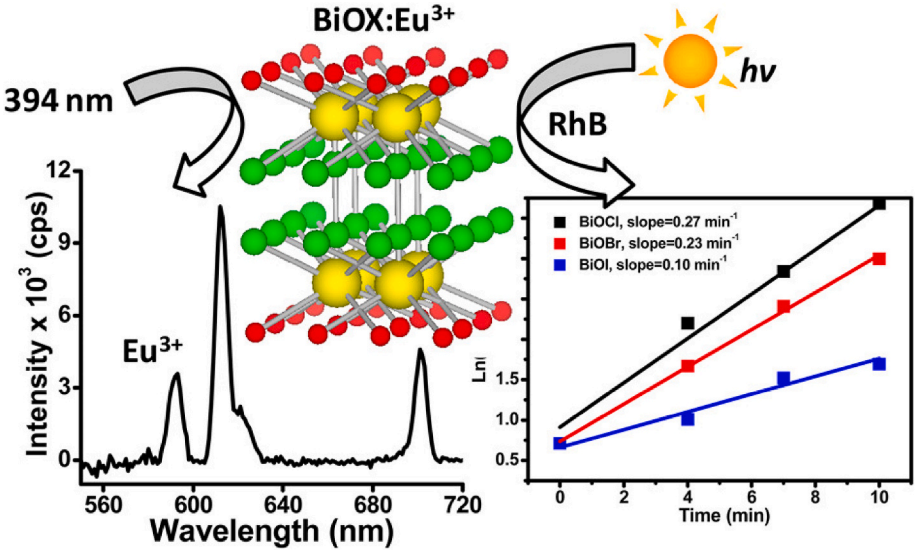


Fig. 4. Photodegradation of rhodamine B dye by Eu^{3+}-doped BiOX (X = Cl, Br, I) nanoflakes [53].

leaving its charge transfer mechanism poorly understood. [67,68]. To remove the confusion and describe the photocatalytic mechanism fittingly in Z-scheme heterojunctions, Yu's group first reported a novel S–S-scheme mechanism [69].

Generally, an S–S scheme heterojunction consists of two related catalysts: oxidation photocatalysts (OP) and reduction photocatalysts (RP) (Fig. 7). The former possesses a higher Fermi CB and VB level than the latter. Since the Fermi levels in the two photocatalysts are dissimilar, the electron in RP readily migrates to the OP to achieve an equal Fermi level at the interface. An internal electric field (IEF) is generated at the interface between the OP and RP sides due to electron movement. This migration generates a positive charge on the RP face but a negative charge on the OP face, causing the IEF to be pointed through RP to the OP. The CB and VB of reverse-biased p-n junctions curve in an upward direction due to the generation of a depleting electron region. Conversely, the CB and VB of the object of interest (OP) exhibit opposite bending orientations due to the generation of an electron's accumulating zone. Upon exposure to suitable light, the electrons in these photocatalysts undergo photoexcitation, transitioning from the VB to the CB. This promotes the photogenerated electron transfers across the CB of the OP to that VB of the receiving material (RP) for recombing with the hole, facilitated by the IEF. Electrostatic attraction and band bending facilitate the recombination of those non-functional holes and electrons. On the other hand, the phenomena of IEF and electrostatic attraction band bending facilitate the electron movement in the CB of the RP and VB hole of the OP through its interior towards the surface. Therefore, these important holes and electrons are separated spatially, resulting in a system having optimized oxidation and reduction capacity. The electron transfer generated by light in the S-scheme heterojunction may be described as a "step" from a macroscopic perspective or as an "N" type from a microscopic point of view [70]. The "S-scheme heterojunction" involves interfacial electron transfer from the RP to the OP upon their contact and the photogenerated electron transfer from the OP to the RP when exposed to light. Significantly, this S-scheme configuration enhances redox capability and mitigates charge recombination. Throughout the photocatalytic process, the generation of reactive oxygen species (ROS) is influenced by the redox potential of the photocatalyst [67]. Leveraging the S-scheme charge transfer in heterojunction is advantageous for achieving highly effective environmental purification via photocatalysis. This involves retaining photoexcited electrons in the reduction photocatalyst (RP) and holes in the oxidation photocatalyst (OP), both possessing robust photo-redox capabilities. It is essential to carefully choose semiconductor material(s) with potent reduction or oxidation capacity for constructing S-scheme heterojunction to ensure an efficient photocatalytic reaction.

3. Preparation of S–Scheme heterojunctions of BiOX

Bismuth oxyhalide (BiOX) has garnered significant attention for its distinctive layered structures and exceptional charged carrier characteristics. The material's structure is characterized by a tetragonal magnesia-olivine mesocrystal arrangement (PbFCl type), comprising a [Bi–O] layer intertwined with halogen layers forming atomic layer(s), producing the precise crystal structure depicted in Fig. 8 [71]. The exceptional structural crystal properties of BiOX stem from the dominance of hybrid O 2p orbitals and Bi 6s in the valence band of Bi-based compound(s), with the CB primarily constituted by Bi 6p orbitals. This arrangement gives rise to internal electrostatic force and indirect optical transitions, constraining the excited hole and electron complexes. According to Density Functional Theory (DFT) calculation, the upper VB of BiOX is chiefly shaped by the hybridization of O 2p orbital and X np orbital (where n = 3, 4, and 5 for X = Br,Cl, and I). In contrast, the low CB predominantly comprises Bi 6p orbital [72].

BiOX (X = Cl, Br, and I) possesses a modifiable band gap, which sets it apart from traditional photocatalysts like ZnO and TiO_2. Out of the BiOX photocatalysts, BiOCl can be stimulated by UV photons due to its broad appropriate energy band (~3.20 eV). BiOI has a band gap of around 1.76 eV, allowing it to be triggered by visible light. On the other hand, BiOBr has a band gap of ~2.63 eV, suggesting its strong ability to facilitate reduction and oxidation reactions by photocatalysis [71,73].

In the furtherance of research on BiOX materials may be synthesized using various processes and by controlling the conditions of reactions to get materials with distinct shape, size, crystallinity and morphology, hence enhancing their photocatalytic capabilities. BiOX and their heterojunctions are often prepared through hydrothermal synthesis, electrodeposition, co-precipitation, and wet chemical precipitation. Typically, in a study reported by Dou et al., [74]. where a BiOBr/Cu_2O containing S–scheme heterojunction was prepared, the BiOBr was first prepared through hydrothermal synthesis. This was done by preparing a precursor solution containing $Bi(NO_3)_3{\cdot}5H_2O$ and KBr at pH 9. The solution was then transferred into a Teflon-lined autoclave and heated at 160 °C for 16 h. The obtained BiOBr was washed with deionized water and dried to obtain fine powders. For the heterojunction, BiOBr was dispersed in deionized water, and specific quantities of copper chloride dihydrate ($CuCl_2{\cdot}2H_2O$), NaOH, and ascorbic acid were added under continuous stirring. The BiOBr/Cu_2O was obtained after 30 min, after

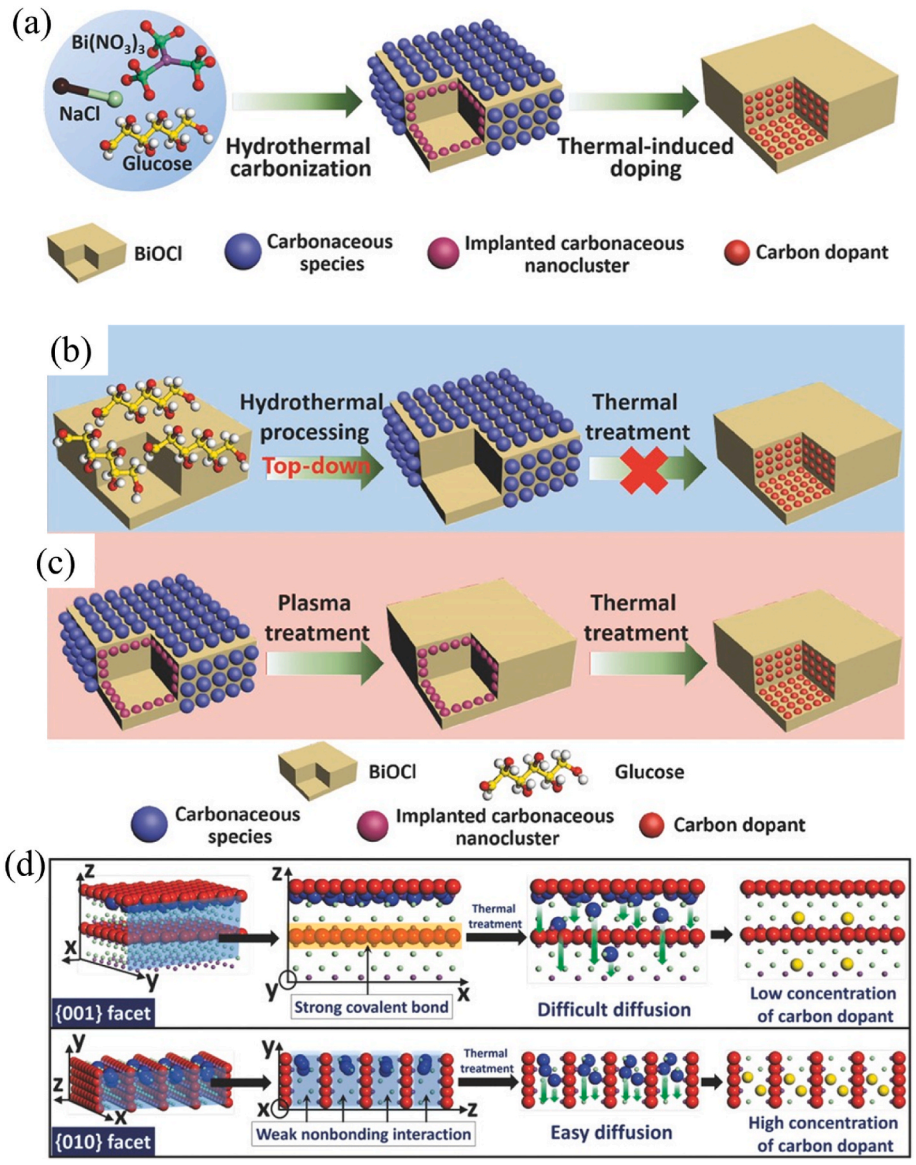


Fig. 5. (a) Schematic illustration of homogeneous carbon doping strategy comprised of bottom-up hydrothermal processing and subsequent thermal treatment with taking carbon doped BiOCl as the example. (b) Exploration of the contribution of surface modified carbonaceous species to carbon doping. (c) Elucidation of the role of implanted carbonaceous nanoclusters during carbon doping. (d) Schematic illustration of the detailed carbon doping process of {001}- and {010}-faceted BiOCl accounting for the role of facet-related arrangement of bulk atom on the diffusion and concentration of carbon dopant [56].

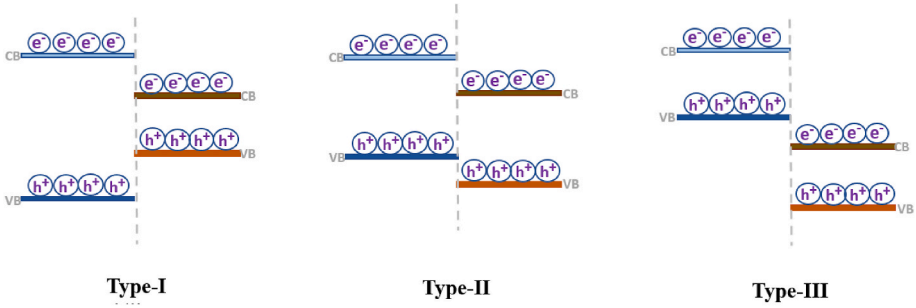


Fig. 6. Typical interface of different types of heterojunctions.

which it was washed and dried. The SEM images of the prepared materials revealed a flower-like nature of BiOBr and cubic particles of Cu_2O. Contrary, in a study involving BiOBr/g-C_3N_4 S−scheme heterojunction [75], the g-C_3N_4 was prepared first and subsequently introduced into the precursor solution for BiOBr, which contained Bi$(NO_3)_3{\cdot}5H_2O$ and cetyltrimethylammonium bromide (CTAB). The hydrothermal reaction was then carried out in an autoclave at 160 °C for 12 h. The HR-TEM of the composite revealed the g-C_3N_4 composed of an

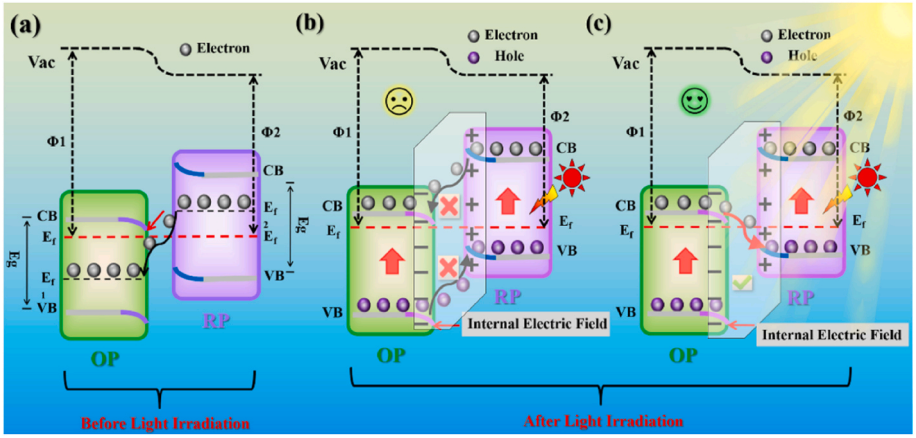


Fig. 7. A typical process of S-scheme formation and the charge transfer within the system (Reproduced with permission from Ref. [66]. Copyright Elsevier 2024).

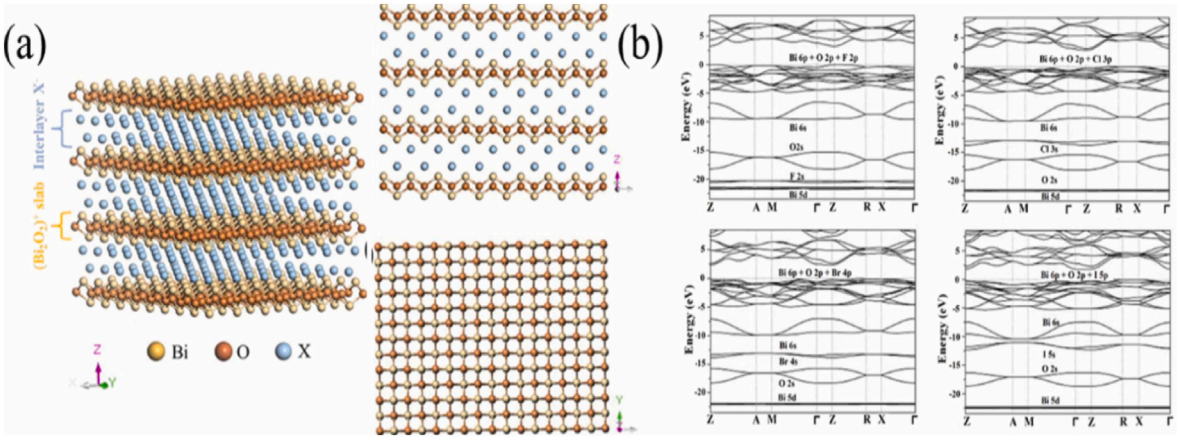


Fig. 8. (a) Crystal structure and (b) energy band distribution of BiOX (Reproduced with permission from Ref. [71]. Copyright Elsevier 2023).

irregular block formed by stacking many nanosheets, and the BiOBr particles were dispersed on its surface, confirming the successful formation of the heterojunction. In another study conducted by Zhang et al., [76], a facile in situ hydrothermal method was employed for the preparation of S−scheme heterojunction of BiOBr and protonated g-C_3N_4 (BiOBr/pCN). As shown in Fig. 9, the g-C_3N_4 was firstly obtained from the calcination of melamine and then protonated by the addition of nitric acid at 80 °C for 4 h. To obtain the heterojunction, a solution containing KBr, pCN, citric acid, and polyvinyl pyrrolidone (PVP) was prepared and stirred for 30 min at 80 °C. Then, a solution of Bi $(NO_3)_3{\cdot}5H_2O$ was added in a drop-wise manner, and the stirring was maintained for an additional 3 h. The composite obtained was then washed and dried. The TEM images showed that the solid spherical particles of BiOBr were formed on the lamellar structure of pCN. A similar in situ hydrothermal approach has been employed for the preparation of S-scheme heterojunctions of BiOCl/g-C_3N_4 [77].

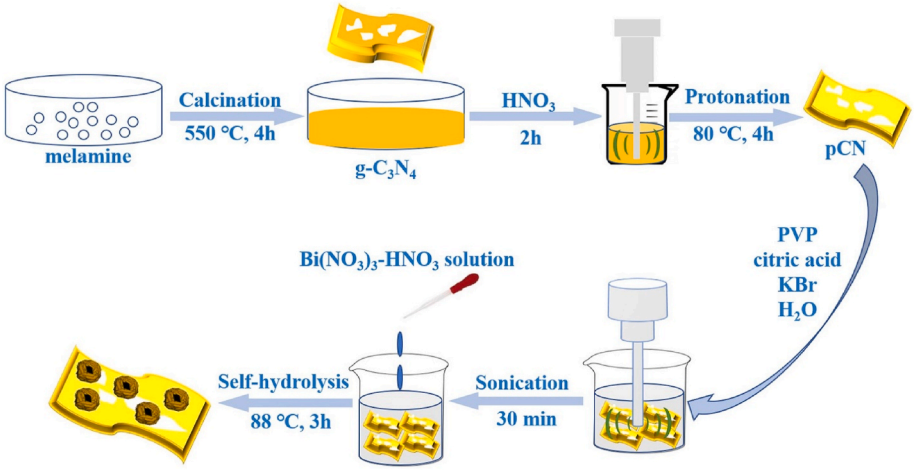


Fig. 9. Synthesis route for the preparation of BiOBr/pCN (Reproduced with permission from Ref. [76]. Copyright Elsevier 2021).

4. Recent advances in the photodegradation of organic pollutants using BiOX S–scheme heterojunction

Water pollution caused by organic contaminants is a pressing environmental issue with far-reaching consequences. The discharge of these pollutants into water bodies, stemming from agricultural runoff, industrial processes, and improper waste disposal, poses a significant threat to aquatic ecosystems. These contaminants include pesticides, fertilizers, and organic chemicals, which lead to various detrimental effects. Organic pollutants can alter water quality, disrupting the delicate balance of aquatic ecosystems and endangering marine life [78,79]. For example, excessive nutrients from organic sources can trigger algal blooms, depleting oxygen levels and causing the death of fish and other aquatic organisms [80]. Furthermore, some organic contaminants, such as pharmaceuticals and personal care products, can persist in water bodies, affecting wildlife and human health [81–83]. The widespread use of synthetic chemicals in agriculture and industry exacerbates the problem, as these substances find their way into water sources and accumulate over time [84,85]. Not only does contaminated water threaten biodiversity, but it also jeopardises the safety of drinking water for human consumption [86,87]. Addressing the issue of water pollution by organic contaminants requires concerted efforts in regulation, sustainable practices, and public awareness to ensure the preservation of clean and healthy water resources for future generations.

Tackling the issue of water pollution due to the presence of organic contaminants necessitates a comprehensive and concerted effort. A multi-faceted approach that combines regulatory measures, technological advancements, public education, and research initiatives is essential to effectively tackle the problem of water pollution by organic contaminants and make clean water available for use. Additionally, promoting the use of eco-friendly alternatives and developing biodegradable products can help curb the release of harmful substances into water sources [88–90]. Investing in advanced wastewater treatment technologies is essential to effectively remove organic contaminants before discharging treated water into the environment. This is crucial because conventional wastewater treatment options have proven unsuitable for removing these organic pollutants [87,91]. The intricate and diverse characteristics of organic pollutants add to the constraints of conventional wastewater treatment approaches[92–94]. Also, the persistence of certain organic pollutants poses a significant challenge, as conventional methods may not adequately break down or eliminate these substances, leading to their release into receiving water bodies [95,96]. Moreover, conventional treatments often require extensive energy consumption, making them environmentally taxing and economically burdensome [97–99]. Hence, greater attention has been focused on developing other treatment options, such as advanced oxidation processes (AOPs), and photocatalysis is a prominent example of these processes.

Heterogeneous photocatalysis, an AOP, whereby powerful oxidants, majorly hydroxyl radicals generated in situ, are used to mineralise organic molecules, has shown excellent prospects as a suitable approach for treating wastewater contaminated with organic pollutants [100–102]. Tremendous efforts have been dedicated to this technique in recent years. The application of photocatalysis is not exclusive to the degradation of organic pollutants in aqueous solution as the process is widely applied for energy generation through water splitting and also the reduction of carbon dioxide [103–106]. However, the success of photocatalysis in wastewater treatment and other applications largely depends on the properties and performance of the photocatalyst employed. Hence, to improve the efficiency of the photocatalysis system, many considerations have been given to the development of novel photocatalysts or improving the existing ones using different strategies. For example, the integration of advanced nanotechnology has facilitated the design of photocatalysts with increased surface area and enhanced light absorption, contributing to higher efficiency in pollutant removal [107,108].

Likewise, tailoring the band structures of photocatalysts has become a focus, allowing for the utilization of a broader spectrum of light, including visible light, thereby enhancing the photocatalytic process. Interestingly, the use of visible light responsive photocatalysts which could be metal oxides or metal chalcogenides such as $BiVO_4$ [109], WO_3 [110,111], Bi_2WO_6 [112], Cu_2O [113], CuS [114], CdS [115], MoS_2 [116–118], Ag_2S [119,120], Fe_3O_4 [121] have become popular in recent years. This is because the use of these photocatalysts could significantly reduce the cost associated with the photocatalysis system, as direct sunlight could be used to facilitate the process.

4.1. Application of BiOBr-based S-scheme heterojunctions for organic pollutants remediation

In the pool of numerous photocatalysts, BiOBr has been identified as a unique photocatalyst that can be employed either in the pristine form, doped, or in a composite for the degradation of myriads of organic contaminants in aqueous media. Among bismuth oxyhalides, BIOBr exhibits a broader spectrum of sensitivity to visible light, possesses a greater quantum efficiency, and demonstrates superior conductivity [122–124]. Nevertheless, most recent studies on BiOBr photocatalysts focused on their use in composite form. Hence, it is not surprising that many S–scheme heterostructured photocatalysts involving BiOBr have been prepared and successfully deployed for the quick removal of pharmaceuticals, dyes, pesticides, and phenols from contaminated aqueous systems. For example, Fan et al. report the use of BiOBr/AgBr photocatalyst consisting of S–scheme heterojunction for the removal of carbamazepine, a pharmaceutical compound for treating epilepsy [125]. The composite photocatalyst was prepared through the facile water bath precipitation method. The introduction of AgBr into BiOBr significantly increased its visible light absorption, suggesting the formation of heterojunction. Specifically, the absorption edge of the pristine BiOBr was 440 nm, while the BiOBr/AgBr heterojunction recorded 487 nm. Also, the fluorescence emission peak intensity of the composite is lower than that of the pristine, which further confirmed the formation of heterojunction, which could promote efficient charge separation and impede recombination rate. As envisaged, the BiOBr/AgBr achieved better photocatalytic removal of carbamazepine within 2 h with a percentage removal of 99.64 %, which is significantly higher than that obtained with pristine BiOBr (65.92 %). The enhanced performance was attributed to the formation of an S-scheme heterojunction formed between BiOBr and AgBr, which resulted in accelerated charge separation and transfer. The mechanism of the charge separation and transfer through the S-scheme heterojunction is shown in Fig. 10.

Similarly, BiOBr/AgBr was successfully used for the photocatalytic removal of sulfisoxazole antibiotic (Fig. 10b–g) [126]. The composite photocatalyst was prepared through in situ hydrothermal method. The composite showed the highest transient photocurrent response and lower interfacial transfer resistance than pristine BiOBr and AgBr, which revealed the formation of the S-scheme heterojunction. The formation of the S–scheme heterojunction was further confirmed through a photoluminescence experiment. The heterostructured photocatalyst achieved more than twice the removal of the pharmaceutical within 15 min than pure BiOBr. The kinetic rate constant was also more than 70 times that of BiOBr (Fig. 10b–g). The formation of the S-scheme heterojunction in the BiOBr/AgBr photocatalyst is ideal for the removal of pharmaceuticals.

Another pharmaceutical that has been successfully degraded using BiOBr-based S-scheme heterojunction is tetracycline. For example, Zhang et al., [127]. reported the efficient degradation of tetracycline antibiotic using S–scheme $BiOBr/WO_3$. The heterostructured photocatalyst was prepared through one-pot hydrothermal synthesis without the addition of any surfactant. The composite showed a 3D hierarchical structure, and the presence of WO_3 caused surface roughness, which was associated with a decrease in the compactness of BiOBr nanosheets, resulting in larger pore sizes of the composite photocatalyst. The effect of the formation of S-scheme heterojunction was seen in the optical

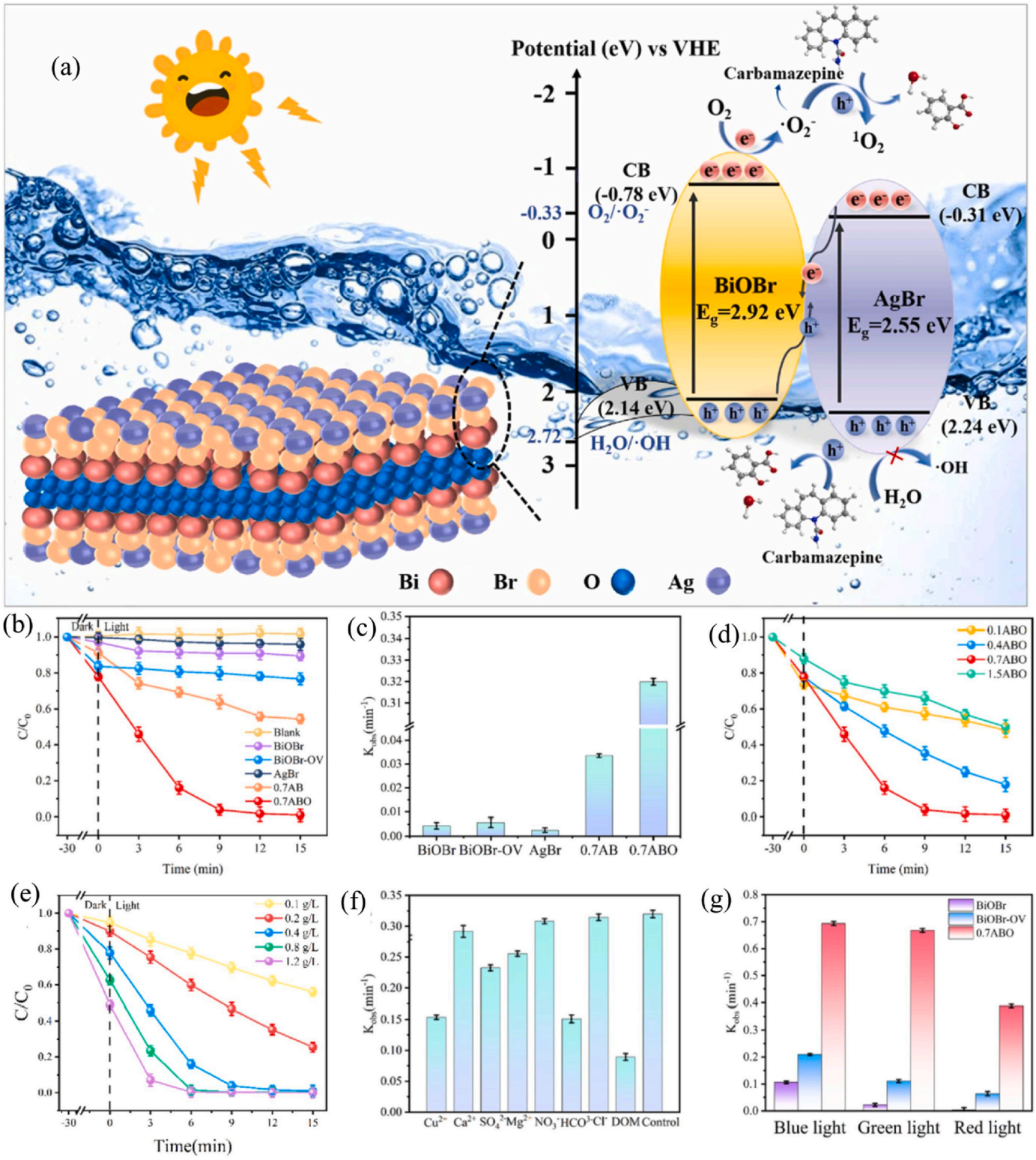


Fig. 10. (a) Proposed mechanism of degradation of carbamazepine using S-Scheme BiOBr/AgBr (Reproduced with permission from Ref. [125]. Copyright Elsevier 2023). (b) Photocatalytic degradations curve of different samples under visible irradiation; (c) Kinetic rate constants of SIZ decomposition with various photocatalysts under visible light; (d) Effects of various catalysts; (e) Effects of 0.7ABO dosage on degradability of SIZ; (f) Effects of photocatalytic activity of SIZ under different substances; (g) Kinetic rate constant for the decomposition of SIZ at various wavelength [126].

measurements, where the $BiOBr/WO_3$ had the highest absorption intensity and absorption edge (470 nm). Also, lower photoluminescence (PL) intensity was noted with the $BiOBr/WO_3$, suggesting efficient charge separation, and this was supported by the increase in charge transfer resistance recorded with electrochemical impedance spectroscopy (EIS). The improved charge separation in the S–scheme $BiOBr/WO_3$ heterostructure photocatalyst led to the removal efficiency of 100 % for tetracycline in 50 min, and this was exceedingly higher than

the performance of pure BiOBr. A similar performance was reported by Liu et al., where S−scheme $BiOBr/WO_3$ heterojunction achieved 98 % removal of tetracycline in 60 min in the presence of peroxymonosulfate [128]. The composite photocatalyst was also prepared through hydrothermal synthesis. It was equally observed that the $BiOBr/WO_3$ showed lower PL intensity and higher visible light absorption due to the efficient separation of electron and hole pairs within the S−scheme heterojunction. Other common BiOBr-based S-scheme heterostructured photocatalysts that have been employed for the mineralization of tetracycline include $BiOBr/Zn_2In_2S_5$ [129], BiOBr/black phosphorous (BP) [130], and $BiOBr/CuBi_2O_4$ [131].

Enhanced photocatalytic degradation of organic dyes has also been reported with the use of BiOBr-based S-scheme heterojunctions. A typical case was reported by Kokilavani et al. [132], involving the use of $BiOBr/Ag_3PO_4$ for the removal of methyl orange and malachite green in the presence of visible light. The heterostructured photocatalyst was synthesized through the direct solution precipitation method. The morphology study revealed the presence of Ag_3PO_4 nanospheres on the BiOBr nanoflowers (Fig. 11a–d). The formation of the heterojunction was evident through the lower PL intensity recorded and smaller arc radius on EIS recorded with $BiOBr/Ag_3PO_4$ (Fig. 11e–f). The synthesized heterostructured composite achieved significant photocatalytic degradation of the dyes within 200 min. Specifically, the percentage removal was 93.4% and 99.8% for malachite green and methyl orange, respectively, with corresponding high rate constants. The results obtained were approximately twice that of using BiOBr alone, and this further confirmed the superiority of the S-scheme heterojunction in enhancing photocatalytic performance. Additionally, improved photocatalytic removal of rhodamine B dye has also been recorded with the use of S-scheme heterojunction of $BiOBr/g\text{-}C_3N_4$ [133] and $BiOBr/In_2O_3$ [134].

4.2. *Application of BiOCl-based S-scheme heterojunctions for organic pollutants remediation*

Bismuth oxychloride (BiOCl) is another popular bismuth-based photocatalyst. BiOCl has attracted huge research interest in the field of photocatalysis because of its low toxicity, outstanding photocatalytic properties, exceptional photoluminescence, and high chemical stability [33,135,136]. However, the optimal photocatalytic activity of this material is attained when exposed to UV light, which constitutes <5 % of the solar spectrum, owing to its significant band gap of around 3.0 V [137,138]. Furthermore, it suffers from a fast recombination of electron-hole pairs.

However, the formation of heterojunction has been identified as a viable approach to improve its performance. Appropriate materials have been incorporated with BiOCl to form an S-scheme heterojunction photocatalyst with enhanced efficiency. Such composites have been employed for the photocatalytic degradation of organic pollutants in water. For example, the photocatalytic removal of tetracycline using S−scheme BiOCl/CdS composite has been reported [139]. The heterostructured composite was prepared through hydrothermal synthesis

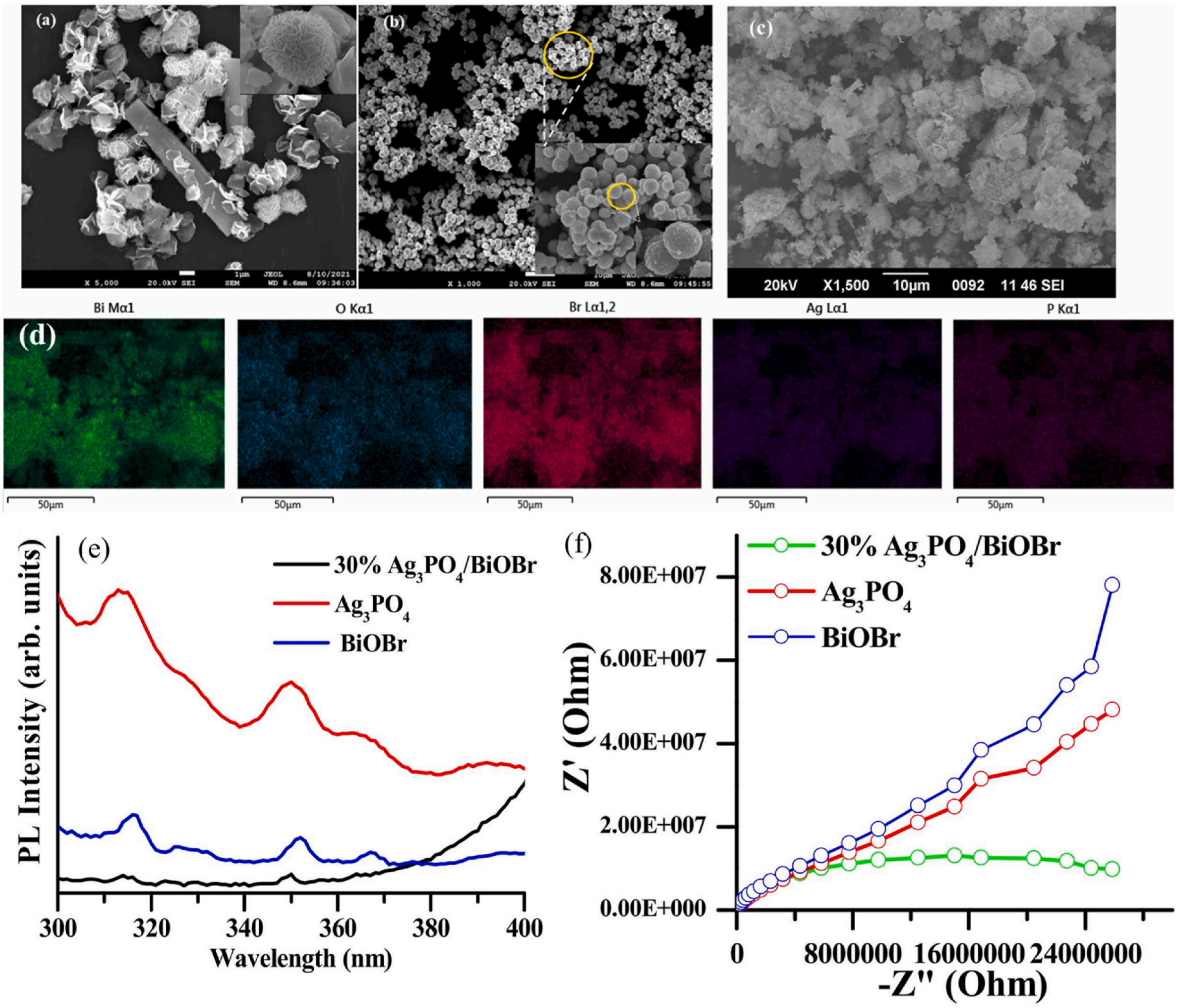


Fig. 11. SEM image of (a) BiOBr(b) Ag_3PO_4 (c) BB/30 % AgP (d) Elemental mapping of 30 % BB/AgP, (e) PL and EIS spectra for $BiOBr/Ag_3PO_4$ (Reproduced with permission from Ref. [132]. Copyright Elsevier 2022).

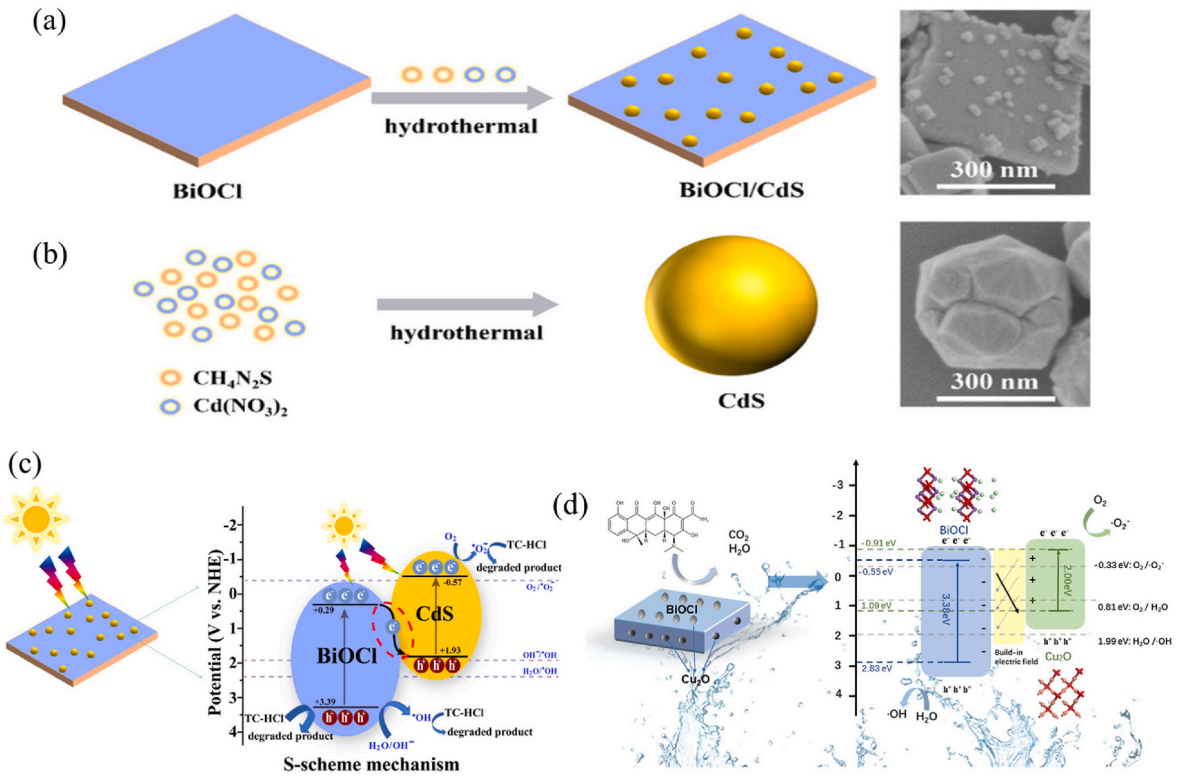


Fig. 12. (a Schematic preparation process of; (a) BiOCl/CdS and (b) CdS, (c) Schematic representation of photocatalytic mechanism for BOC/CdS-3 composite, (d) schematic diagram of electron-hole separation and transfer mechanism in BiOCl/Cu_2O S−scheme heterojunction (Reproduced with permission from Ref. [140]. Copyright Elsevier 2022).

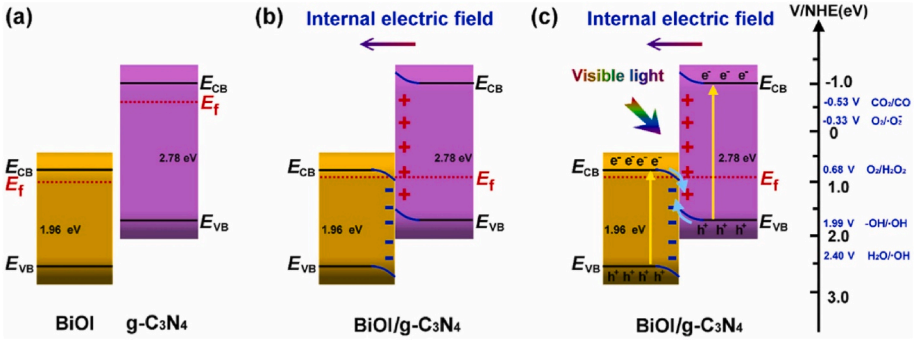


Fig. 13. (a) The band gap of BiOI and g-C_3N_4 before contact; (b) The internal electric field and band edge bending at the interface of BiOI/g-C_3N_4 after contact; (c) The mechanism of charge carrier transfer in the BiOI/g-C_3N_4 S-scheme heterojunction (Reproduced with permission from Ref. [145]. Copyright Elsevier 2022″).

(Fig. 12a), and the morphology studies revealed that the nanoparticles of CdS were successfully immobilized onto the BiOCl square-like nanosheets. The presence of CdS in the composite significantly promotes the absorption edge of the BiOCl, which made the composite photocatalysts responsive to visible light, and this revealed the formation of heterojunction. The formation of heterojunction was further confirmed through the improved photocurrent response and reduced charge transfer resistance of the composite. Upon application for the photocatalytic removal of tetracycline, the pristine BiOCl performed poorly under visible light, while 75 % removal of the pharmaceutical was achieved within 100 min using the composite photocatalyst. Additionally, the degradation rate using BiOCl/CdS was almost five and three times more than using pure CdS and BiOCl, respectively. The enhanced efficiency was linked to the charge separation through the formation of S−scheme heterojunction.

In a similar study involving the removal of tetracycline, BiOCl/Cu_2O with an S-scheme heterojunction was employed, and 90% photocatalytic removal was achieved in 80 min [140]. As shown in Fig. 12, the mechanism of charge separation involved electrons mobilizing to the conduction band of Cu_2O and holes moving to the valence band of BiOCl through an S−scheme route and led to the generation of more oxidizing radicals and, consequently, higher photocatalytic efficiency.

Another S-scheme heterojunction of BiOCl-based photocatalyst materials employed for the mineralization of pharmaceuticals is the BiOCl/In_2O_3 [141]. The S−scheme heterojunction composite photocatalyst was prepared through the molten salt method, and the amount of In_2O_3 in the composite was optimized. The morphology of the composite demonstrated that the In_2O_3 irregular nanoparticles were distributed on the surface of the 2D sheet-like BiOCl photocatalyst. Enhancing the catalytic efficiency was found to depend on the amount of In_2O_3 in the composite, and the composite with 20 % In_2O_3 was observed to offer the best efficiency. The highest photo-current response and minimal achieved with the composite was attributed to the enhanced charge

separation and transfer through the formation of S−scheme heterojunction. The composite achieved 91 % removal of ciprofloxacin within 35 min, and the rate was found to be 3.1 times faster than using pristine BiOCl. Similar trends have also been reported with the degradation of diclofenac using BiOCl/$CuBi_2O_4$ S−scheme heterojunction composite [142]. The composite was prepared through a solvothermal route without any surfactant. The percentage photocatalytic removal of the pharmaceuticals was 18 % and 90 % within 90 min using pristine BiOCl and BiOCl/$CuBi_2O_4$, respectively. Efficient charge separation through the heterojunction was responsible for the significantly higher value recorded with the composite.

BiOCl-based S-scheme heterojunction composites have also been applied for the photocatalytic degradation of organic dyes. For example, Gogoi et al. investigated the removal of rhodamine B dye using BiOCl–LaOCl S−scheme heterostructured photocatalyst [143]. The composite was prepared through the precipitation method. The SEM images revealed that the composite had hierarchical flower-like microspheres with nanosheets, and LaOCl nanoparticles were agglomerated on the surface of BiOCl. Evidence of successful formation of heterojunction was confirmed through reduced PL intensity noted with BiOCl/LaOCl composite. The degradation efficiency of rhodamine B using the composite was 98.78% within 30 min and was more than twice that of using pristine BiOCl (46.96 %). The enhanced efficiency was linked to the synergistic effect between BiOCl and LaOCl, which resulted in efficient charge separation and better visible light harvesting through the S-scheme heterojunction. This significant photocatalytic performance was also similar to the report by Guo et al. where a BiOCl/FeOCl S−scheme heterostructured composite achieved 91% removal of rhodamine B within 60 min [144]. BiOCl-based S-scheme heterostructured photocatalysts are good candidates for the treatment of organic dye-polluted water.

4.3. Application of BiOI-based S-scheme heterojunctions for organic pollutants remediation

Bismuth oxyiodide (BiOI) is a bismuth-based semiconductor photocatalyst, and its visible light response owing lower band energy gap (1.77–2.0 eV). It has a lamellar structure, low toxicity, and good photostability. It has found wide applications in photocatalysis and photoelectrochemical systems. Just like other bismuth oxyhalides, BiOI has a spontaneous recombination problem involving the photogenerated charge carrier, and this seriously limits its photocatalytic efficiency. Hence, it is often used in heterostructured composites for better performance. There have been giant strides in the application of BiOI-based S−scheme heterostructured composites for the photocatalytic degradation of organics in contaminated water. For example, Li et al. reported the degradation of tetracycline and p-chlorophenol using BiOI/g-C_3N_4 S−scheme heterostructured photocatalyst [145]. The composite was prepared through an electrostatic self-assembly process, which involved stirring at 40 °C for 5 h. The morphology of the BiOI in the composite was observed as a nanoplate, while the g-C_3N_4 displayed an irregular lamellar structure. A distinct reduction in the rapid recombination of photo-induced charge carriers was achieved, as noted in the photocurrent response measurement. The composite photocatalyst photocurrent was about 4 times higher than that of pristine BiOI. This was associated with the charge separation through the S-scheme heterojunction. The mechanism of this charge separation is illustrated in Fig. 13. It can be seen that after contact, an internal electric field was generated, and the separation of the charges occurred through the S−scheme route. Consequently, the composite photocatalyst achieved higher removal of tetracycline (100%) and p-chlorophenol (46%) than using the pristine BiOI. In a similar study, 90% photocatalytic removal of tetracycline was achieved using an S-scheme BiOI/g-C_3N_4 heterostructured composite prepared through hydrothermal synthesis [146]. Also, BiOI/g-C_3N_4 has been successfully employed for the removal of bisphenol A through photocatalysis [147]. These findings established the efficiency of BiOI/g-C_3N_4 S-scheme heterojunction in eliminating a wide range of organic pollutants. Table 1 presents the studies on the application of BiOX-based S-scheme heterojunction for photocatalytic degradation of organic pollutant.

The catalytic activity of BiOI-based S-scheme heterostructured materials for the efficient photodegradation of various dyes in wastewater has been demonstrated in recent studies. For example, Lei et al. [148], examined the degradation of methyl orange and rhodamine B dyes using an S-scheme heterostructured composite of BiOI and Bi_2WO_6 [148]. The composite photocatalyst was prepared through an in-situ hydrothermal process involving the use of an ionic liquid. The synergetic effects between the Bi_2WO_6 and BiOI resulted in an improved light absorbance and efficient photogenerated electron-hole pair separation. A red shift was observed in the UV/Vis spectrum of the composite when compared with the pristine photocatalysts. This was corroborated by a higher transient photocurrent response achieved with the heterostructured photocatalyst. The enhanced photocatalytic efficiency was ascribed to the S-scheme heterojunction formation between BiOI and Bi_2WO_6. Importantly, in the photocatalytic degradation studies, the percentage removal of methyl orange and rhodamine B were 72.1% and 90.1%, respectively. These values exceeded those obtained using either pristine BiOI or pristine Bi_2WO_6, and this further affirmed that the S-scheme heterojunction formation was favorable for the degradation of the organic dyes. These results were in conjunction with that of Xu et al., [149] for degrading rhodamine B using BiOI-based S-scheme heterostructured photocatalyst where 96% removal was achieved in 20 min.

Likewise, in the study conducted by Bavani et al. [150], BiOI/WS_2 S-scheme was constructed using a one-step solvothermal technique (Fig. 14a) and adopted for the photocatalytic removal of 99.5 % of rhodamine B from aqueous media after 60 min with a rate constant of 0.0940 min^{-1} and the recycling performance was retained after 3 consecutive runs (Fig. 14a). The enhanced performance was due to the efficient charge separation through the S-scheme mechanism, as shown in Fig. 14c. These findings clearly showed that the formation of S-scheme heterojunction is an ideal way of improving the performance of BiOI photocatalysts towards the degradation of organics in wastewater.

Apart from combined BiOI with other semiconductor photocatalysts of different chemical composition to facilitate charge separation through heterojunction with S-scheme mechanism, BiOI can also be coupled with non-stoichiometric BiOI series ($Bi_xO_yI_z$). For example, Lai et al. [151], reported the synthesis of BiOI/Bi_4/O_5I_2 as an S-scheme heterojunction. The photocatalyst was constructed through an in-situ hydrothermal technique using coconut shell as a template. The composite photocatalyst showed the highest photoelectron response, which was about 7 times more than pristine BiOI, and also the highest photocurrent response. This was due to efficiently suppressing the recombination rate resulting from the formation of S-scheme heterojunction. The composite photocatalyst was employed for the degradation of rhodamine B dye and tetracycline in the presence of visible light. The percentage removal of rhodamine B was 82% within 2 h, and this was approximately 6 times greater than the result of using native BiOI. Likewise, the removal of tetracycline using the BiOI/Bi_4/O_5I_2 heterostructured photocatalyst was approximately 5 times that of native BiOI. This trend was similar to the one observed in the degradation of bisphenol A using BiOI/Bi_4/O_5I_2 [152]. These improved performances confirmed the enhanced photocatalytic efficiency of the composite through the S-scheme heterojunction. Additionally, non-stoichiometric Bi_5O_7I has been combined with BiOI, forming an S-scheme heterojunction and applied for the removal of organic pollutants [153,154].

5. Photocatalytic removal of heavy metals using BiOX S−scheme heterojunction

Among the pollutants, heavy metals are known to negatively affect the well-being and welfare of various individuals and animals. There are

Table 1
BiOX-based S-scheme heterostructured photocatalyst materials for removal of organic pollutants.

Photocatalyst	Photocatalysis condition	Pollutant	% Removal	Rate constant (min^{-1})	Ref
BiOBr/Ag_3PO_4	C = 10 mg/L; V = 100 mL; T = 180 min; L = 1000 W Xe Lamp; D = 25 mg	Methyl Orange	99.8	0.0151	[132]
BiOBr/$AgBiO_3$	C = 20 mg/L; V = 40 mL; T = 120 min; L = 350 W Xe lamp; D = 40 mg	Ciprofloxacin	83.0	0.0149	[155]
BiOBr/AgBr	C = 10 mg/L; V = 50 mL; T = 15 min; L = 350 W Xe lamp; D = 20 mg	Sulfisoxazole	99.0	0.3199	[126]
BiOBr/AgBr	C = 10 mg/L V = 100 mL; T = 120 min; L = 500 W Xe lamp; D = 50 mg	Carbamazepine	99.64	0.0426	[125]
BiOBr/$BaFe_{12}O_{19}$	C = 10 mg/L; V = 80 mL; T = 15 min; L = 250 W Xe lamp; D = 40 mg	2-mercaptobenzothiazole	95.0	0.5529	[156]
BiOBr/$Bi_2Fe_4O_9$	C = 10 mg/L; V = 50 mL; T = 30 min; L = 300 W Xe lamp; D = 20 mg	Thiabendazole	91.2	0.0648	[157]
BiOBr/Bi_2MoO_6	C = 10 mg/L; V = 50 mL; T = 120 min; L = 500 W Xe lamp; D = 20 mg	Levofloxacin	99.0	0.0120	[158]
BiOBr/Bi_2MoO_6	C = 10 mgL-1; V = 50 mL; T = 120 min; L = 500 W Xe lamp; D = 25 mg	Ciprofloxacin	94.0	0.0169	[159]
BiOBr/BiOCl/AgBr	C = 20 mg/L; V = 50 mL; T = 90 min; L = 210 W Xe lamp; D = 10 mg	Rhodamine B	91.8	0.1180	[160]
BiOBr/BiOI	C = 10 mg/L; V = 50 mL; T = 80 min; L = 500 W Xe lamp; D = 50 mg	Tetracycline	90.0	0.021	[161]
BiOBr/BP	C = 50 mg/L; V = 100 mL; T = 90 min; L = 300 W Xe lamp; D = 100 mg	Tetracycline	85.0	0.0210	[130]
BiOBr/CNQDs	C = 50 mg/L; V = 50 mL; T = 90 min; L = 300 W Xe lamp; D = 20 mg	Tetracycline	80.0	0.0129	[162]
BiOBr/Cu_2O	C = 10 mg/L; V = 100 mL; T = 100 min; L = 300 W Xe lamp D = 20 mg	Tetracycline	78.27	0.0173	[74]
BiOBr/Cu_2O	C = 100 mg/L; V = 100 mL; T = 50 min; L = 300 W Xe lamp; D = 50 mg	Methylene blue	98.30	0.0787	[163]
BiOBr/$CuBi_2O_4$	C = 10 mg/L; V = 100 mL; T = 35 min; L = 300 W Xe lamp; D = 20 mg	Tetracycline	90.3	0.0961	[131]
BiOBr/CuO/$ZnFe_2O_4$	C = 25 mg/L; V = 150 mL; T = 90 min; L = 150 W LED lamp; D = 150 mg	Levofloxacin	91.0	–	[164]
BiOBr/$FeIn_2S_4$	C = 15 mg/L; V = 100 mL; T = 120 min; L = 500 W Xe lamp; D = 30 mg	Tetracycline	89.2	0.0249	[165]
BiOBr/g-C_3N_4	C = 50 mg/L; V = 50 mL; T = 120 min; L = 500 W Xe lamp; D = 30 mg	Ethyl xanthate	96.1	0.0282	[75]
BiOBr/g-C_3N_4	C = 10 mg/L; V = 50 mL; T = 30 min; L = 500 W Xe lamp; D = 20 mg	Rhodamine B	75.0	0.0450	[133]
BiOBr/g-C_3N_4	C = 20 mg/L; V = 100 mL; T = 180 min; L = 300 W Xe lamp; D = 20 mg	Ammonium dinitramide	95.0	0.0158	[166]
BiOBr/g-C_3N_4	C = 10 mg/L; V = 50 mL; T = 60 min; L = 350 W Xe lamp; D = 25 mg	Tetracycline	94.5	0.0434	[167]
BiOBr/In_2O_3	C = 10 mg/L; V = 200 mL; T = 30 min; L = 300 W Xe lamp; D = 100 mg	Rhodamine B	56.3	0.1180	[134]
BiOBr/MIL-101(Fe)	C = 10 mg/L; V = 100 mL; T = 40 min; L = 300 W Xe lamp; D = 25 mg	Enrofloxacin	84.4	–	[168]
BiOBr/Ni–SnS_2	C = 15 mg/L; V = 100 mL; T = 70 min; L = 500 W Xe lamp; D = 30 mg	Tetracycline	99.75	0.0488	[169]
BiOBr/PANI	C = 3 mg/L V = 40 mL; T = 40 min; L = 300 W Xe lamp; D = 20 mg	17β-estradiol	100	0.3956	[170]
BiOBr/p-C_3N_4	C = 10 mg/L; V = 100 mL; T = 30 min; L = 1000 W Xe lamp; D = 20 mg	Rhodamine B	95.23	–	[76]
BiOBr/PDI-Urea	C = 10 mg/L; V = 50 mL; T = 150 min; L = 300 W Xe lamp; D = 50 mg	Ofloxacin	93.0	0.0170	[171]
BiOBr/P-g-C_3N_4	C = 1 mg/L; V = 50 mL; T = L = 300 W Xe lamp; D = 10 mg	Phenanthrene	99.2	0.0405	[172]
BiOBr/S-g-C_3N_4	C = 5 mg/L; V = 100 mL; T = 30 min; L = 300 W Xe lamp; D = 25 mg	Rhodamine B	93.0	0.0879	[173]
BiOBr/TaON	C = 30 mg/L; V = 100 mL; T = 70 min; L = 150 W LED lamp; D = 40 mg	Tetracycline	93.0	0.0321	[174]
BiOBr/WO_3	C = 20 mg/L V = 50 mL; T = 60 min; L = 300 W Xe lamp; D = 50 mg	Tetracycline	98.0	–	[128]
BiOBr/WO_3	C = 40 mg/L; V = 40 mL; T = 50 min; L = 300 W Xe lamp; D = 20 mg	Tetracycline	100	0.0701	[127]
BiOBr/$Zn_2In_2S_5$	C = 40 mg/L; V = 50 mL; T = 40 min; L = 5 W LED; D = 50 mg	Tetracycline	97.52	–	[129]
BiOBr/$ZnFe_2O_4$/CuO	C = 25 mg/L; V = 250 mL; T = 90; L = 150 W LED lamp; D = 50 mg	Malachite Green	98.0	0.0348	[175]
BiOBr/$ZnIn_2S_4$	C = 50 mg/L; V = 50 mL; T = 30 min; L = 300 W Xe lamp; D = 20 mg	Rhodamine B	92.36	0.1372	[176]
BiOBr/β-SiC	C = 15 mg/L; V = 100 mL; T = 90 min; L = 350 W Xe lamp; D = 100 mg	Bisphenol A	68.0	–	[177]
BiOCl/Bi_2WO_6	C = 5 mg/L; V = 50 mL; T = 40 min; L = 500 W Xe lamp; D = 20 mg	Rhodamine B	98.6	–	[178]
BiOCl/$Bi2WO_6$	C = 10 mg/L; V = 50 mL; T = 90 min; L = 35 W Xe lamp; D = 20 mg	Ciprofloxacin	94.4	0.0303	[179]
BiOCl/$BiVO_4$	C = 10 mg/L; V = 50 mL; T = 120 min; L = 300 W Xe lamp; D = 20 mg	Methylene blue	97.9	0.0278	[180]
BiOCl/BP	C = 20 mg/L; V = 50 mL; T = 60 min; L = 300 W Xe lamp; D = 50 mg	Rhodamine B	98.0	–	[181]
BiOCl/$Cd_{0.5}Zn_{0.5}S$	C = 10 mg/L; V = 50 mL; T = 20 min; L = 300 W Xe lamp; D = 10 mg	Norfloxacin	77.47	–	[182]
BiOCl/Cu_2O	C = 20 mg/L; V = 50 mL; T = 80 min; L = 300 W Xe lamp; D = 20 mg	Tetracycline	90.3	–	[140]
BIOCl/Cu_3P	C = 10 mg/L; V = 50 mL; T = 60 min; L = 300 W Xe lamp; D = 50 mg	Tetracycline	86.0	0.216	[183]
BiOCl/$CuBi_2O_4$	C = 50 mg/L; V = 40 mL; T = 60 min; L = 300 Xe lamp; D = 20 mg	Diclofenac	90.0	0.0354	[142]
BiOCl/FeOCl	C = 15 mg/L; V = 50 mL; T = 60 min; L = 300 W Xe lamp; D = 50 mg	Rhodamine B	96.2	–	[144]
BiOCl/g-C_3N_4	C = 50 mg/L; V = 50 mL; T = 180 min; L = 500 W Xe lamp; D = 40 mg	Xanthate	91.2	0.0132	[77]
BiOCl/ln_2O_3	C = 20 mg/L; V = 50 mL; T = 35 min; L = 300 W Xe lamp; D = 50 mg	Ciprofloxacin	91.0	0.0713	[141]
BiOCl/MoS_2/Bi—CAU-17	C = 10 mg/L; V = 50 mL; T = 20 min; L = 300 W Xe lamp; D = 10 mg	Tetracycline	90.0	–	[184]
BiOCl/$MoSe_2$	C = 20 mg/L; V = 50 mL; T = 30 min; L = 300 W Xe lamp; D = 50 mg	Methyl orange	100	0.0063	[185]
BiOCl/SdS	C = 10 mg/L; V = 15 mL; T = 100 min; L = 300 W Xe lamp; D = 10 mg	Tetracycline	70.0	–	[139]
BiOCl/Ta_3N_5	C = 20 mg/L; V = 100 mL; T = 60 min; L = 300 W Xe lamp; D = 30 mg	Tetracycline	89.6	0.0367	[186]
BiOCl/TiO_2	C = 10 mg/L; V = 200 mL; T = 60 min; L = 300 W Xe lamp; D = 100 mg	Norfloxacin	76.0	–	[187]
BiOCl/$ZnIn_2S_4$/$FeVO_4$	C = 10^{-5} M; V = 100 mL; T = 60 min; L = 300 Xe lamp; D = 60 mg	Rhodamine B	71.2	0.1242	[188]
BiOCl–LaOCl	C = 10 mg/L; V = 50 mL; T = 30 min; L = 300 W Xe lamp; D = 50 mg	Rhodamine B	98.78	0.1209	[143]
BiOI/AgI/Bi_2WO_6	C = 20 mg/L; V = 100 mL; T = 30 min; L = 300 Xe lamp; D = 30 mg	2, 4-dinitrophenyl hydrazine	93.6	0.1200	[189]
BiOI/$Bi_2O_2(OH)(NO_3)$	C = 10 mg/L; V = 50 mL; T = 100 min; L = 300 W Xe lamp; D = 10 mg	Methylene blue	98.6	0.0459	[190]
BiOI/Bi_2O_3	C = 10 mg/L; V = 100 mL; T = 150 min; L = 300 W Xe lamp; D = 50 mg	Methylene blue	97.8	0.0218	[191]
BiOI/Bi_2WO_6	C = 10 mg/L; V = 50 mL; T = 120 min; L = 500 W Xe lamp; D = 50 mg	Rhodamine B	90.1	0.0296	[148]
BiOI/$Bi_4O_5I_2$	C = 30 mg/L; V = 50 mL; T = 120 min; L = 500 W Xe lamp; D = 20 mg	Bisphenol A	95.0	–	[152]
BiOI/$Bi_4O_5I_2$	C = 10 mg/L; V = 50 mL; T = 120 min; L = 500 W Xe lamp; D = 50 mg	Rhodamine B	82.0	0.0123	[151]

(*continued on next page*)

Table 1 (*continued*)

Photocatalyst	Photocatalysis condition	Pollutant	% Removal	Rate constant (min^{-1})	Ref
$BiOI/Bi_5O_7I$	C = 10 mg/L; V = 50 mL; T = 60 min; L = 300 W Xe lamp; D = 25 mg	Tetracycline	80.0	0.1664	[153]
$BiOI/Bi_5O_7I$	C = 20 mg/L; V = 100 mL; T = 100 min; L = 300 W Xe lamp; D = 200 mg	Tetracycline	83.0	–	[154]
$BiOI/BiVO_4$	C = 10 mg/L; V = 50 mL; T = 90 min; L = 500 W Xe lamp; D = 50 mg	Rhodamine B	90.0	–	[149]
$BiOI/g\text{-}C_3N_4$	C = 20 mg/L; V = 50 mL; T = 240 min; L = 250 W Xe lamp; D = 10 mg	Tetracycline	100	0.0095	[145]
$BiOI/g\text{-}C_3N_4$	C = 10 mg/L; V = 100 mL; T = 150 min; L = 500 W Xe lamp; D = 50 mg	Bisphenol A	83.9	0.0116	[147]
$BiOI/g\text{-}C_3N_4$	C = 30 mg/L; V = 100 mL; T = 40 min; L = 300 W Xe lamp; D = 30 mg	Tetracycline	90.1	0.1687	[146]
$BiOI/g\text{-}C_3N_4$	C = 10^{-5} M; V = 50 mL; T = 60 min; L = 250 W Xe lamp; D = 100 mg	Rhodamine B	98.9	0.0940	[150]
$BiOI/g\text{-}C_3N_4/Au$	C = 10 mg/L; V = 50 mL; T = 150 min; L = 300 W Xe lamp, D = 10 mg	Bisphenol AF	91.8	0.0174	[192]
$BiOI/TiO_2$	C = 20 mg/L; V = 50 mL; T = 180 min; L = 350 W Xe lamp; D = 50 mg	Tetracycline	98.7	0.0200	[193]
$I\text{–}BiOBr/g\text{-}C_3N_4$	C = 20 mg/L; V = 50 mL; T = 5 h; L = 300 W Xe lamp; D = 50 mg	Tetracycline	90.3	–	[194]
$L\text{-}BiOBr/Cu_3SnS_4$	C = 10 mg/L V = 100 mL; T = 10 min; L = 300 W Xe lamp; D = 50 mg	Ciprofloxacin	93.0	–	[195]

*C = initial concentration of analyte; V = volume of analyte; T = Time of photocatalyt; L = Light source; D = Photocatalyst dose.

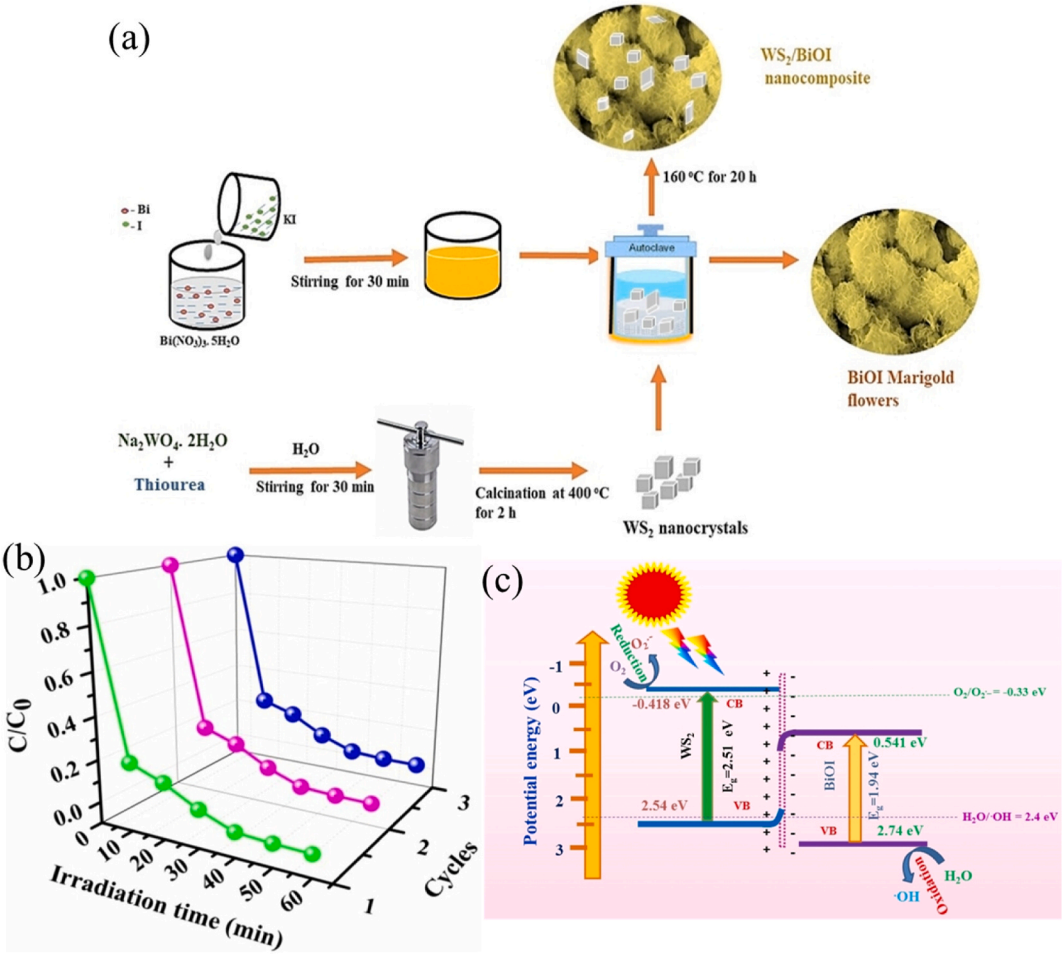


Fig. 14. (a) Schematic representation of the one-step solvothermal synthesis of the WS2/BiOI composite. (b) Photocatalytic recycling test for the optimized BW-2 composite photocatalyst for the degradation of rhodamine B (1×10^{-5} M) under 60 min of VLI. (c) Schematic diagram for the degradation of rhodamine B using $BiOI/WS_2$ S-scheme heterojunction (Reproduced with permission from Ref. [150]).

two potential solutions to these issues: deployment porous material(s) for removal and the chemical transformation of heavy metals into less harmful components via different processes such as photocatalytic, electrochemical, and catalytic. The presence of hexavalent chromium ions in water and waste water is considered to be one of the most common toxic substances in the environment [196]. They are usually released through various industrial processes, such as wood preservation, metal polishing, and leather tanning. Highly toxic Cr(VI) is known to cause various health conditions, such as kidney failure, cancer, and diarrhea. Urgent action is needed to reduce its toxicity by removing it from the environment. This process can be carried out through Cr(VI) reduction to Cr(III), which exhibits lower solubility in water [197]. Photocatalytic reduction, a chemical process gaining significant attention, utilizes sunlight to convert toxic inorganic substances to a minimally hazardous form and generates highly reactive species for organic pollutants degradation. Photocatalysts based on the S-scheme have attracted interest due to the effective electrons in the reduction process. Scavenger studies indicate that photogenerated electrons from the CB of

the reduction photocatalyst are crucial in Cr(VI) degradation, with silver nitrate being among the scavengers used.

Notably, BiOX has been a catalyst utilized in S−scheme systems for Cr(VI) reduction. Nevertheless, these BiOX S−scheme-based photocatalysts have consistently demonstrated excellent results in a short timeframe. For instance, Lu et al., [198]. introduced a novel S−scheme BiOCl(110)/TiO_2(001) for reducing Cr(VI), the heterojunction achieved 99.9% reduction in 90 min with a rate constant of 0.1367 min^{-1}. Similarly, Li et al., [186] reported an S-scheme Ta_3N_5/BiOCl system with 91.5% degradation and a rate constant of 0.001 min^{-1} [186]. It is noteworthy that various parameters influence Cr(VI) reduction, with pH being particularly significant. Optimal results are usually obtained under acidic conditions.

The synthesis of Cu_2O/BiOBr composite with a 15 wt% Cu_2O denoted as CB-15, has been reported to exhibit remarkable photocatalytic activity. CB-15 had a Cr(VI) reduction efficiency that was 21.75 times greater than that of BiOBr. The degrading efficiency of TC by CB-15 was 1.21 times greater than that of Cu_2O. An enhanced synergistic activity of CB-15 in a mixed condition was obtained. The reduction capacity of Cr (VI) and the degradation capacity of tetracycline were enhanced 1.67-fold and 1.18-fold, respectively. The increased activity of CB-15 was attributed to the S-scheme heterojunction and 3D/2D structure. Hence, the S-scheme mechanism may be more suited for the transfer of carriers in CB-X. Fig. 15a-c shows that Cu_2O exhibited characteristics of a photocatalyst with a relatively low work function of 4.84 eV, but BiOBr had a much higher work function of 6.95 eV. The S-scheme transfer mechanism in CB-15 can inhibit the recombination of photogenerated carriers (Fig. 15d), resulting in an extended fluorescence lifespan of carriers. The presence of several contact (Fig. 15a–c) regions and active sites in the 3D/2D heterostructure can significantly enhance the effectiveness of the photocatalytic process. Significantly, the photocatalyst retained its exceptional degrading capability even after undergoing four cycles of use.

Wang et al. [199], prepared Ni (II) doped $Zn_3In_2S_6$/BiOBr-OVs S−scheme for Cr(VI) reduction, noting varying rate of degradation at different pH levels (see Table 2). The degradation efficiency decreased with increasing pH. Mechanistic studies revealed that upon the formation of the heterojunction semiconductors possessing different E_{Fermi} values would undergo a spontaneous combination, resulting in the formation of a single E_{Fermi} level. This process involves the transfer of electrons and leads to the bending of the energy band. Similarly, the work by Li et al. [168], on the MIL-101(Fe)//BiOBr S-scheme strongly

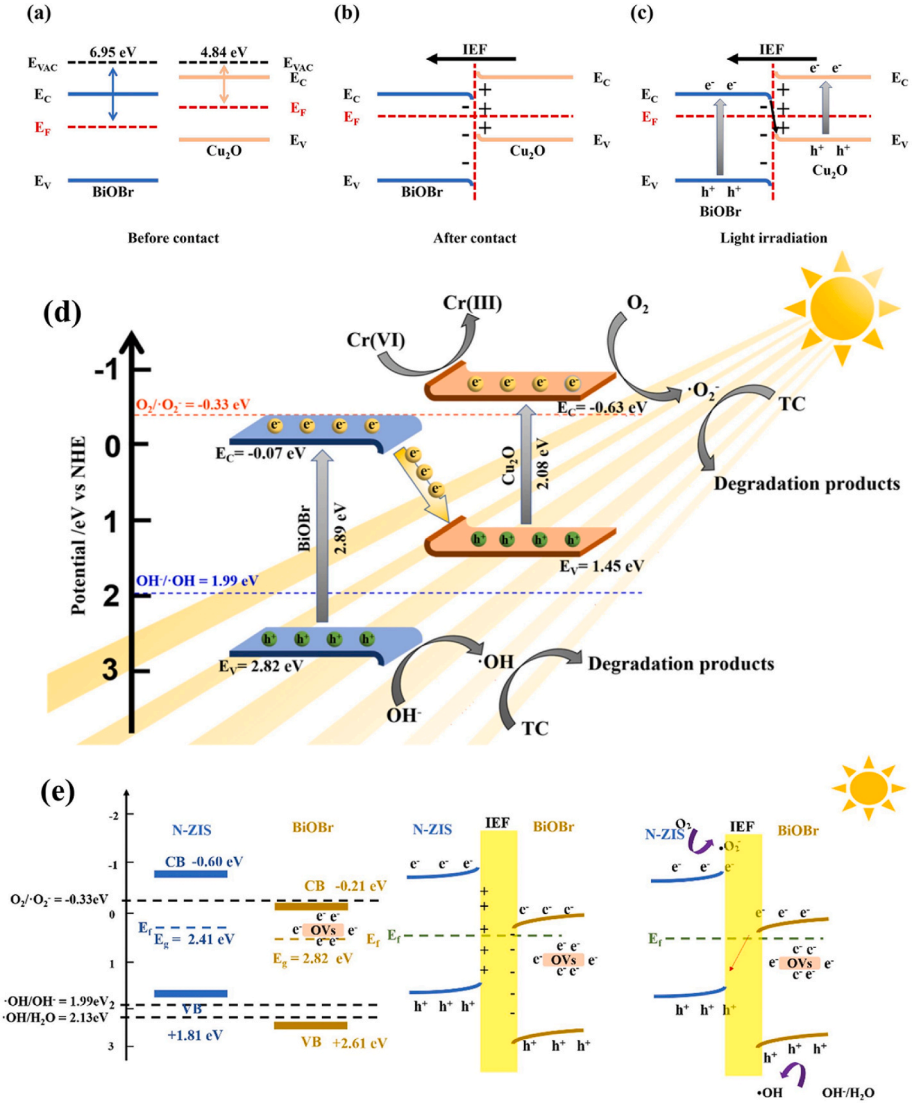


Fig. 15. Band structure of BiOBr and Cu_2O (a) before contact and (b) after contact and the carriers transfer mechanism (c) under light irradiation. (d) Schematic diagram for the reduction of Cr(VI) to Cr(III) using BiOBr/Cu_2O S-scheme heterojunction. (Reproduced with permission from Ref. [74] Copyright Elsevier 2022). (e) Mechanism diagram of N-ZISB-2 [199].

Table 2
BiOX-based S-scheme heterostructured photocatalysts for the removal of heavy metals.

Photocatalyst	Photocatalysis condition	Heavy Metal	% Removal	Rate constant (min^{-1})	Ref
Bi@BiOBr-OV/$MoSe_2$	C = 10 mg/L; V = 100 mL; T = 120 min; L = 300 W Xe lamp; D = 60 mg	Cr(VI)	99.0	–	[200]
$BiO_{1.2}I_{0.6}$/Au/g-C_3N_4	C = 10 mg/L; V = 50 mL; T = 100 min; L = 300 W Xe lamp, D = 10 mg	Cr(VI)	87.3	0.0204	[192]
BiOBr/Bi_2S_3	C = 10 mg/L; V = 100 mL; T = 120 min; L = 300 W Xe lamp; D = 100 mg	Cr(VI)	97.0	–	[201]
BiOBr/Cu_2O	C = 15 mg/L; V = 100 mL; T = 100 min; L = 300 W Xe Lamp; D = 40 mg	Cr(VI)	65.46	0.01196	[74]
BiOBr/In_2O_3	C = 10 mg/L; V = 200 mL; T = 30 min; L = 300 W Xe lamp; D = 100 mg	Cr(VI)	55.6	0.1180	[134]
BiOBr/MIL-101(Fe)	C = 20 mg/L; V = 100 mL; T = 25 min; L = 300 W Xe lamp; D = 25 mg	Cr(VI)	99.64	0.1145	[168]
BiOBr-OV/$Zn_3In_2S_6$	C = 15 mg/L; V = 100 mL; T = 100 min; L = 300 W Xe Lamp; D = 0.5 g L^{-1}	Cr(VI)	99.83	0.0541	[199]
BiOCl/BP	C = 20 mg/L; V = 50 mL; T = 60 min; L = 300 W Xe lamp; D = 50 mg	Cr(VI)	90.0	0.0373	[181]
BiOCl/MIL-101(Fe)	C = 10 mg/L; V = 100 mL; T = 60 min; L = 300 W Xe lamp; D = 30 mg	Cr(VI)	88.9	0.0288	[202]
BiOCl/Ta_3N_5	C = 20 mg/L; V = 100 mL; T = 80 min; L = 300 W Xe lamp; D = 30 mg	Cr(VI)	89.6	0.0289	[186]
BiOCl/TiO_2	C = 10 mg/L; V = 100 mL; T = 90 min; L = 300 W Xe lamp; D = 100 mg	Cr(VI)	99.0	0.0901	[198]
BiOI/Bi_5O_7I	C = 10 mg/L; V = 50 mL; T = 60 min; L = 300 W Xe lamp; D = 25 mg	Cr(VI)	100	0.0548	[153]
BiOI/g-C_3N_4	C = 10 mg/L; V = 100 mL; T = 40 min; L = 300 W Xe lamp; D = 30 mg	Cr(VI)	96.8	0.0718	[146]

supports this, reporting 99.4% degradation of Cr(VI) in 25 min under acidic conditions, while at basic conditions, the catalyst achieved only 23 % degradation within the same timeframe. Table 2 presents recent studies on the catalytic removal of Cr(VI) by BiOX-based S-scheme heterostructures.

6. Photocatalytic CO_2 reduction using BiOX S-scheme heterojunction

Global climate change and critical issues arising from fossil fuel depletion are important problems facing mankind. Increasing levels of CO_2 and other greenhouse gases are considered to be one of the main reasons for global warming [203]. To mitigate climate change and other ecological challenges, a substantial reduction in CO_2 emissions is crucial. Achieving this requires a major shift from fossil fuels, which currently account for over 80% of global energy production, to renewable energy sources. Alternatives like wind, nuclear, and solar energy produce minimal or no direct CO_2 emissions, yet they remain limited in scalability. As fossil fuel reserves are projected to deplete within the next century, significant reductions in CO_2 levels are likely only after that point. Therefore, developing methods to utilize CO_2 emissions generated in the interim as a resource is essential to minimize atmospheric release. One promising approach is the photocatalytic conversion of CO_2, which offers a pathway to repurpose CO_2 as a valuable carbon resource while reducing its environmental impact. Photoreduction of CO_2 seeks to use the energy of light to convert CO_2 to carbon resources, just as green plants do in natural photosynthesis [204].

In the photocatalytic approach for CO_2 conversion, it is crucial for a photocatalyst to meet specific requirements for successful performance. The catalyst should be able to utilize solar energy to produce electron-hole pairs. These pairs should have reducing strengths sufficient to perform the multi-electron CO_2 reduction to hydrocarbons. Photocatalyst selectivity is also crucial as it determines the type of hydrocarbons produced and the potential formation of O_2 as a by-product. BiOX has emerged as a promising candidate due to its unique properties, especially when configured into S-scheme heterojunctions.

It has been reported that BiOX with S-scheme heterojunctions performed better than pristine BiOX for the photoreduction of CO_2 to either CO or methane. For example, in a study conducted by Miao et al., an S-scheme BiOBr/Bi_2S_3 heterojunction with surface oxygen vacancies (OVs) was synthesized (Fig. 16a–h) using a simple hydrothermal technique. It was observed that the conversion rate of CO_2 to CO using BiOBr/Bi_2S_3 S-scheme photocatalyst was 2.7 times higher than using pristine BiOBr [205]. This was attributed to the formation of the s-scheme heterojunction, which improved the photocatalytic efficiency of the composite photocatalyst. The experiment and DFT calculation suggest a possible mechanism for the improved performance of BiOBr/Bi_2S_3 photocatalytic CO_2 reduction. Before coming into contact, pristine Bi_2S_3 has a lower work function (Φ) and a high E_F compared to pristine BiOBr (Fig. 16i). BiOBr has an impurity level caused by the presence of OVs. When BiOBr and Bi_2S_3 come into intimate contact, the electrons from Bi_2S_3 transfer to BiOBr until their E_F positions align. This results in a positively charged interface area on the Bi_2S_3 side, creating an electron depletion region and causing the upward bend in Bi_2S_3 energy band. However, the interface area close to BiOBr exhibits a negative charge, leading to the creation of accumulation of electron layer and a downward energy band bend for BiOBr (Fig. 16j). The CB electron of BiOBr tends to join with the VB hole of Bi_2S_3, prompted by the Coulomb interactions and internal electric field (Fig. 16k).

A similar trend was also reported with the use of BiOBr/Cu_2O S-scheme photocatalyst [206]. The photocatalyst was prepared through the hydrothermal synthesis route, and the microscopic image revealed the cubic structures of Cu_2O uniformly dispersed on the BiOBr layer. The heterostructured photocatalysts achieved a remarkable conversion rate of 22.78 μmol g^{-1} h^{-1} for CO_2 to methane. However, no yield for methane was recorded when pristine BiOBr or Cu2O photocatalyst was used. These results revealed the superiority of the composite photocatalyst due to enhanced photocatalytic efficiency resulting from the s-scheme heterojunction.

Apart from BiOBr-based S-scheme photocatalysts, both BiOCl and BiOI, consisting of S-scheme photocatalysts, have been successfully employed for the photocatalytic conversion of CO_2. For example, Ma et al. [207], prepared an S-scheme photocatalyst consisting of black phosphorous (BP) and BiOCl, which was adopted for the conversion of CO_2. The composite photocatalyst achieved a conversion rate of 260 μmol g^{-1} h^{-1} for CO_2 to CO, which was 13 times more than pure BiOCl. It was noted that the s-scheme contributed directly to the chemical activation of inert CO_2 molecules, which consequently improved the conversion rate. In another report by Li et al., the S-scheme

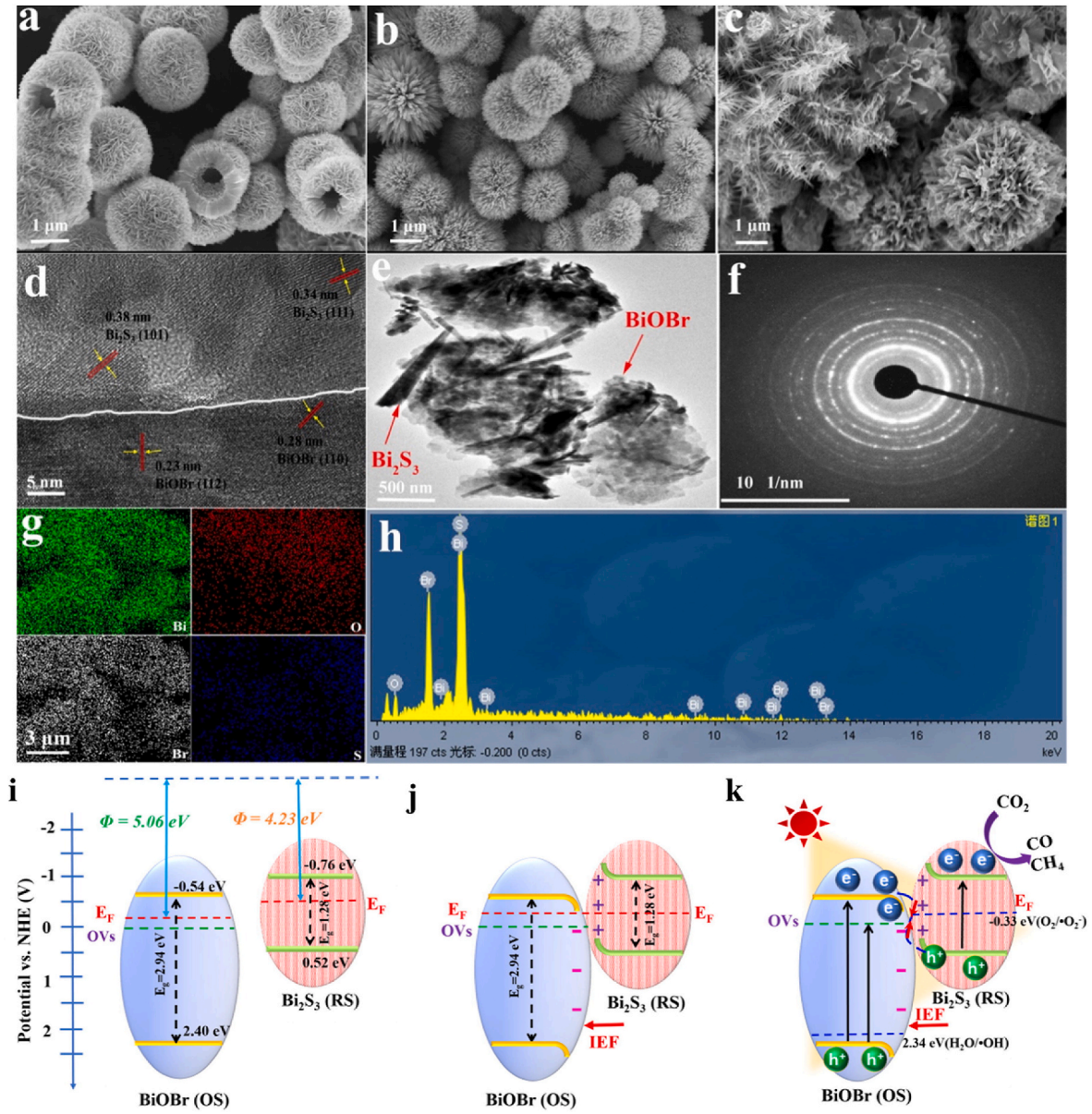


Fig. 16. SEM images of (a–c) pristine BiOBr, pristine Bi_2S_3 and BiOBr/Bi_2S_3 heterostructure. (d) HRTEM, (e) TEM,(f) SAED images, (g) elemental mapping images, and (h) EDX spectrum of BS-3. (i–k) Schematic diagram of light-induced carrier transfer of BiOBr and Bi_2S_3[205].

heterojunction of BiOI/g-C_3N_4 was applied for the photocatalytic CO_2 reduction in the presence of visible light irradiation [126]. The composite photocatalysts attained a CO production rate of 12.45 μmol g^{-1} h^{-1}. Whereas, the value reported using pure BiOI was more than four times lower, suggesting that the S-scheme composite is a better photocatalyst due to improved charge transfer efficiency. Furthermore, Table 3 presents the studies on the application of BiOX-based S-scheme heterojunction for photocatalytic CO_2 reduction. Without a doubt, these BiOX-based photocatalysts are excellent candidates for CO_2 conversion, and this is crucial for growing pollution control.

7. Photocatalytic H_2 production using BiOX S–scheme heterojunction photocatalytic

The quest for sustainable and renewable energy sources has led to significant advancements in photocatalytic hydrogen production, with semiconductor-based materials playing a crucial role in this domain. BiOX has emerged as a promising candidate among these materials due to its unique properties, especially when configured into S-scheme heterojunctions. BiOX, a layered semiconductor compound, possesses a suitable band gap for visible light absorption, making it an efficient photocatalyst. When combined with other semiconductors to form S-Scheme heterojunctions, such as BiOBr/Bi_2WO_6, BiOBr/$BiVO_4$, or BiOBr/$Bi_2O_2CO_3$, the resulting synergistic effects enhance the charge separation and migration, thereby improving the photocatalytic hydrogen evolution. The photocatalytic hydrogen production mechanism on BiOBr S-Scheme heterojunctions involves multiple steps, including light absorption, charge generation, charge separation, surface reactions, and hydrogen evolution (HER) and oxygen evolution (OER). The heterojunction structure facilitates the transfer of photogenerated electron and hole, minimising their recombination and enhancing the overall efficiency of hydrogen generation. Several factors influence the photocatalytic activity of BiOX S-Scheme heterojunctions, such as semiconductor morphology, crystallinity, surface area, band structure, cocatalyst deposition, and reaction conditions (pH, temperature, light intensity). Optimizing these parameters is essential to achieve higher hydrogen production rates and improved stability over prolonged operation. Recent studies have demonstrated remarkable progress in

Table 3
Photocatalytic CO_2 reduction on BiOX-based S-scheme heterojunctions.

Photocatalyst	Reaction Condition	Yield of CO ($\mu mol.g^{-1}.h^{-1}$)	Yield of CH_4 ($\mu mol.g^{-1}.h^{-1}$)	Ref
BiOBr/NiO	D = 10 mg; LS = 300 Xe lamp; T = 3 h	12.8	6.6	[208]
BiOBr/Bi_2S_3	D = 10 mg; LS = 300 Xe lamp; T = 3 h	100.8	8.5	[205]
BiOBr/Cu_2O	D = 20 mg; LS = 300 Xe lamp; T = 4 h	–	22.78	[206]
BiOBr/Bi_2WO_6	D = 10 mg; LS = 300 Xe lamp; T = 4 h	55.17	–	[209]
BiOBr/Bi_2SiO_5/Bi	D = 20 mg; LS = 300 Xe lamp; T = 4 h	234.05	–	[210]
CoPc/BiOBr-NSs	D = 5 mg; LS = 300 Xe lamp; T = 4 h	59.9	–	[211]
BiOBr/$CsPbBr_3$	D = 8 mg; LS = 300 Xe lamp; T = 4 h	72.3	10.0	[212]
BiOCl/BP	D = 10 mg; LS = 300 Xe lamp; T = 5 h	260.0	–	[207]
BiOCl/WO_x	D = 30 mg; LS = 300 Xe lamp; T = 4 h	8.82	–	[213]
Bi–BiOCl/$MgIn_2S_4$	D = 10 mg; LS = 300 Xe lamp; T = 6 h	–	4.29	[214]
BiOCl/In_2O_3/Bi	D = 10 mg; LS = 300 Xe lamp; T = 4 h	34.53	–	[215]
BiOI/g-C_3N_4	D = 10 mg; LS = 300 Xe lamp; T = 4 h	12.45	–	[145]
BiOI/Bi_2MoO_6	D = 10 mg; LS = 300 Xe lamp; T = 4 h	13.5	–	[216]

enhancing the photocatalytic performance of BiOBr S-Scheme heterojunctions through strategies like doping, surface modification, cocatalyst engineering, and heterojunction design optimization. However, challenges such as low quantum efficiency, photocorrosion, and scalability issues need to be addressed for practical implementation in large-scale hydrogen production systems. Despite the challenges, the potential of BiOX S-Scheme heterojunctions in photocatalytic hydrogen production is promising. Future research directions should focus on a fundamental understanding of charge dynamics, novel material synthesis techniques, and integration with renewable energy sources for sustainable hydrogen fuel generation.

BiOX S-Scheme heterojunctions hold immense potential for efficient photocatalytic hydrogen production. Continued research efforts addressing the existing challenges and exploring innovative approaches will pave the way for practical application in renewable environmental remediation and energy conversion. The photocatalytic water splitting for hydrogen production was by Guo et al., [217] using Sn-doped ZnO/BiOCl (ZBC-S). The probability of recombination for the carriers generated by light is diminished upon the formation of a ZnO/BiOCl heterojunction. The introduction of impurity level through Sn doping results in the narrowing of the band gap widths of both ZnO and BiOCl, thereby enhancing light absorption to some extent. Among ZnO, BiOCl, and ZnO/BiOCl, the ZBC-S composites exhibit the highest photocatalytic activity. Furthermore, the introduction of Eosin Y dye as a sensitizer enhances the efficiency generation of H_2. With simulated sunlight, the H_2 rate generation peaks at 4146.77 $\mu mol\ g^{-1}\ h^{-1}$ for the ZBC-S composite, marking a 27-fold increase compared to pure ZnO [217].

Lee et al. reported the photocatalytic performance of various bismuth oxyhalide hierarchical microspheres (BiOX, where X = Br,Cl, and I) and their composites in splitting water under visible light [218]. They examined key factors such as dosage, water pH, and the type of bismuth oxyhalide for HER and OER. The efficiency of hydrogen production using BiOI photocatalyst was found to increase with pH from 3 to 7, reaching a maximum of 1316.9 $\mu mol\ h^{-1}\ g^{-1}$ at pH 7 (Fig. 17a). Compared to other bismuth oxyhalides, BiOI showed superior performance in both HER and OER, attributed to its conduction band level providing sufficient overpotential for water conversion. Additionally, BiOI exhibited higher positive surface charges at lower pH, decreasing as pH increased (pH < pHzpc). Hence, the primary reason for weak H^+ adsorption on the surface is predominantly electrostatic repulsion, leading to a decrease in the rate of hydrogen production. The impact of dosage on HER has been investigated by varying BiOI concentration from 0.10 to 0.40 g L^{-1} (Fig. 17b). Tit was observed that the photocatalytic performance improved with BiOI dosage up to 0.20 g L^{-1}, beyond which further increase led to a decline in HER rates. This trend was attributed to increased active sites initially, followed by aggregation of the photocatalyst and reduced light penetration, causing a decrease in reaction rates. Therefore, while higher BiOI amounts initially boosted hydrogen evolution, excessive dosage hindered incident light and introduced recombination centers, leading to a gradual decrease in efficiency. Comparing BiOI with composites (Fig. 17c) the composites were expected to have higher photocatalytic efficiency due to thier lower PL intensity which suggest improved charge separation. However, BiOI showed better photocatalytic HER and OER as compared to the composites. This could be due to the wide band-gap energy of 3.29 eV in $BiOCl_xBr_{1-x}$, which does not enable effective utilization of visible light, despite possessing ample over-potential in the conduction band. Conversely, although $BiOCl_xI_{1-x}$ and $BiOBr_xI_{1-x}$ have band gaps suitable for efficient visible light absorption, they lack sufficient conduction band over-potential for the conversion of H^+ to H_2 (as illustrated in Fig. 17d). Consequently, composite photocatalysts of $BiOA_xB_{1-x}$ would diminish the catalytic efficacy toward water splitting compared to BiOXs.

Zhou et al. [219], engineered a p-n heterojunction of Bi^0/p--BiOI/n-CdS for water splitting. Experimental data analysis revealed an H_2 production efficiency of 31 mmol/h. The incorporation of p-BiOI/n-CdS heterojunction along with Bi^0 served to amplify the Surface Plasmon Resonance (SPR) effect, thereby enhancing the kinetics of two-electron transfer and optical absorption. This spatial separation of the O_2 and H_2 active sites minimized electron recombination from CdS, leading to improved performance.

In another study, BiOCl was loaded with copper phthalocyanine to improve the photocatalytic H_2 production. By depositing the gold on the (001) facet and MnO_x on the (110) facet of BiOCl, the recombination of electron-hole pairs created by light was substantially reduced, leading to a significant improvement in the photocatalytic activity [220]. However, the amount of photocatalytic hydrogen produced was lower. Introducing surface oxygen vacancy onto BiOCl emerges as an efficient process of boosting the HER activity. By employing a glycerol-assisted solvothermal process [221]. The synthesis of BiOCl nanosheet containing oxygen vacancy on their surface has been reported. The as-obtained nanosheet demonstrated a higher ability toward HER when exposed to visible light compared to bulk BiOCl. This improved performance was ascribed to the nanosheet capacity to separate and utilize light energy more efficiently, owing to their broadened facet spacing and oxygen vacancy. To further improve the H_2 production, the nanosheet was doped with carbon, thereby resulting in a remarkable increase in their HER capability. This doping process involved using triethanolamine as a sacrificial electron donor and NiOx as a co-catalyst [56]. This translates to an optimal H_2 production rate of 0.42 mmol $h^{-1}\ g^{-1}$ on a carbon-doped {010}-facet BiOCl nanosheet. Additionally, beyond BiOCl, other bismuth oxyhalides such as $Bi_{12}O_{17}Cl_2$ [222] and $Bi_{24}O_{31}Br_{10}$ [223] have also shown promise for photocatalytic hydrogen evolution.

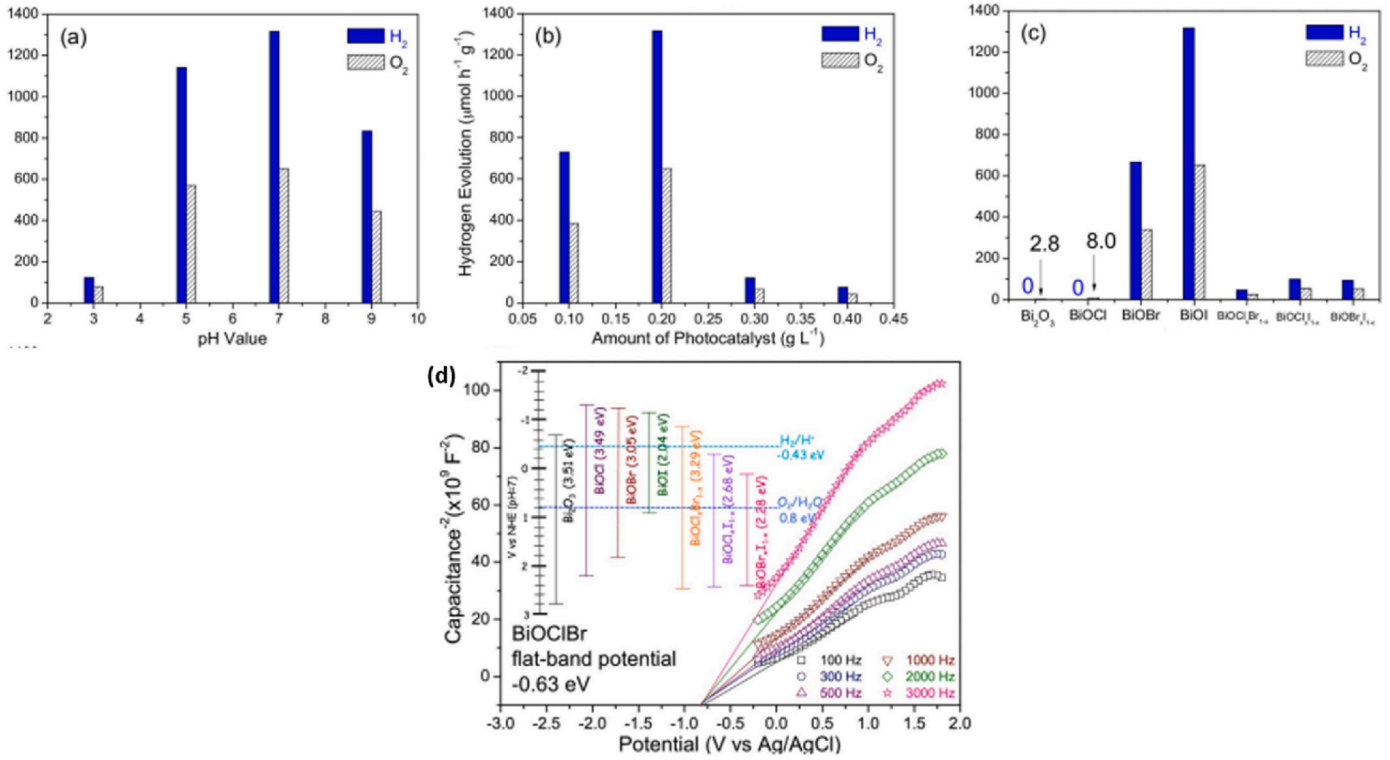


Fig. 17. Effect of (a)pH, (b) dosage and (c) different photocatalysts for hydrogen evolution and oxygen evolution, (d) Mott-Schottky plots and Energy-level diagram (CB and VB redox potentials) [218].

Chang et al. [224], fabricated a BiOBr/Bi_2S_3 heterojunction consisting of Cu complex as a cocatalyst/redox mediator. The fabricated photocatalyst composite (BiOBr/Bi_2S_3–Cu) was employed for photocatalytic hydrogen production. For the hydrogen (H_2) test, a specific quantity of a suspension of a photocatalyst composite weighing 0.05 g was prepared in a sacrificial solution consisting of 100 mL of Na_2S, NaCl, and Na_2SO_3. A magnetic stirrer was placed at the base of the reactor and maintained constant agitation during the photocatalysis reaction. The H_2 production volume was quantified at 60-min intervals using GC-TCD. The H_2 generation rate of BiOBr and the Cu macrocyclic complex were 103 and 203 μmol g^{-1} h^{-1}, respectively. Hence, it is vital to augment the functions of BiOBr and the Cu complex. The addition of Bi_2S_3 to the BiOBr resulted in the H_2 production rate of 445 μmol g^{-1} h^{-1}, which is 4.3 times that of pristine BiOBr. The enhanced photocatalytic activity could be ascribed to an improved photoexcited electron and hole transfer at the BiOBr/Bi_2S_3 interface. Moreover, the incorporation of the Cu macrocyclic complex into BiOBr also resulted in an enhancement of its activity. The composite of BiOBr and a Cu macrocyclic complex demonstrated a photoactivity of 390 μmol g^{-1} h^{-1}. The activity of the composite material consisting of BiOBr/Bi_2S_3/Cu macrocyclic complex attained 1030 μmol h^{-1} g^{-1}, which is 2.3 times higher than that of BiOBr/Bi_2S_3 and 10 times higher than that of BiOBr. The results highlight the considerable potential of the combined impact of the BiOBr/Bi_2S_3 heterojunction and the Cu macrocyclic complex in improving the photocatalytic process for H_2 production.

Lu et al. [225], constructed a BiOCl–PbS heterostructure intending to broaden the light absorption spectrum and enhance the separation of electron-hole pairs, thereby enhancing the efficiency of solar-to-chemical energy conversion [225]. The PbS nanocrystal was selectively placed onto the (001) and (110) surfaces of BiOCl nanoplate, resulting in the formation of BiOCl (01)-PbS and BiOCl (110)-PbS, respectively. The BiOCl (110)-PbS was shown to have an average H_2 generation rate that was ~3 times higher than that of BiOCl (0 0 1)-PbS when exposed to broad-spectrum irradiation. The increase in performance can be ascribed mainly to differences in the efficiency of charge transfer at the interface. The BiOCl (0 01)-PbS samples exhibit V-shaped band alignments because of the disparity in band energy between the BiOCl (0 0 1) and (1 1 0) facets. As a result, photogenerated electrons gather at the BiOCl (0 0 1)-PbS interface, impeding the ongoing transfer and separation of charges between PbS and BiOCl. In contrast, the BiOCl (1 1 0)-PbS systems exhibit ladder-shaped band alignments, which promote efficient charge transfer and separation, thereby preventing the electron buildup at the interface.

The photocatalytic activity of BiOI has been observed to be improved by forming an AgI– BiOI heterojunction and introducing graphene [226]. The improved photocatalytic hydrogen production by the composite (AgI– BiOI-graphene) was due to better charge transfer and separation. The maximum hydrogen production was estimated to be 72 μmol h^{-1} g^{-1}, 135 μmol h^{-1} g^{-1}, and 168 μmol h^{-1} g^{-1} for BiOI, BiOI-graphene, and AgI– BiOI-graphene, respectively.

Zhao et al. [227], developed a heterostructure of BiOBr@TiO_2 p–n junction for improved photocatalytic water splitting and photodegradation of rhodamine dye. Concerning H_2 production, TiO_2 nanobelts exhibit minimal H_2-production activity owing to their poor response to visible light. Similarly, pure BiOBr demonstrates slight H_2 production. However, there is a significant enhancement in H_2 evolution on BiOBr@TiO_2 heterostructure. Particularly noteworthy is the existence of an optimum ratio of BiOBr to TiO_2 for maximizing H_2 generation. BiOBr@TiO_2-1 displays the highest H_2-production activity, reaching up to 122 mol^{-1} g^{-1} h^{-1}, which is twice that of BiOBr@TiO_2-1.5 and BiOBr@TiO_2-0.5. These findings align with those observed in the photodegradation of RhB. This is attributed to the fact that an insufficient loading of BiOBr leads to inadequate absorption of visible light, whereas excessive loading of BiOBr causes fast electron and hole recombinations. Furthermore, Table 4 presents the studies on the application of BiOX-based S-scheme heterojunction for photocatalytic H_2 production.

Table 4
Photocatalytic hydrogen production using BiOX-based catalyst using a Xe lamp (300 W) as the light source.

Photocatalyst	Solution source	H_2 rate production	Ref
ZnO/BiOCl	Deionised water	313.61 mmol g^{-1} h^{-1}	[217]
$BiOBr/Bi_2S_3$	Sacrificial solution of Na_2S, NaCl, and Na_2SO_3	445 μmol g^{-1} h^{-1}	[224]
BiOCl/PbS	H_2O containing Na_2S and Na_2SO_3	0.8 μmol g^{-1} h^{-1}	[225]
AgI/BiOI	Ethylene glycol as a sacrificial agent	168 μmol $h^{-1}g^{-1}$	[226]
$BiOBr/TiO_2$	Sacrificial solution of Na_2S, NaCl, and Na_2SO_3	122 mol $^{-1}$ g^{-1} h^{-1}	[227]
BiOI/CdS	A solution containing 10 vol % lactic acid	36 μmol $h^{-1}g^{-1}$	[219]
$BiOBr/g\text{-}C_3N$	Solution containing TEOA (20 vol %)	31.66 μmol $h^{-1}g^{-1}$	[228]
$ZnIn_2S_4/BiOI$	Solution containing TEOA	206.4 μmol $h^{-1}g^{-1}$	[229]
$TiO_{2-x}/BiOI$	Solution containing 15 vol% of methanol	46.755 μmol $h^{-1}g^{-1}$	[230]

8. Conclusion and future perspective

Bismuth oxyhalides (BiOX) continue to be a pivotal group of photocatalysts in the field of photocatalysis, with significant advancements made in their development and applications. The increasing number of publications on BiOX reflects a growing interest in these materials, particularly for environmental remediation. While BiOX photocatalysts have shown promise, their core limitations include the tendency for photo-generated electron-hole pairs to recombine, limited visible light absorption, and constrained redox potential. To address these limitations, the construction of heterojunctions (particularly S-scheme BiOX heterojunctions) has emerged as an effective strategy. These heterojunctions show improved charge separation, enhanced visible light absorption, and greater photocatalytic efficiency for the degradation of various organic pollutants, including pharmaceuticals, dyes, pesticides, and phenols. Furthermore, these processes often harness visible light, making BiOX photocatalysts viable for solar-driven applications. Importantly, the preparation of these S-scheme BiOX heterojunctions remains relatively straightforward, adding to their appeal for practical use.

Despite these advances, several challenges and opportunities for improvement remain in the study and application of BiOX-based S-scheme heterostructures. First, there is a need for thorough validation of the S-scheme charge separation mechanism. In some studies, insufficient data prevents a clear distinction between the conventional Type II and S-scheme mechanisms, highlighting the need for both experimental and theoretical analyses to confirm the mechanism accurately. Additionally, although BiOX-based heterostructures are designed to operate under visible or solar light, most studies continue to use artificial light sources (such as Xenon lamps with UV cutoff) rather than direct sunlight. This approach limits the understanding of their potential for real-world, solar-driven applications. Furthermore, although BiOX photocatalysts have shown efficiency in simulated wastewater treatments, there is a notable lack of research on their performance in real wastewater effluents, which may contain complex mixtures of pollutants that differ significantly from laboratory-simulated samples.

Therefore, future research on the BiOX S-scheme heterojunctions should focus on the following areas. First, rigorous design and characterization protocols are essential to clearly understand charge separation mechanisms. Secondly, studies should prioritize the use of direct sunlight as the light source for photocatalytic applications, thus providing a more realistic assessment of these materials' suitability for solar-driven processes. Additionally, applying BiOX-based photocatalysts to real wastewater effluents will provide critical insights into their practical efficacy and environmental impact. Beyond environmental remediation, BiOX photocatalysts hold significant potential in other energy applications, including photocatalytic hydrogen production and CO_2 reduction. Coupling BiOX S-scheme heterostructures with other advanced oxidation technologies, such as Fenton or electro-Fenton processes, could further enhance the degradation rates of pollutants and expand their use in various environmental and energy applications.

Moreover, while oxygen vacancies are the most common defects in BiOX structures, introducing a wider variety of defects—such as dual vacancies, halogen vacancies, or dislocations—could be instrumental in tuning electronic properties and enhancing photocatalytic performance. These defects introduce additional electronic states and influence electron transfer dynamics, potentially leading to improved photocatalytic activity. Further research into controlled defect engineering, aimed at establishing a direct correlation between defect type, density, and photocatalytic performance, could offer transformative insights into the optimization of BiOX-based materials.

Overall, the development of BiOX-based S-scheme heterostructured photocatalysts remains an exciting area of study. By addressing the outlined challenges and broadening the scope of applications, future research could unlock the full potential of BiOX materials, paving the way for practical, large-scale applications in environmental and energy-related fields.

CRediT authorship contribution statement

Tunde L. Yusuf: Writing – review & editing, Writing – original draft, Data curation, Conceptualization. **Benjamin O. Orimolade:** Writing – review & editing, Writing – original draft. **Daniel Masekela:** Writing – review & editing. **Kayode A. Adegoke:** Writing – review & editing, Writing – original draft. **Kwena D. Modibane:** Writing – review & editing. **Seshibe S. Makgato:** Writing – review & editing, Writing – original draft.

Declaration of competing interest

The authors declare that they have no known competing financial interests or personal relationships that could have appeared to influence the work reported in this paper.

Data availability

No data was used for the research described in the article.

References

[1] S. Jargin, Overpopulation and international conflicts: an update, J. Environ. Stud. 8 (2022) 1–10, https://doi.org/10.13188/2471-4879.1000034.
[2] S. Jargin, The conflict around Ukraine: social and environmental aspects, J. Environ. Stud. 8 (2022) 5, https://doi.org/10.13188/2471-4879.1000035.
[3] J.G. Kovoor, S. Bacchi, A.K. Gupta, G.J. Maddern, COVID-19 and the Ukraine-Russia conflict: warnings from history, Br. J. Surg. 109 (2022) 777, https://doi.org/10.1093/bjs/znac133.
[4] S. Vinoth, W.-J. Ong, A. Pandikumar, Defect engineering of BiOX (X = Cl, Br, I) based photocatalysts for energy and environmental applications: current progress and future perspectives, Coord. Chem. Rev. 464 (2022) 214541, https://doi.org/10.1016/j.ccr.2022.214541.
[5] J. Zheng, Y. Lyu, B. Wu, S. Wang, Defect engineering of the protection layer for photoelectrochemical devices, EnergyChem 2 (2020) 100039, https://doi.org/10.1016/j.enchem.2020.100039.
[6] K.A. Adegoke, A.K. Oyebamiji, A.O. Adeola, A.B. Olabintan, K.O. Oyedotun, B. B. Mamba, O.S. Bello, Iron-based metal–organic frameworks and derivatives for electrochemical energy storage and conversion, Coord. Chem. Rev. 517 (2024) 215959, https://doi.org/10.1016/j.ccr.2024.215959.
[7] K.A. Adegoke, O.R. Adegoke, R.A. Adigun, N.W. Maxakato, O.S. Bello, Two-dimensional metal-organic frameworks: from synthesis to biomedical, environmental, and energy conversion applications, Coord. Chem. Rev. 473 (2022) 214817, https://doi.org/10.1016/j.ccr.2022.214817.
[8] F. Xu, K. Meng, B. Cheng, S. Wang, J. Xu, J. Yu, Unique S-scheme heterojunctions in self-assembled TiO2/CsPbBr3 hybrids for CO2 photoreduction, Nat. Commun. 11 (2020) 4613, https://doi.org/10.1038/s41467-020-18350-7.

[9] X. Lv, F.L.Y. Lam, X. Hu, A review on bismuth oxyhalide (BiOX, X=Cl, Br, I) based photocatalysts for wastewater remediation, Front. Catal. 2 (2022) 839072, https://doi.org/10.3389/fctls.2022.839072.
[10] A. Malathi, J. Madhavan, M. Ashokkumar, P. Arunachalam, A review on BiVO4photocatalyst: activity enhancement methods for solar photocatalytic applications, Appl. Catal. Gen. 555 (2018) 47–74, https://doi.org/10.1016/j.apcata.2018.02.010.
[11] M.F.R. Samsudin, S. Sufian, B.H. Hameed, Epigrammatic progress and perspective on the photocatalytic properties of BiVO4-based photocatalyst in photocatalytic water treatment technology: a review, J. Mol. Liq. 268 (2018) 438–459, https://doi.org/10.1016/j.molliq.2018.07.051.
[12] B.O. Orimolade, O.A. Arotiba, Bismuth vanadate in photoelectrocatalytic water treatment systems for the degradation of organics: a review on recent trends, J. Electroanal. Chem. 878 (2020) 114724, https://doi.org/10.1016/j.jelechem.2020.114724.
[13] S.J. Segovia-Sandoval, H.J. Ojeda-Galván, A.I. Moral-Rodríguez, J. Rodríguez-Hernández, R.D. Peralta-Rodríguez, K.J. Gómez-Villegas, N.I. Hernández-Juárez, E. Mendoza-Mendoza, A novel green synthesis of Bi2WO6-based photocatalysts for efficient pollutants degradation using low-power UV-A LEDs, J. Alloys Compd. 911 (2022) 165018, https://doi.org/10.1016/j.jallcom.2022.165018.
[14] B.O. Orimolade, A.O. Idris, U. Feleni, B. Mamba, Recent advances in degradation of pharmaceuticals using Bi 2 WO 6 mediated photocatalysis – a comprehensive review, Environ. Pollut. 289 (2021) 117891, https://doi.org/10.1016/j.envpol.2021.117891.
[15] M. Arumugam, M.Y. Choi, Recent progress on bismuth oxyiodide (BiOI) photocatalyst for environmental remediation, J. Ind. Eng. Chem. 81 (2020) 237–268, https://doi.org/10.1016/j.jiec.2019.09.013.
[16] W.-W. Liu, R.-F. Peng, Recent advances of bismuth oxychloride photocatalytic material: property, preparation and performance enhancement, J. Electron. Sci. Technol. 18 (2020) 100020, https://doi.org/10.1016/j.jnlest.2020.100020.
[17] J. Li, Y. Yu, L. Zhang, Bismuth oxyhalide nanomaterials: layered structures meet photocatalysis, Nanoscale 6 (2014) 8473–8488, https://doi.org/10.1039/C4NR02553A.
[18] Y. Mi, H. Li, Y. Zhang, W. Hou, Synthesis of belt-like bismuth-rich bismuth oxybromide hierarchical nanostructures with high photocatalytic activities, J. Colloid Interface Sci. 534 (2019) 301–311, https://doi.org/10.1016/j.jcis.2018.09.038.
[19] M. Marks, H.S. Jeppesen, N. Lock, Tuneable phase, morphology, and performance of bismuth oxyhalide photocatalysts via microwave-assisted synthesis, ACS Appl. Mater. Interfaces 14 (2022) 23496–23506, https://doi.org/10.1021/acsami.2c03837.
[20] A.K. Geim, I.V. Grigorieva, Van der Waals heterostructures, Nature 499 (2013) 419–425, https://doi.org/10.1038/nature12385.
[21] M. Chhowalla, H.S. Shin, G. Eda, L.-J. Li, K.P. Loh, H. Zhang, The chemistry of two-dimensional layered transition metal dichalcogenide nanosheets, Nat. Chem. 5 (2013) 263–275, https://doi.org/10.1038/nchem.1589.
[22] H. Chang, H. Wu, Graphene-based nanocomposites: preparation, functionalization, and energy and environmental applications, Energy Environ. Sci. 6 (2013) 3483, https://doi.org/10.1039/c3ee42518e.
[23] C.G. Silva, Y. Bouizi, V. Fornés, H. García, Layered double hydroxides as highly efficient photocatalysts for visible light oxygen generation from water, J. Am. Chem. Soc. 131 (2009) 13833–13839, https://doi.org/10.1021/ja905467v.
[24] L. Ye, Y. Su, X. Jin, H. Xie, C. Zhang, Recent advances in BiOX (X = Cl, Br and I) photocatalysts: synthesis, modification, facet effects and mechanisms, Environ. Sci. Nano 1 (2014) 90, https://doi.org/10.1039/c3en00098b.
[25] W.L. Huang, Q. Zhu, Electronic structures of relaxed BiOX (X=F, Cl, Br, I) photocatalysts, Comput. Mater. Sci. 43 (2008) 1101–1108, https://doi.org/10.1016/j.commatsci.2008.03.005.
[26] W.L. Huang, Electronic structures and optical properties of BiOX (X = F, Cl, Br, I) via DFT calculations, J. Comput. Chem. 30 (2009) 1882–1891, https://doi.org/10.1002/jcc.21191.
[27] K. Zhao, L. Zhang, J. Wang, Q. Li, W. He, J.J. Yin, Surface structure-dependent molecular oxygen activation of BiOCl single-crystalline nanosheets, J. Am. Chem. Soc. 135 (2013) 15750–15753, https://doi.org/10.1021/ja4092903.
[28] A.M. Ganose, M. Cuff, K.T. Butler, A. Walsh, D.O. Scanlon, Interplay of orbital and relativistic effects in bismuth oxyhalides: BiOF, BiOCl, BiOBr, and BiOI, Chem. Mater. 28 (2016) 1980–1984, https://doi.org/10.1021/acs.chemmater.6b00349.
[29] X. Wu, Y.H. Ng, L. Wang, Y. Du, S.X. Dou, R. Amal, J. Scott, Improving the photo-oxidative capability of BiOBr: via crystal facet engineering, J. Mater. Chem. A 5 (2017) 8117–8124, https://doi.org/10.1039/c6ta10964k.
[30] X. Wu, K. Zhang, G. Zhang, S. Yin, Facile preparation of BiOX (X = Cl, Br, I) nanoparticles and up-conversion phosphors/BiOBr composites for efficient degradation of NO gas: oxygen vacancy effect and near infrared light responsive mechanism, Chem. Eng. J. 325 (2017) 59–70, https://doi.org/10.1016/j.cej.2017.05.044.
[31] J. Xiong, P. Song, J. Di, H. Li, Z. Liu, Freestanding ultrathin bismuth-based materials for diversified photocatalytic applications, J. Mater. Chem. A 7 (2019) 25203–25226, https://doi.org/10.1039/C9TA10144F.
[32] J. Di, J. Xia, H. Li, S. Guo, S. Dai, Bismuth oxyhalide layered materials for energy and environmental applications, Nano Energy 41 (2017) 172–192, https://doi.org/10.1016/j.nanoen.2017.09.008.
[33] K. Zhang, C. Liu, F. Huang, C. Zheng, W. Wang, Study of the electronic structure and photocatalytic activity of the BiOCl photocatalyst, Appl. Catal. B Environ. 68 (2006) 125–129, https://doi.org/10.1016/j.apcatb.2006.08.002.
[34] J. Di, C. Chen, S.-Z. Yang, M. Ji, C. Yan, K. Gu, J. Xia, H. Li, S. Li, Z. Liu, Defect engineering in atomically-thin bismuth oxychloride towards photocatalytic oxygen evolution, J. Mater. Chem. A 5 (2017) 14144–14151, https://doi.org/10.1039/C7TA03624H.
[35] W. Wang, W. Yang, R. Chen, X. Duan, Y. Tian, D. Zeng, B. Shan, Investigation of band offsets of interface BiOCl:Bi2WO6: a first-principles study, Phys. Chem. Chem. Phys. 14 (2012) 2450, https://doi.org/10.1039/c2cp23186g.
[36] L. Zhao, X. Zhang, C. Fan, Z. Liang, P. Han, First-principles study on the structural, electronic and optical properties of BiOX (X=Cl, Br, I) crystals, Phys. B Condens. Matter 407 (2012) 3364–3370, https://doi.org/10.1016/j.physb.2012.04.039.
[37] L. Wang, L. Wang, Y. Du, X. Xu, S.X. Dou, Progress and perspectives of bismuth oxyhalides in catalytic applications, Mater. Today Phys. 16 (2021) 100294, https://doi.org/10.1016/j.mtphys.2020.100294.
[38] J. Di, J. Xia, M. Ji, S. Yin, H. Li, H. Xu, Q. Zhang, H. Li, Controllable synthesis of Bi 4 O 5 Br 2 ultrathin nanosheets for photocatalytic removal of ciprofloxacin and mechanism insight, J. Mater. Chem. A 3 (2015) 15108–15118, https://doi.org/10.1039/C5TA02388B.
[39] J. Wang, Y. Yu, L. Zhang, Highly efficient photocatalytic removal of sodium pentachlorophenate with Bi3O4Br under visible light, Appl. Catal. B Environ. 136–137 (2013) 112–121, https://doi.org/10.1016/j.apcatb.2013.02.009.
[40] X. Xiao, J. Jiang, L. Zhang, Selective oxidation of benzyl alcohol into benzaldehyde over semiconductors under visible light: the case of Bi12O17Cl2 nanobelts, Appl. Catal. B Environ. 142–143 (2013) 487–493, https://doi.org/10.1016/j.apcatb.2013.05.047.
[41] X. Xiao, R. Hao, X. Zuo, J. Nan, L. Li, W. Zhang, Microwave-assisted synthesis of hierarchical Bi7O9I3 microsheets for efficient photocatalytic degradation of bisphenol-A under visible light irradiation, Chem. Eng. J. 209 (2012) 293–300, https://doi.org/10.1016/j.cej.2012.07.142.
[42] X. Xiao, C. Liu, R. Hu, X. Zuo, J. Nan, L. Li, L. Wang, Oxygen-rich bismuth oxyhalides: generalized one-pot synthesis, band structures and visible-light photocatalytic properties, J. Mater. Chem. 22 (2012) 22840, https://doi.org/10.1039/c2jm33556e.
[43] D. Liu, J. Zhang, C. Li, X. Zhang, X. Chen, F. Wang, M. Shi, R. Li, C. Li, In-situ fabrication of atomic charge transferring path for constructing heterojunction photocatalysts with hierarchical structure, Appl. Catal. B Environ. 248 (2019) 459–465, https://doi.org/10.1016/j.apcatb.2019.02.050.
[44] F. Li, Q. Wang, X. Wang, B. Li, Y. Hao, R. Liu, D. Zhao, In-situ one-step synthesis of novel BiOCl/Bi24O31Cl10 heterojunctions via self-combustion of ionic liquid with enhanced visible-light photocatalytic activities, Appl. Catal. B Environ. 150–151 (2014) 574–584, https://doi.org/10.1016/j.apcatb.2014.01.009.
[45] J. Sharma, P. Dhiman, A. Kumar, E.A. Dawi, G. Rana, G. Sharma, 2D–2D g-C3N5/Bi24O31Br10 S-scheme nanostructures with increased photocatalytic efficiency for crystal violet removal, Chem. Eng. Res. Des. 195 (2023) 432–446, https://doi.org/10.1016/j.cherd.2023.05.059.
[46] J. Li, L. Cai, J. Shang, Y. Yu, L. Zhang, Giant enhancement of internal electric field boosting bulk charge separation for photocatalysis, Adv. Mater. 28 (2016) 4059–4064, https://doi.org/10.1002/adma.201600301.
[47] Y. Yu, C. Cao, H. Liu, P. Li, F. Wei, Y. Jiang, W. Song, A Bi/BiOCl heterojunction photocatalyst with enhanced electron–hole separation and excellent visible light photodegrading activity, J. Mater. Chem. A 2 (2014) 1677–1681, https://doi.org/10.1039/C3TA14494A.
[48] J. Sharma, P. Dhiman, R.A. Alshgari, Z.A. Alothman, A. Kumar, G. Sharma, G. Rana, Advances in photocatalytic environmental and clean energy applications of bismuth-rich oxy halides-based heterojunctions: a review, Mater. Today Sustain. 21 (2023) 100327, https://doi.org/10.1016/j.mtsust.2023.100327.
[49] H. Li, L. Zhang, Oxygen vacancy induced selective silver deposition on the {001} facets of BiOCl single-crystalline nanosheets for enhanced Cr(<scp>vi</scp>) and sodium pentachlorophenate removal under visible light, Nanoscale 6 (2014) 7805–7810, https://doi.org/10.1039/C4NR01315H.
[50] Z. Zhang, Y. Zhou, S. Yu, M. Chen, F. Wang, Ag-BiOCl nanocomposites prepared by the oxygen vacancy induced photodeposition method with improved visible light photocatalytic activity, Mater. Lett. 150 (2015) 97–100, https://doi.org/10.1016/j.matlet.2015.03.011.
[51] Y. Jia, Y. Yang, W. Guo, Q. Qin, X. Yang, Y. Guo, Y. Guo, Simulated sunlight photocatalytic degradation of aqueous p-nitrophenol and bisphenol A in a Pt/BiOBr film-coated quartz fiber photoreactor, Dalton Trans. (2003) 44 (2015) 9439–9449, https://doi.org/10.1039/c5dt00417a.
[52] R. Saraf, C. Shivakumara, S. Behera, N. Dhananjaya, H. Nagabhushana, Synthesis of Eu 3 + -activated BiOF and BiOBr, 2015, pp. 9241–9254.
[53] A. Dash, S. Sarkar, V.N.K.B. Adusumalli, V. Mahalingam, Microwave synthesis, photoluminescence, and photocatalytic activity of PVA-functionalized Eu 3+ -doped BiOX (X = Cl, Br, I) nanoflakes, Langmuir 30 (2014) 1401–1409, https://doi.org/10.1021/la403996m.
[54] H. Lin, X. Li, J. Cao, S. Chen, Y. Chen, Novel I–doped BiOBr composites: modulated valence bands and largely enhanced visible light phtotocatalytic activities, Catal. Commun. 49 (2014) 87–91, https://doi.org/10.1016/j.catcom.2014.02.010.
[55] Z. Wei, J. Liu, W. Fang, Z. Qin, Z. Jiang, W. Shangguan, A visible-light driven novel layered perovskite oxyhalide Bi 4 MO 8 X (M = Nb, Ta; X = Cl, Br) constructed using BiOX (X = Cl, Br) for enhanced photocatalytic hydrogen evolution, Catal. Sci. Technol. 8 (2018) 3774–3784, https://doi.org/10.1039/C8CY00959G.
[56] J. Li, K. Zhao, Y. Yu, L. Zhang, Facet-level mechanistic insights into general homogeneous carbon doping for enhanced solar-to-hydrogen conversion, Adv. Funct. Mater. 25 (2015) 2189–2201, https://doi.org/10.1002/adfm.201404178.

[57] L. Zhang, M. Jaroniec, Toward designing semiconductor-semiconductor heterojunctions for photocatalytic applications, Appl. Surf. Sci. 430 (2018) 2–17, https://doi.org/10.1016/j.apsusc.2017.07.192.
[58] J. Low, J. Yu, M. Jaroniec, S. Wageh, A.A. Al-Ghamdi, Heterojunction photocatalysts, Adv. Mater. 29 (2017) 1–20, https://doi.org/10.1002/adma.201601694.
[59] S. Wang, J.H. Yun, B. Luo, T. Butburee, P. Peerakiatkhajohn, S. Thaweesak, M. Xiao, L. Wang, Recent progress on visible light responsive heterojunctions for photocatalytic applications, J. Mater. Sci. Technol. 33 (2017) 1–22, https://doi.org/10.1016/j.jmst.2016.11.017.
[60] O.A. Arotiba, B.O. Orimolade, B.A. Koiki, Visible light driven photoelectrocatalytic semiconductor heterojunction anodes for water treatment applications, Curr. Opin. Electrochem. (2020) 1–10, https://doi.org/10.1016/j.coelec.2020.03.018.
[61] M. Lin, H. Chen, Z. Zhang, X. Wang, Engineering interface structures for heterojunction photocatalysts, Phys. Chem. Chem. Phys. 25 (2023) 4388–4407, https://doi.org/10.1039/D2CP05281D.
[62] L. Zhang, J. Zhang, H. Yu, J. Yu, Emerging S-scheme photocatalyst, Adv. Mater. 34 (2022) 10, https://doi.org/10.1002/adma.202107668.
[63] H. Li, W. Tu, Y. Zhou, Z. Zou, Z-Scheme photocatalytic systems for promoting photocatalytic performance: recent progress and future challenges, Adv. Sci. 3 (2016) 21, https://doi.org/10.1002/advs.201500389.
[64] Q. Xu, L. Zhang, J. Yu, S. Wageh, A.A. Al-Ghamdi, M. Jaroniec, Direct Z-scheme photocatalysts: principles, synthesis, and applications, Mater. Today 21 (2018) 1042–1063, https://doi.org/10.1016/j.mattod.2018.04.008.
[65] L. Wang, C. Bie, J. Yu, Challenges of Z-scheme photocatalytic mechanisms, Trends Chem. 4 (2022) 973–983, https://doi.org/10.1016/j.trechm.2022.08.008.
[66] Y. Ren, Y. Li, G. Pan, N. Wang, Y. Xing, Z. Zhang, Recent progress in CdS-based S-scheme photocatalysts, J. Mater. Sci. Technol. 171 (2024) 162–184, https://doi.org/10.1016/j.jmst.2023.06.052.
[67] C. Nie, X. Wang, P. Lu, Y. Zhu, X. Li, H. Tang, Advancements in S-scheme heterojunction materials for photocatalytic environmental remediation, J. Mater. Sci. Technol. 169 (2024) 182–198, https://doi.org/10.1016/j.jmst.2023.06.011.
[68] Q. Xu, L. Zhang, B. Cheng, J. Fan, J. Yu, S-scheme heterojunction photocatalyst, Chem 6 (2020) 1543–1559, https://doi.org/10.1016/j.chempr.2020.06.010.
[69] J. Fu, Q. Xu, J. Low, C. Jiang, J. Yu, Ultrathin 2D/2D WO3/g-C3N4 step-scheme H2-production photocatalyst, Appl. Catal. B Environ. 243 (2019) 556–565, https://doi.org/10.1016/j.apcatb.2018.11.011.
[70] L. Wang, B. Zhu, J. Zhang, J.B. Ghasemi, M. Mousavi, J. Yu, S-scheme heterojunction photocatalysts for CO2 reduction, Matter 5 (2022) 4187–4211, https://doi.org/10.1016/j.matt.2022.09.009.
[71] J. Liu, J. Shi, H. Deng, Current status of research on BiOX-based heterojunction photocatalytic systems: synthesis methods, photocatalytic applications and prospects, J. Environ. Chem. Eng. 11 (2023) 110311, https://doi.org/10.1016/j.jece.2023.110311.
[72] W.L. Huang, Q. Zhu, DFT calculations on the electronic structures of BiOX (X = F, Cl, Br, I) photocatalysts with and without semicore Bi 5d states, J. Comput. Chem. 30 (2009) 183–190, https://doi.org/10.1002/jcc.21055.
[73] J. Liu, Y. Li, L. Huang, C. Wang, L. Yang, J. Liu, C. Huang, Y. Song, Fabrication of novel narrow/wide band gap Bi4O5I2/BiOCl heterojunction with high antibacterial and degradation efficiency under LED and sunlight, Appl. Surf. Sci. 567 (2021) 150713, https://doi.org/10.1016/j.apsusc.2021.150713.
[74] X. Dou, C. Zhang, H. Shi, The simultaneous promotion of Cr (VI) photoreduction and tetracycline removal over 3D/2D Cu2O/BiOBr S-scheme nanostructures, Sep. Purif. Technol. 282 (2022) 120023, https://doi.org/10.1016/j.seppur.2021.120023.
[75] F. Yuan, Y. Zheng, D. Gao, L. Wang, X. Hu, Facile assembly and enhanced visible-light-driven photocatalytic activity of S-scheme BiOBr/g-C3N4 heterojunction for degrading xanthate in wastewater, J. Mol. Liq. 366 (2022) 120279, https://doi.org/10.1016/j.molliq.2022.120279.
[76] T. zhang, M. Maihemllti, K. Okitsu, D. Talifur, Y. Tursun, A. Abulizi, In situ self-assembled S-scheme BiOBr/pCN hybrid with enhanced photocatalytic activity for organic pollutant degradation and CO2 reduction, Appl. Surf. Sci. 556 (2021) 149828, https://doi.org/10.1016/j.apsusc.2021.149828.
[77] F. Yuan, Y. Zheng, D. Gao, D. Meng, L. Wang, X. Hu, Relationship of structure and enhanced photocatalytic activity of S-scheme BiOCl/g-C3N4 heterojunction for xanthate removal under visible light, Adv. Powder Technol. 34 (2023) 104049, https://doi.org/10.1016/j.apt.2023.104049.
[78] V.J. Nagaraj, M. Jacobs, K.M. Vattipalli, V.P. Annam, S. Prasad, Nanochannel-based electrochemical sensor for the detection of pharmaceutical contaminants in water, Environ. Sci. Process. Impacts. 16 (2013) 135–140, https://doi.org/10.1039/c3em00406f.
[79] D. Negrete-Bolagay, C. Zamora-Ledezma, C. Chuya-Sumba, F.B. De Sousa, D. Whitehead, F. Alexis, V.H. Guerrero, Persistent organic pollutants: the trade-off between potential risks and sustainable remediation methods, J. Environ. Manag. 300 (2021) 113737, https://doi.org/10.1016/j.jenvman.2021.113737.
[80] J. Sha, H. Xiong, C. Li, Z. Lu, J. Zhang, H. Zhong, W. Zhang, B. Yan, Harmful algal blooms and their eco-environmental indication, Chemosphere 274 (2021) 129912, https://doi.org/10.1016/j.chemosphere.2021.129912.
[81] S. Mompelat, B. Le Bot, O. Thomas, Occurrence and fate of pharmaceutical products and by-products, from resource to drinking water, Environ. Int. 35 (2009) 803–814, https://doi.org/10.1016/j.envint.2008.10.008.
[82] J. Wilkinson, P.S. Hooda, J. Barker, S. Barton, J. Swinden, Occurrence, fate and transformation of emerging contaminants in water: an overarching review of the field, Environ. Pollut. 231 (2017) 954–970, https://doi.org/10.1016/j.envpol.2017.08.032.
[83] N. Serpone, Y.M. Artemev, V.K. Ryabchuk, A.V. Emeline, S. Horikoshi, Light-driven advanced oxidation processes in the disposal of emerging pharmaceutical contaminants in aqueous media: a brief review, Curr. Opin. Green Sustainable Chem. 6 (2017) 18–33, https://doi.org/10.1016/j.cogsc.2017.05.003.
[84] N. Morin-Crini, E. Lichtfouse, G. Liu, V. Balaram, A.R.L. Ribeiro, Z. Lu, F. Stock, E. Carmona, M.R. Teixeira, L.A. Picos-Corrales, J.C. Moreno-Piraján, L. Giraldo, C. Li, A. Pandey, D. Hocquet, G. Torri, G. Crini, Worldwide cases of water pollution by emerging contaminants: a review, Environ. Chem. Lett. 20 (2022) 2311–2338, https://doi.org/10.1007/s10311-022-01447-4.
[85] L.A. Picos-Corrales, J.I. Sarmiento-Sánchez, J.P. Ruelas-Leyva, G. Crini, E. Hermosillo-Ochoa, J.A. Gutierrez-Montes, Environment-friendly approach toward the treatment of raw agricultural wastewater and river water via flocculation using chitosan and bean straw flour as bioflocculants, ACS Omega 5 (2020) 3943–3951, https://doi.org/10.1021/acsomega.9b03419.
[86] A.C. Collier, Pharmaceutical contaminants in potable water: potential concerns for pregnant women and children, EcoHealth 4 (2007) 164–171, https://doi.org/10.1007/s10393-007-0105-5.
[87] S. Jan, A.K. Mishra, M.A. Bhat, M.A. Bhat, A.T. Jan, Pollutants in aquatic system: a frontier perspective of emerging threat and strategies to solve the crisis for safe drinking water, Environ. Sci. Pollut. Res. 30 (2023) 113242–113279, https://doi.org/10.1007/s11356-023-30302-4.
[88] Y.A. Hajam, R. Kumar, A. Kumar, Environmental waste management strategies and vermi transformation for sustainable development, Environ. Challenges. 13 (2023) 100747, https://doi.org/10.1016/j.envc.2023.100747.
[89] B.O. Orimolade, A.O. Oladipo, A.O. Idris, F. Usisipho, S. Azizi, M. Maaza, S. L. Lebelo, B.B. Mamba, Advancements in electrochemical technologies for the removal of fluoroquinolone antibiotics in wastewater: a review, Sci. Total Environ. 881 (2023) 163522, https://doi.org/10.1016/j.scitotenv.2023.163522.
[90] T.L. Yusuf, B.O. Orimolade, D. Masekela, B. Mamba, N. Mabuba, The application of photoelectrocatalysis in the degradation of rhodamine B in aqueous solutions: a review, RSC Adv. 12 (2022) 26176–26191, https://doi.org/10.1039/D2RA04236C.
[91] H.E. Al-Hazmi, A. Mohammadi, A. Hejna, J. Majtacz, A. Esmaeili, S. Habibzadeh, M.R. Saeb, M. Badawi, E.C. Lima, J. Mąkinia, Wastewater reuse in agriculture: prospects and challenges, Environ. Res. 236 (2023) 116711, https://doi.org/10.1016/j.envres.2023.116711.
[92] A. Saravanan, P. Senthil Kumar, S. Jeevanantham, S. Karishma, B. Tajsabreen, P. R. Yaashikaa, B. Reshma, Effective water/wastewater treatment methodologies for toxic pollutants removal: processes and applications towards sustainable development, Chemosphere 280 (2021) 130595, https://doi.org/10.1016/j.chemosphere.2021.130595.
[93] F. Younas, A. Mustafa, Z.U.R. Farooqi, X. Wang, S. Younas, W. Mohy-Ud-Din, M. Ashir Hameed, M. Mohsin Abrar, A.A. Maitlo, S. Noreen, M.M. Hussain, Current and emerging adsorbent technologies for wastewater treatment: trends, limitations, and environmental implications, Water 13 (2021) 215, https://doi.org/10.3390/w13020215.
[94] M. Cirja, P. Ivashechkin, A. Schäffer, P.F.X. Corvini, Factors affecting the removal of organic micropollutants from wastewater in conventional treatment plants (CTP) and membrane bioreactors (MBR), Rev. Environ. Sci. Bio/Technology. 7 (2008) 61–78, https://doi.org/10.1007/s11157-007-9121-8.
[95] N. Gaur, K. Narasimhulu, P. Y, Recent advances in the bio-remediation of persistent organic pollutants and its effect on environment, J. Clean. Prod. 198 (2018) 1602–1631, https://doi.org/10.1016/j.jclepro.2018.07.076.
[96] S. Adithya, R.S. Jayaraman, A. Krishnan, R. Malolan, K.P. Gopinath, J. Arun, W. Kim, M. Govarthanan, A critical review on the formation, fate and degradation of the persistent organic pollutant hexachlorocyclohexane in water systems and waste streams, Chemosphere 271 (2021) 129866, https://doi.org/10.1016/j.chemosphere.2021.129866.
[97] L. Levidow, P. Lindgaard-Jørgensen, Å. Nilsson, S.A. Skenhall, D. Assimacopoulos, Process eco-innovation: assessing meso-level eco-efficiency in industrial water-service systems, J. Clean. Prod. 110 (2016) 54–65, https://doi.org/10.1016/j.jclepro.2014.12.086.
[98] S.F. Ahmed, M. Mofijur, S. Nuzhat, A.T. Chowdhury, N. Rafa, M.A. Uddin, A. Inayat, T.M.I. Mahlia, H.C. Ong, W.Y. Chia, P.L. Show, Recent developments in physical, biological, chemical, and hybrid treatment techniques for removing emerging contaminants from wastewater, J. Hazard Mater. 416 (2021) 125912, https://doi.org/10.1016/j.jhazmat.2021.125912.
[99] L. Rizzo, S. Malato, D. Antakyali, V.G. Beretsou, M.B. Đolić, W. Gernjak, E. Heath, I. Ivancev-Tumbas, P. Karaolia, A.R. Lado Ribeiro, G. Mascolo, C.S. McArdell, H. Schaar, A.M.T. Silva, D. Fatta-Kassinos, Consolidated vs new advanced treatment methods for the removal of contaminants of emerging concern from urban wastewater, Sci. Total Environ. 655 (2019) 986–1008, https://doi.org/10.1016/j.scitotenv.2018.11.265.
[100] H. Wang, X. Li, X. Zhao, C. Li, X. Song, P. Zhang, P. Huo, X. Li, A review on heterogeneous photocatalysis for environmental remediation: from semiconductors to modification strategies, Chin. J. Catal. 43 (2022) 178–214, https://doi.org/10.1016/S1872-2067(21)63910-4.
[101] S. Younis, K.-H. Kim, Heterogeneous photocatalysis scalability for environmental remediation: opportunities and challenges, Catalysts 10 (2020) 1109, https://doi.org/10.3390/catal10101109.
[102] B.O. Orimolade, A.O. Idris, U. Feleni, B. Mamba, Peroxymonosulfate assisted photoelectrocatalytic degradation of pharmaceuticals at a FTO-Bi2WO6 electrode: mechanism and kinetics studies, Catal. Commun. 169 (2022) 106481, https://doi.org/10.1016/j.catcom.2022.106481.

[103] K.H. Ng, S.Y. Lai, C.K. Cheng, Y.W. Cheng, C.C. Chong, Photocatalytic water splitting for solving energy crisis: myth, Fact or Busted? Chem. Eng. J. 417 (2021) 128847 https://doi.org/10.1016/j.cej.2021.128847.
[104] X. Tao, Y. Zhao, S. Wang, C. Li, R. Li, Recent advances and perspectives for solar-driven water splitting using particulate photocatalysts, Chem. Soc. Rev. 51 (2022) 3561–3608, https://doi.org/10.1039/D1CS01182K.
[105] S. Kreft, D. Wei, H. Junge, M. Beller, Recent advances on TiO2-based photocatalytic CO2 reduction, EnergyChem 2 (2020) 100044, https://doi.org/10.1016/j.enchem.2020.100044.
[106] F. Zhang, Y.-H. Li, M.-Y. Qi, Z.-R. Tang, Y.-J. Xu, Boosting the activity and stability of Ag-Cu2O/ZnO nanorods for photocatalytic CO2 reduction, Appl. Catal. B Environ. 268 (2020) 118380, https://doi.org/10.1016/j.apcatb.2019.118380.
[107] S. Cheriyamundath, S.L. Vavilala, Nanotechnology-based wastewater treatment, Water Environ. J. 35 (2021) 123–132, https://doi.org/10.1111/wej.12610.
[108] H. Tong, S. Ouyang, Y. Bi, N. Umezawa, M. Oshikiri, J. Ye, Nano-photocatalytic materials: possibilities and challenges, Adv. Mater. 24 (2012) 229–251, https://doi.org/10.1002/adma.201102752.
[109] Y.M. Hunge, A. Uchida, Y. Tominaga, Y. Fujii, A.A. Yadav, S.-W. Kang, N. Suzuki, I. Shitanda, T. Kondo, M. Itagaki, M. Yuasa, S. Gosavi, A. Fujishima, C. Terashima, Visible light-assisted photocatalysis using spherical-shaped BiVO4 photocatalyst, Catalysts 11 (2021) 460, https://doi.org/10.3390/catal11040460.
[110] J.C. Murillo-Sierra, A. Hernández-Ramírez, L. Hinojosa-Reyes, J.L. Guzmán-Mar, A review on the development of visible light-responsive WO3-based photocatalysts for environmental applications, Chem. Eng. J. Adv. 5 (2021) 100070, https://doi.org/10.1016/j.ceja.2020.100070.
[111] W. Zhu, J. Liu, S. Yu, Y. Zhou, X. Yan, Ag loaded WO3 nanoplates for efficient photocatalytic degradation of sulfanilamide and their bactericidal effect under visible light irradiation, J. Hazard Mater. 318 (2016) 407–416, https://doi.org/10.1016/j.jhazmat.2016.06.066.
[112] Y. Ma, Q. Liu, Q. Wang, D. Qu, J. Shi, Insight into the origin of photoreactivity of various well-defined Bi2WO6 crystals: exposed heterojunction-like surface and oxygen defects, RSC Adv. 6 (2016) 18916–18923, https://doi.org/10.1039/c5ra27295e.
[113] W. Zou, L. Zhang, L. Liu, X. Wang, J. Sun, S. Wu, Y. Deng, C. Tang, F. Gao, L. Dong, Engineering the Cu2O–reduced graphene oxide interface to enhance photocatalytic degradation of organic pollutants under visible light, Appl. Catal. B Environ. 181 (2016) 495–503, https://doi.org/10.1016/j.apcatb.2015.08.017.
[114] J.-H. Yoo, M. Ji, J.H. Kim, C.-H. Ryu, Y.-I. Lee, Facile synthesis of hierarchical CuS microspheres with high visible-light-driven photocatalytic activity, J. Photochem. Photobiol. Chem. 401 (2020) 112782, https://doi.org/10.1016/j.jphotochem.2020.112782.
[115] H. Ullah, E. Viglašová, M. Galamboš, Visible light-driven photocatalytic rhodamine B degradation using CdS nanorods, Processes 9 (2021) 263, https://doi.org/10.3390/pr9020263.
[116] Z. Li, X. Meng, Z. Zhang, Recent development on MoS2-based photocatalysis: a review, J. Photochem. Photobiol. C Photochem. Rev. 35 (2018) 39–55, https://doi.org/10.1016/j.jphotochemrev.2017.12.002.
[117] N. Thomas, S. Mathew, K.M. Nair, K. O'Dowd, P. Forouzandeh, A. Goswami, G. McGranaghan, S.C. Pillai, 2D MoS2: structure, mechanisms, and photocatalytic applications, Mater. Today Sustain. 13 (2021) 100073, https://doi.org/10.1016/j.mtsust.2021.100073.
[118] D. Panchal, A. Sharma, S. Pal, Engineered MoS2 nanostructures for improved photocatalytic applications in water treatment, Mater, Today Sustain. 21 (2023) 100264, https://doi.org/10.1016/j.mtsust.2022.100264.
[119] A.A. Baoum, M.S. Amin, Excellent photocatalytic degradation of tetracycline under visible illumination utilizing Ag2S/Ag2O heterojunction, Opt. Mater. 137 (2023) 113594, https://doi.org/10.1016/j.optmat.2023.113594.
[120] Z. Zhang, Z. Xing, K. Wang, T. Cheng, Z. Li, W. Zhou, Bi2S3@Ag2S nano-heterojunction decorated self-floating carbon fiber cloth and enhanced solar-driven photothermal-photocatalytic performance, Chemosphere 271 (2021) 129500, https://doi.org/10.1016/j.chemosphere.2020.129500.
[121] R. Elshypany, H. Selim, K. Zakaria, A.H. Moustafa, S.A. Sadeek, S.I. Sharaa, P. Raynaud, A.A. Nada, Elaboration of Fe3O4/ZnO nanocomposite with highly performance photocatalytic activity for degradation methylene blue under visible light irradiation, Environ. Technol. Innov. 23 (2021) 101710, https://doi.org/10.1016/j.eti.2021.101710.
[122] A.M. Alansi, M. Al-Qunaibit, I.O. Alade, T.F. Qahtan, T.A. Saleh, Visible-light responsive BiOBr nanoparticles loaded on reduced graphene oxide for photocatalytic degradation of dye, J. Mol. Liq. 253 (2018) 297–304, https://doi.org/10.1016/j.molliq.2018.01.034.
[123] X. Jia, Q. Han, H. Liu, S. Li, H. Bi, A dual strategy to construct flowerlike S-scheme BiOBr/BiOAc1−Br heterojunction with enhanced visible-light photocatalytic activity, Chem. Eng. J. 399 (2020) 125701, https://doi.org/10.1016/j.cej.2020.125701.
[124] X. Xiong, L. Ding, Q. Wang, Y. Li, Q. Jiang, J. Hu, Synthesis and photocatalytic activity of BiOBr nanosheets with tunable exposed {0 1 0} facets, Appl. Catal. B Environ. 188 (2016) 283–291, https://doi.org/10.1016/j.apcatb.2016.02.018.
[125] G. Fan, K. Hu, X. Li, M. Xia, Z. Chen, S. Chen, J. Luo, J. Zou, Z. Hong, K. Xu, Highly efficient S-scheme AgBr/BiOBr with visible light photocatalytic performance for carbamazepine degradation: mechanism insight and toxicity assessment, J. Environ. Chem. Eng. 11 (2023) 110918, https://doi.org/10.1016/j.jece.2023.110918.
[126] C. Wen, D. Li, J. Zhong, Z. Wang, S. Huang, H. Liu, J. Wu, P. Chen, W. Lv, G. Liu, In situ synthesis of S-scheme AgBr/BiOBr for efficient degradation of sulfonamide antibiotics: synergistic effects of oxygen vacancies and heterojunctions promote exciton dissociation, Chem. Eng. J. 450 (2022) 138075, https://doi.org/10.1016/j.cej.2022.138075.
[127] X. Zhang, W. Huang, Z. Xia, M. Xian, F. Bu, F. Liang, D. Feng, One-pot synthesis of S-scheme WO3/BiOBr heterojunction nanoflowers enriched with oxygen vacancies for enhanced tetracycline photodegradation, Sep. Purif. Technol. 290 (2022) 120897, https://doi.org/10.1016/j.seppur.2022.120897.
[128] C. Liu, S. Mao, H. Wang, Y. Wu, F. Wang, M. Xia, Q. Chen, Peroxymonosulfate-assisted for facilitating photocatalytic degradation performance of 2D/2D WO3/BiOBr S-scheme heterojunction, Chem. Eng. J. 430 (2022) 132806, https://doi.org/10.1016/j.cej.2021.132806.
[129] C. Du, S. He, Y. Xing, Q. Zhao, C. Yu, X. Su, J. Feng, J. Sun, S. Dong, Fabricating S-scheme BiOBr/Zn2In2S5 heterojunction for synergistic adsorption-photocatalytic degradation of tetracycline, Mater. Today Phys. 27 (2022) 100827, https://doi.org/10.1016/j.mtphys.2022.100827.
[130] X. Li, J. Xiong, X. Gao, J. Ma, Z. Chen, B. Kang, J. Liu, H. Li, Z. Feng, J. Huang, Novel BP/BiOBr S-scheme nano-heterojunction for enhanced visible-light photocatalytic tetracycline removal and oxygen evolution activity, J. Hazard Mater. 387 (2020) 121690, https://doi.org/10.1016/j.jhazmat.2019.121690.
[131] X. Dou, Y. Chen, H. Shi, CuBi2O4/BiOBr composites promoted PMS activation for the degradation of tetracycline: S-scheme mechanism boosted Cu2+/Cu+ cycle, Chem. Eng. J. 431 (2022) 134054, https://doi.org/10.1016/j.cej.2021.134054.
[132] S. Kokilavani, I.A. Alaraidh, M.K. Okla, P. Chandran, A. Mohebaldin, W. Soufan, A.A. Al-ghamdi, M.A. Abdel-Maksoud, H. AbdElgawad, A.M. Thomas, L.L. Raju, S. Sudheer Khan, Efficient photocatalytic degradation of methyl orange and malachite green by Ag3PO4 decorated BiOBr nanoflower under visible light: performance evaluation, mechanism insights and toxicology of the by-products, J. Alloys Compd. 909 (2022) 164703, https://doi.org/10.1016/j.jallcom.2022.164703.
[133] T. Zhang, Q. Yang, H. Li, J. Zhong, J. Li, H. Yang, Photocatalytic properties of BiOBr/g-C3N4 heterojunctions originated from S-scheme separation and transfer of interfacial charge pairs, Opt. Mater. 131 (2022) 112649, https://doi.org/10.1016/j.optmat.2022.112649.
[134] T. Xian, H. Li, X. Sun, Y. Huo, L. Di, C. Sun, H. Yang, S-scheme In2O3Nanoparticle/BiOBr nanoplate heterojunctions for improved photocatalytic dye degradation and Cr(VI) reduction, ACS Appl. Nano Mater. 5 (2022) 15260–15271, https://doi.org/10.1021/acsanm.2c03352.
[135] A. Paul Chowdhury, B.H. Shambharkar, Synthesis and characterization of BiOCl-CoWO 4 nanocomposites with improved photocatalytic activity, Int. J. Appl. Ceram. Technol. 17 (2020) 1467–1478, https://doi.org/10.1111/ijac.13366.
[136] Q. Wang, J. Hui, Y. Huang, Y. Ding, Y. Cai, S. Yin, Z. Li, B. Su, The preparation of BiOCl photocatalyst and its performance of photodegradation on dyes, Mater. Sci. Semicond. Process. 17 (2014) 87–93, https://doi.org/10.1016/j.mssp.2013.08.018.
[137] J. Jiang, L. Zhang, H. Li, W. He, J.J. Yin, Self-doping and surface plasmon modification induced visible light photocatalysis of BiOCl, Nanoscale 5 (2013) 10573–10581, https://doi.org/10.1039/c3nr03597b.
[138] X. Yang, S. Sun, J. Cui, M. Yang, Y. Luo, S. Liang, Synthesis, functional modifications, and diversified applications of hybrid BiOCl-based heterogeneous photocatalysts: a review, Cryst. Growth Des. 21 (2021) 6576–6618, https://doi.org/10.1021/acs.cgd.1c00866.
[139] L. Yang, J. Wang, Y. Zhang, B. Zhou, P. Tan, J. Pan, Construction of S-scheme BiOCl/CdS composite for enhanced photocatalytic degradation of antibiotic, J. Mater. Sci. Mater. Electron. 33 (2022) 13303–13315, https://doi.org/10.1007/s10854-022-08269-8.
[140] X. Yuan, J. Yang, Y. Yao, H. Shen, Y. Meng, B. Xie, Z. Ni, S. Xia, Preparation, characterization and photodegradation mechanism of 0D/2D Cu2O/BiOCl S-scheme heterojunction for efficient photodegradation of tetracycline, Sep. Purif. Technol. 291 (2022) 120965, https://doi.org/10.1016/j.seppur.2022.120965.
[141] K. Xu, J. Shen, S. Zhang, D. Xu, X. Chen, Efficient interfacial charge transfer of BiOCl-In2O3 step-scheme heterojunction for boosted photocatalytic degradation of ciprofloxacin, J. Mater. Sci. Technol. 121 (2022) 236–244, https://doi.org/10.1016/j.jmst.2021.12.070.
[142] S. Wu, X. Yu, J. Zhang, Y. Zhang, Y. Zhu, M. Zhu, Construction of BiOCl/CuBi2O4 S-scheme heterojunction with oxygen vacancy for enhanced photocatalytic diclofenac degradation and nitric oxide removal, Chem. Eng. J. 411 (2021) 128555, https://doi.org/10.1016/j.cej.2021.128555.
[143] H.P. Gogoi, A. Dehingia, A. Singh, P. Barman, Heterostructured BiOCl–LaOCl S-scheme composites with improved visible-light photocatalytic activity on Rhodamine B dye, J. Phys. Chem. Solid. 174 (2023) 111163, https://doi.org/10.1016/j.jpcs.2022.111163.
[144] H. Guo, Y. Deng, H. Yin, J. Liu, S. Zou, Fabricating BiOCl nanoflake/FeOCl nanospindle heterostructures for efficient visible-light photocatalysis, Molecules 28 (2023) 6949, https://doi.org/10.3390/molecules28196949.
[145] H. Li, D. Wang, C. Miao, F. Xia, Y. Wang, Y. Wang, C. Liu, G. Che, g-C3N4/BiOI S-scheme heterojunction: a 2D/2D model platform for visible-light-driven photocatalytic CO2reduction and pollutant degradation, J. Environ. Chem. Eng. 10 (2022) 108201, https://doi.org/10.1016/j.jece.2022.108201.
[146] K. Dou, C. Peng, R. Wang, H. Cao, C. Yao, J. Qiu, J. Liu, N. Tsidaeva, W. Wang, S-scheme tubular g-C3N4/BiOI heterojunctions for boosting photodegradation of tetracycline and Cr(VI): mechanism insight, degradation pathway and DFT calculation, Chem. Eng. J. 455 (2023) 140813, https://doi.org/10.1016/j.cej.2022.140813.
[147] F. Mu, B. Dai, Y. Wu, G. Yang, S. Li, L. Zhang, J. Xu, Y. Liu, W. Zhao, 2D/3D S-scheme heterojunction of carbon nitride/iodine-deficient bismuth oxyiodide for photocatalytic hydrogen production and bisphenol A degradation, J. Colloid Interface Sci. 612 (2022) 722–736, https://doi.org/10.1016/j.jcis.2021.12.196.

[148] S. Lei, R. Luo, H. Li, J. Chen, J. Zhong, J. Li, Ionic liquid assisted in-situ construction of S-scheme BiOI/Bi2WO6 heterojunctions with improved sunlight-driven photocatalytic performance, Inorg. Chem. Commun. 121 (2020) 108192, https://doi.org/10.1016/j.inoche.2020.108192.
[149] Z. Xu, C. Qin, J. Zhong, S. Huang, M. Li, S. Zhang, H. Yang, L. Ma, In-situ preparation of S-scheme BiOI/BiVO4 heterojunctions with enhanced photocatalytic performance, Solid State Sci. 129 (2022) 106908, https://doi.org/10.1016/j.solidstatesciences.2022.106908.
[150] T. Bavani, M. Preeyanghaa, B. Neppolian, J. Madhavan, D. Balaji, A hybrid S-scheme WS 2/BiOI heterojunction photocatalyst for wastewater treatment, ChemPhotoChem 7 (2023) 1–10, https://doi.org/10.1002/cptc.202300024.
[151] C. Lai, L. Luo, Y. Chen, J. Chen, J. Zhong, In-situ construction of S-scheme Bi4O5I2/BiOI heterojunctions with enriched oxygen vacancies and enhanced photocatalytic properties towards destruction of rhodamine B and tetracycline, Inorg. Chem. Commun. 158 (2023) 111622, https://doi.org/10.1016/j.inoche.2023.111622.
[152] H. Ding, A. Hannan Zahid, Q. Han, Synthesis of 3D flowerlike S-scheme Bi4O5I2/BiOI heterojunction with synergistic effect of adsorption and photocatalysis, Mater. Sci. Eng. B 289 (2023) 116209, https://doi.org/10.1016/j.mseb.2022.116209.
[153] J. Wang, S. Li, K. Yang, T. Zhang, S. Jiang, X. Li, B. Li, Bacitracin-controlled BiOI/Bi5O7I nanosheet assembly and S-scheme heterojunction formation for enhanced photocatalytic performances, ACS Appl. Nano Mater. 5 (2022) 6736–6749, https://doi.org/10.1021/acsanm.2c00760.
[154] J. Yi, R. Xie, R. Liu, M. Li, H. Zeng, Q. Chen, L. Cai, N. Li, C. Yu, Z. Liu, D. Li, Hollow BiOI/Bi5O7I hierarchical microsphere with S-scheme heterostructure for efficiently removal of tetracycline hydrochloride, J. Water Process Eng. 53 (2023) 103798, https://doi.org/10.1016/j.jwpe.2023.103798.
[155] J. Lu, J. Bie, S. Fu, J. Wu, Q. Huang, P. He, Z. Yang, X. Zhang, H. Zhu, P. Deng, Construction of a novel two-dimensional AgBiO3/BiOBr step-scheme heterojunction for enhanced broad-spectrum photocatalytic performance, RSC Adv. 12 (2022) 20628–20639, https://doi.org/10.1039/d2ra03157d.
[156] X. Yan, T. Zhang, S. Meng, P. Zhou, Y. Xu, Y. Wang, M. Xie, BaFe12O19/BiOBr S-scheme heterojunction magnetic nanosheets for high-efficiency photocatalytic degradation of 2-mercaptobenzothiazole, Sep. Purif. Technol. 326 (2023) 124746, https://doi.org/10.1016/j.seppur.2023.124746.
[157] G. Peng, Y. Xie, Y. Wang, Q. Yu, Y. Huang, S. Liu, L. Lu, Triggering sustainable regeneration of Fe2+ by S-scheme Bi2Fe4O9/BiOBr heterojunction toward highly efficient peroxymonosulfate activation for visible-light-driven removal of thiabendazole, Appl. Surf. Sci. 631 (2023) 157567, https://doi.org/10.1016/j.apsusc.2023.157567.
[158] K. Liu, L. Wang, T. Fu, H. Zhang, C. Lu, Z. Tong, Y. Yang, Y. Peng, Oxygen-functionalized Ti3C2 MXene/exfoliated montmorillonite supported S-scheme BiOBr/Bi2MoO6 heterostructures for efficient photocatalytic quinolone antibiotics degradation, Chem. Eng. J. 457 (2023) 141271, https://doi.org/10.1016/j.cej.2023.141271.
[159] K. Liu, T. Fu, L. Wang, J. Yan, J. Sun, J. Zhang, X. Wei, Z. Tong, H. Zhang, Unique roles of exfoliated bentonite in S-scheme BiOBr/Bi2MoO6 heterojunction for boosted ciprofloxacin degradation, Sep. Purif. Technol. 323 (2023) 124427, https://doi.org/10.1016/j.seppur.2023.124427.
[160] X. hua Zheng, W. Chen, M. nan Xu, C. bin Cai, F. er Yang, Photocatalytic properties of BiOBr/BiOCl/AgBr ternary photocatalysts for degradation of RhB dye, J. Nanoparticle Res. 25 (2023) 1–16, https://doi.org/10.1007/s11051-023-05748-9.
[161] G. Huang, K. Liu, Y. Muhammad, T. Fu, L. Wang, J. Nong, S. Xu, L. Jiang, Z. Tong, H. Zhang, Integrating magnetized bentonite and pinecone-like BiOBr/BiOI Step-scheme heterojunctions as novel recyclable photocatalyst for efficient antibiotic degradation, J. Ind. Eng. Chem. 122 (2023) 482–499, https://doi.org/10.1016/j.jiec.2023.03.010.
[162] Z. Zan, X. Li, X. Gao, J. Huang, Y. Luo, L. Han, 0D/2D carbon nitride quantum dots (CNQDs)/BiOBr S-scheme heterojunction for robust photocatalytic degradation and H2O2 production, Wuli Huaxue Xuebao/Acta Phys. - Chim. Sin. 39 (2023) 1–13, https://doi.org/10.3866/PKU.WHXB202209016.
[163] M. Gao, W. Li, X. Su, Z. Li, X. Ding, X. Du, Y. Ren, H. Zhang, J. Feng, T. Wei, A regenerable Cu2O/BiOBr S-scheme heterojunction photocatalysts for efficient photocatalytic degradation of mixed organic pollutants, Sep. Purif. Technol. 313 (2023) 123447, https://doi.org/10.1016/j.seppur.2023.123447.
[164] D.A. Sabit, S.E. Ebrahim, Z.H. Jabbar, Immobilization of 0D CuO/ZnFe2O4 nanoparticles onto 2D BiOBr nanoplates as dual S-scheme heterostructure for boosting photocatalytic oxidation of levofloxacin in wastewater: magnetic reusability and mechanism insights, J. Photochem. Photobiol. Chem. 443 (2023) 114849, https://doi.org/10.1016/j.jphotochem.2023.114849.
[165] L. Wang, Q. Li, J. Song, X. Lu, Z. Tian, Y. Liu, J. Zhang, Construction of hierarchical FeIn2S4/BiOBr S-scheme heterojunction with enhanced visible-light photocatalytic performance for antibiotics degradation, Adv. Powder Technol. 33 (2022) 103859, https://doi.org/10.1016/j.apt.2022.103859.
[166] X. Lian, S. Chen, F. He, S. Dong, E. Liu, H. Li, K. Xu, Photocatalytic degradation of ammonium dinitramide over novel S-scheme g-C3N4/BiOBr heterostructure nanosheets, Sep. Purif. Technol. 286 (2022) 120449, https://doi.org/10.1016/j.seppur.2022.120449.
[167] M. Song, M. Li, H. Li, P. Wang, Y. Wu, L. Li, Novel through-holes g-C3N4/BiOBr S-scheme heterojunction: charge relocation mechanism and DFT insights, Surf. Interfaces 41 (2023) 103227, https://doi.org/10.1016/j.surfin.2023.103227.
[168] S. Li, C. Wang, K. Dong, P. Zhang, X. Chen, X. Li, MIL-101(Fe)/BiOBr S-scheme photocatalyst for promoting photocatalytic abatement of Cr(VI) and enrofloxacin antibiotic: performance and mechanism, Chin. J. Catal. 51 (2023) 101–112, https://doi.org/10.1016/S1872-2067(23)64479-1.
[169] Q. Li, L. Wang, J. Song, Y. Huang, G. Xie, Y. Liu, H. Li, Novel 2D/2D S-scheme Ni doped SnS2/BiOBr heterostructures with enhanced photocatalytic activity, Arab. J. Chem. 16 (2023) 105081, https://doi.org/10.1016/j.arabjc.2023.105081.
[170] Y. Qing, Y. Li, L. Cao, Y. Yang, L. Han, P. Dansawad, H. Gao, W. Li, Rationally designed C-PANI/BiOBr STEP-scheme heterojunction photocatalyst for boosting photodegradation of 17β-estradiol, Sep. Purif. Technol. 314 (2023) 123545, https://doi.org/10.1016/j.seppur.2023.123545.
[171] W. Wang, X. Li, F. Deng, J. Liu, X. Gao, J. Huang, J. Xu, Z. Feng, Z. Chen, L. Han, Novel organic/inorganic PDI-Urea/BiOBr S-scheme heterojunction for improved photocatalytic antibiotic degradation and H2O2 production, Chin. Chem. Lett. 33 (2022) 5200–5207, https://doi.org/10.1016/j.cclet.2022.01.058.
[172] Y. Feng, Y. Tao, J. Qu, Y. Zhang, S-scheme P-doped g-C3N4/BiOBr heterojunction with oxygen vacancy for efficient photocatalytic degradation of phenanthrene: enhance molecular oxygen activation and mechanism insights, Chem. Eng. J. 472 (2023) 145053, https://doi.org/10.1016/j.cej.2023.145053.
[173] S. Lin, Z. Sun, X. Qiu, H. Li, P. Ren, H. Xie, L. Guo, Construction of embedded sulfur-doped g-C3N4/BiOBr S-scheme heterojunction for highly efficient visible light photocatalytic degradation of organic compound rhodamine B, Small (2023) 1–17, https://doi.org/10.1002/smll.202306983, 2306983.
[174] B.H. Graimed, Z.H. Jabbar, M.M. Alsunbuli, S.H. Ammar, S.A. Hamood, A. G. Taher, D.A. Sabit, Rational design of 1D TaON nano-fibrous network decorated 2D BiOBr nanosheets for sustainable photocatalytic detoxification of antibiotics in wastewater via S-scheme heterostructure system, J. Water Process Eng. 54 (2023) 104059, https://doi.org/10.1016/j.jwpe.2023.104059.
[175] D.A. Sabit, S.E. Ebrahim, Fabrication of magnetic BiOBr/ZnFe2O4/CuO heterojunction for improving the photocatalytic destruction of malachite green dye under LED irradiation: dual S-scheme mechanism, Mater. Sci. Semicond. Process. 163 (2023) 107559, https://doi.org/10.1016/j.mssp.2023.107559.
[176] L. Feng, H. Yu, G. Yang, X. Liang, T. Zhang, C. Zhang, H. Xu, T. Liu, M. Xu, W. Yang, Novel 3D@2D/2D HHSS@BiOBr/Znln2S4 S-scheme photocatalyst for efficient adsorption-photocatalytic-photosensitization synergistic degradation of organics, Appl. Surf. Sci. 640 (2023) 158340, https://doi.org/10.1016/j.apsusc.2023.158340.
[177] L. Zhang, J. Hao, Z. Jia, C. Wang, Visible light responding β-SiC/BiOBr S-scheme heterojunction photocatalyst with improved photodegradation efficiency of bisphenol A, J. Solid State Chem. 325 (2023) 124167, https://doi.org/10.1016/j.jssc.2023.124167.
[178] Y. Zheng, Y. Sun, Construction of a flower-like S-scheme Bi2WO6/BiOCl nano-heterojunction with enhanced visible-light photocatalytic properties, New J. Chem. 46 (2022) 21418–21427, https://doi.org/10.1039/d2nj04521d.
[179] A. Verma, E. Dhanaraman, W.T. Chen, Y.P. Fu, Optimization of intercalated 2D BiOCl sheets into Bi2WO6 flowers for photocatalytic NH3 production and antibiotic pollutant degradation, ACS Appl. Mater. Interfaces 15 (2023) 37540–37553, https://doi.org/10.1021/acsami.3c07489.
[180] F. Liu, Y. Wang, D. Xu, F. Sun, S. Zhang, W. Wang, X. Li, W. Yu, H. Yu, X. Dong, Full-spectrum-responsive 1D/2D BiVO4:Er3+,Yb3+/BiOCl core-shell S-scheme heterostructure with boosted charge transport and redox capacity for the efficient removal of organic pollutants, Ceram. Int. 49 (2023) 13371–13385, https://doi.org/10.1016/j.ceramint.2022.12.212.
[181] H. Ma, J. Liu, Y. Wang, S. Zuo, Y. Yu, B. Li, Construction of novel flower-like functionalized black phosphorus nanosheets/P-doped BiOCl S-scheme photocatalysts with improved photocatalytic activity in RhB and Cr(vi) degradation, Mater. Adv. 3 (2022) 7546–7558, https://doi.org/10.1039/d2ma00290f.
[182] M. Cai, Y. Liu, K. Dong, C. Wang, S. Li, A novel S-scheme heterojunction of Cd0.5Zn0.5S/BiOCl with oxygen defects for antibiotic norfloxacin photodegradation: performance, mechanism, and intermediates toxicity evaluation, J. Colloid Interface Sci. 629 (2023) 276–286, https://doi.org/10.1016/j.jcis.2022.08.136.
[183] L. Shi, J. Yin, Y. Liu, H. Liu, H. Zhang, H. Tang, Embedding Cu3P quantum dots onto BiOCl nanosheets as a 0D/2D S-scheme heterojunction for photocatalytic antibiotic degradation, Chemosphere 309 (2022) 136607, https://doi.org/10.1016/j.chemosphere.2022.136607.
[184] M. Liu, P. Ye, M. Wang, L. Wang, C. Wu, J. Xu, Y. Chen, 2D/2D Bi-MOF-derived BiOCl/MoS2nanosheets S-scheme heterojunction for effective photocatalytic degradation, J. Environ. Chem. Eng. 10 (2022) 108436, https://doi.org/10.1016/j.jece.2022.108436.
[185] Y. Huang, F. Chen, Z. Guan, Y. Luo, L. Zhou, Y. Lu, B. Tian, J. Zhang, S-scheme BiOCl/MoSe2 heterostructure with enhanced photocatalytic activity for dyes and antibiotics degradation under sunlight irradiation, Sensors 22 (2022) 1–14, https://doi.org/10.3390/s22093344.
[186] S. Li, M. Cai, C. Wang, Y. Liu, N. Li, P. Zhang, X. Li, Rationally designed Ta3N5/BiOCl S-scheme heterojunction with oxygen vacancies for elimination of tetracycline antibiotic and Cr(VI): performance, toxicity evaluation and mechanism insight, J. Mater. Sci. Technol. 123 (2022) 177–190, https://doi.org/10.1016/j.jmst.2022.02.012.
[187] L. Hao, D. Teng, X. Guo, B. Wu, J. Wan, J. Zhang, J.-H. Yang, Construction of TiO2/BiOCl S-Scheme heterojunction and photocatalytic degradation of norfloxacin, J. Photochem. Photobiol. Chem. 444 (2023) 115004, https://doi.org/10.1016/j.jphotochem.2023.115004.
[188] Y. Kumar, A. Sudhaik, K. Sharma, Sonu, P. Raizada, A. Aslam Parwaz Khan, V. H. Nguyen, T. Ahamad, P. Singh, A.M. Asiri, Construction of magnetically separable novel arrow down dual S-scheme ZnIn2S4/BiOCl/FeVO4

heterojunction for improved photocatalytic activity, J. Photochem. Photobiol. Chem. 435 (2023) 114326, https://doi.org/10.1016/j.jphotochem.2022.114326.
[189] H. Luo, S. Dong, H. Li, S. Chen, J. Huang, K. Xu, Novel dual S-scheme BiOI/AgI/Bi2WO6 heterojunction with enhanced photocatalytic activity for highly efficient removal of organic pollutants, Opt. Mater. 140 (2023) 113842, https://doi.org/10.1016/j.optmat.2023.113842.
[190] T. Zhong, H. Wen, J. Ruan, B. Li, Y. Guo, Z. Lin, In situ construction of closely bonded S-scheme BiOI@Bi2O2(OH)(NO3) heterojunctions for boosted visible-light-driven photocatalytic activity, ACS Appl. Energy Mater. 5 (2022) 15729–15739, https://doi.org/10.1021/acsaem.2c03307.
[191] X. Jiang, H. Tan, X. Shi, X. Cheng, W. Hu, X. Hu, Preparation of Bi2O3/BiOI step-scheme heterojunction photocatalysts and their degradation mechanism of methylene blue, J. Wuhan Univ. Technol.-Materials Sci. Ed. 37 (2022) 801–806, https://doi.org/10.1007/s11595-022-2599-7.
[192] B. Dai, X. Chen, X. Yang, G. Yang, S. Li, L. Zhang, F. Mu, W. Zhao, D.Y.C. Leung, Designing S-scheme Au/g-C3N4/BiO1.2I0.6 plasmonic heterojunction for efficient visible-light photocatalysis, Sep. Purif. Technol. 287 (2022) 120531, https://doi.org/10.1016/j.seppur.2022.120531.
[193] X. Liao, T.-T. Li, H.-T. Ren, X. Zhang, B. Shen, J.-H. Lin, C.-W. Lou, Construction of BiOI/TiO2 flexible and hierarchical S-scheme heterojunction nanofibers membranes for visible-light-driven photocatalytic pollutants degradation, Sci. Total Environ. 806 (2022) 150698, https://doi.org/10.1016/j.scitotenv.2021.150698.
[194] X. Jia, C. Hu, H. Sun, J. Cao, H. Lin, X. Li, S. Chen, A dual defect co-modified S-scheme heterojunction for boosting photocatalytic CO2 reduction coupled with tetracycline oxidation, Appl. Catal. B Environ. 324 (2023) 122232, https://doi.org/10.1016/j.apcatb.2022.122232.
[195] Z. Li, D. Lan, Z. Li, J. Sun, S. Chen, J. Yang, J. Wei, Z. Yu, S. Wang, Y. Hou, Step-doped disulfide vacancies and functional groups synergistically enhance photocatalytic activity of S-scheme Cu3SnS4/L-BiOBr towards ciprofloxacin degradation, Chemosphere 301 (2022) 134684, https://doi.org/10.1016/j.chemosphere.2022.134684.
[196] K. GracePavithra, V. Jaikumar, P.S. Kumar, P. SundarRajan, A review on cleaner strategies for chromium industrial wastewater: present research and future perspective, J. Clean. Prod. 228 (2019) 580–593, https://doi.org/10.1016/j.jclepro.2019.04.117.
[197] S.H. Rimu, M.M. Rahman, Insight of chitosan-based nanocomposite for removal of hexavalent chromium from wastewater- a review, Int. J. Environ. Anal. Chem. 102 (2022) 6801–6818, https://doi.org/10.1080/03067319.2020.1817426.
[198] Y. Lu, L. Chen, C. Zhang, M. Yu, K. Lv, X. Li, B. Xi, Construction of oxidation-reduction bifunctional nano-purifiers: S-scheme faceted heterojunction BiOCl (110) nanosheets/TiO2(001) hollow nanocubes with abundant oxygen vacancies for balancing visible photocatalytic activity, J. Environ. Chem. Eng. 12 (2024) 111893, https://doi.org/10.1016/j.jece.2024.111893.
[199] C. Wang, H. Liu, G. Wang, F. Ye, S. Tao, X. Li, P. Qiu, Z. Huang, Ni (II) doping induced lattice distortion in Zn3In2S6/BiOBr-OVs for boosting photocatalytic removal of antibiotics and Cr (VI) performance, Sep. Purif. Technol. 324 (2023) 124457, https://doi.org/10.1016/j.seppur.2023.124457.
[200] J. Yang, Y. Hou, J. Sun, J. Liang, Z. Yu, H. Zhu, S. Wang, In-situ generation of oxygen vacancies and Bi0 clusters on MoSe2/Bi@BiOBr-OV via Fermi inter-level electron transfer for efficient elimination of chlorotetracycline and Cr (VI), Sep. Purif. Technol. 299 (2022) 121701, https://doi.org/10.1016/j.seppur.2022.121701.
[201] R. He, Z. Wang, F. Deng, X. Li, Y. Peng, Y. Deng, J. Zou, X. Luo, X. Liu, Tunable Bi-bridge S-scheme Bi2S3/BiOBr heterojunction with oxygen vacancy and SPR effect for efficient photocatalytic reduction of Cr(VI) and industrial electroplating wastewater treatment, Sep. Purif. Technol. 311 (2023) 123176, https://doi.org/10.1016/j.seppur.2023.123176.
[202] C. Wang, C. You, K. Rong, C. Shen, F. Yang, S. Li, An S-scheme MIL-101(Fe)-on-BiOCl heterostructure with oxygen vacancies for boosting photocatalytic removal of Cr(VI), Acta Phys. Chim. Sin. (2023) 2307045, https://doi.org/10.3866/PKU.WHXB202307045.
[203] K.O. Yoro, M.O. Daramola, CO2 emission sources, greenhouse gases, and the global warming effect, in: Adv. Carbon Capture, Elsevier, 2020, pp. 3–28, https://doi.org/10.1016/B978-0-12-819657-1.00001-3.
[204] S. Nahar, M. Zain, A. Kadhum, H. Hasan, M. Hasan, Advances in photocatalytic CO2 reduction with water: a review, Materials 10 (2017) 629, https://doi.org/10.3390/ma10060629.
[205] Z. Miao, Y. Zhang, N. Wang, P. Xu, X. Wang, BiOBr/Bi2S3 heterojunction with S-scheme structureand oxygen defects: in-situ construction and photocatalytic behavior for reduction of CO2 with H2O, J. Colloid Interface Sci. 620 (2022) 407–418, https://doi.org/10.1016/j.jcis.2022.04.035.
[206] C. Yan, M. Xu, W. Cao, Q. Chen, X. Song, P. Huo, W. Zhou, H. Wang, Fabricated S-scheme BiOBr/Cu2O heterojunction photocatalyst for adjusting conversion of CO2 to CH4, J. Environ. Chem. Eng. 11 (2023) 111479, https://doi.org/10.1016/j.jece.2023.111479.
[207] J. Ma, M. Hu, D. Li, J. Fan, Q. Bi, Black phosphorus coupled bismuth chloride oxide nanocomposites for efficient photocatalytic CO 2 reduction, New J. Chem. 46 (2022) 21762–21770, https://doi.org/10.1039/D2NJ04549D.
[208] Z. Wang, B. Cheng, L. Zhang, J. Yu, H. Tan, BiOBr/NiO S-scheme heterojunction photocatalyst for CO 2 photoreduction, Sol. RRL 6 (2022) 2100587, https://doi.org/10.1002/solr.202100587.
[209] J. Wu, K. Li, S. Yang, C. Song, X. Guo, In-situ construction of BiOBr/Bi2WO6 S-scheme heterojunction nanoflowers for highly efficient CO2 photoreduction: regulation of morphology and surface oxygen vacancy, Chem. Eng. J. 452 (2023) 139493, https://doi.org/10.1016/j.cej.2022.139493.
[210] X. Guan, X. Zhang, C. Zhang, R. Li, J. Liu, Y. Wang, Y. Wang, C. Fan, Z. Li, Original self-assembled S-scheme BiOBr-(0 0 1)/Bi2SiO5/Bi heterojunction photocatalyst with rich oxygen vacancy for boosting CO2 reduction performance, J. Colloid Interface Sci. 644 (2023) 426–436, https://doi.org/10.1016/j.jcis.2023.04.097.
[211] W. Li, X. Li, X. Fu, Z. Lou, Y. Zhu, Y. Zhang, Photo-induced conversion of type-II CoPc/BiOBr-NSs to S-scheme heterostructure for boosting CO2 photoreduction, Chem. Eng. J. 451 (2023) 138932, https://doi.org/10.1016/j.cej.2022.138932.
[212] Z. Zhang, L. Li, Y. Jiang, J. Xu, Step-scheme photocatalyst of CsPbBr3 quantum dots/BiOBr nanosheets for efficient CO2 photoreduction, Inorg. Chem. 61 (2022) 3351–3360, https://doi.org/10.1021/acs.inorgchem.2c00012.
[213] H. Jiang, W. Wang, L. Sun, T. Kong, Z. Lu, H. Tang, L. Wang, Q. Liu, Boosting photocatalytic CO2 reduction by tuning photogenerated carrier kinetics in two-dimensional WOx/BiOCl S-scheme heterojunction with oxygen vacancies, J. Catal. 416 (2022) 1–10, https://doi.org/10.1016/j.jcat.2022.10.015.
[214] Z. Zhang, R. Guo, J. Tang, Y. Miao, J. Gu, W. Pan, Fabrication of Bi-BiOCl/MgIn2S4 heterostructure with step-scheme mechanism for carbon dioxide photoreduction into methane, J. CO2 Util. 45 (2021) 101453, https://doi.org/10.1016/j.jcou.2021.101453.
[215] K. Wang, T. Sun, H. Ma, R.-J. You, Z.-H. He, J.-G. Chen, H. Wang, W. Wang, Y. Yang, L. Wang, Z.-T. Liu, In-situ construction of S-scheme heterojunction nanoflowers by In2O3-regulated the growth of metal Bi and oxygen vacancy on BiOCl surface for boosting photocatalytic CO2 reduction, Sep. Purif. Technol. 340 (2024) 126786, https://doi.org/10.1016/j.seppur.2024.126786.
[216] Z. Wang, B. Cheng, L. Zhang, J. Yu, Y. Li, S. Wageh, A.A. Al-Ghamdi, S-Scheme 2D/2D Bi2MoO6/BiOI van der Waals heterojunction for CO2 photoreduction, Chin. J. Catal. 43 (2022) 1657–1666, https://doi.org/10.1016/S1872-2067(21)64010-X.
[217] Y. Guo, C. Qi, B. Lu, P. Li, Enhanced hydrogen production from water splitting by Sn-doped ZnO/BiOCl photocatalysts and Eosin Y sensitization, Int. J. Hydrogen Energy 47 (2022) 228–241, https://doi.org/10.1016/j.ijhydene.2021.10.014.
[218] G.J. Lee, Y.C. Zheng, J.J. Wu, Fabrication of hierarchical bismuth oxyhalides (BiOX, X = Cl, Br, I) materials and application of photocatalytic hydrogen production from water splitting, Catal. Today 307 (2018) 197–204, https://doi.org/10.1016/j.cattod.2017.04.044.
[219] C. Zhou, C. Jiang, R. Wang, J. Chen, G. Wang, CdS microparticles decorated with Bi0/BiOI nanosheets for visible light photocatalytic hydrogen evolution, ACS Appl. Nano Mater. 4 (2021) 4939–4947, https://doi.org/10.1021/acsanm.1c00473.
[220] L. Zhang, W. Wang, S. Sun, D. Jiang, E. Gao, Selective transport of electron and hole among {001} and {110} facets of BiOCl for pure water splitting, Appl. Catal. B Environ. 162 (2015) 470–474, https://doi.org/10.1016/j.apcatb.2014.07.024.
[221] L. Ye, X. Jin, Y. Leng, Y. Su, H. Xie, C. Liu, Synthesis of black ultrathin BiOCl nanosheets for efficient photocatalytic H2 production under visible light irradiation, J. Power Sources 293 (2015) 409–415, https://doi.org/10.1016/j.jpowsour.2015.05.101.
[222] J. Li, G. Zhan, Y. Yu, L. Zhang, Superior visible light hydrogen evolution of Janus bilayer junctions via atomic-level charge flow steering, Nat. Commun. 7 (2016) 1–9, https://doi.org/10.1038/ncomms11480.
[223] J. Shang, W. Hao, X. Lv, T. Wang, X. Wang, Y. Du, S. Dou, T. Xie, D. Wang, J. Wang, Bismuth oxybromide with reasonable photocatalytic reduction activity under visible light, ACS Catal. 4 (2014) 954–961, https://doi.org/10.1021/cs401025u.
[224] C.J. Chang, C.L. Huang, Y.H. Yu, M.C. Teng, C.L. Chiang, Y.G. Lin, Electron transfer dynamics and enhanced H2 production activity of hydrangea-like BiOBr/Bi2S3-based photocatalysts with Cu-complex as a redox mediator, Appl. Surf. Sci. 576 (2022) 151870, https://doi.org/10.1016/j.apsusc.2021.151870.
[225] J. Lu, Y. Chen, L. Li, X. Cai, S. Zhong, L. Wu, J. Chen, S. Bai, Facet engineering on the interface of BiOCl-PbS heterostructures for enhanced broad-spectrum photocatalytic H2 production, Chem. Eng. J. 362 (2019) 1–11, https://doi.org/10.1016/j.cej.2018.12.130.
[226] C.J. Chang, Y.G. Lin, P.Y. Chao, J.K. Chen, AgI-BiOI-graphene composite photocatalysts with enhanced interfacial charge transfer and photocatalytic H 2 production activity, Appl. Surf. Sci. 469 (2019) 703–712, https://doi.org/10.1016/j.apsusc.2018.11.081.
[227] Y. Zhao, X. Huang, X. Tan, T. Yu, X. Li, L. Yang, S. Wang, Fabrication of BiOBr nanosheets@TiO 2 nanobelts p-n junction photocatalysts for enhanced visible-light activity, Appl. Surf. Sci. 365 (2016) 209–217, https://doi.org/10.1016/j.apsusc.2015.12.249.
[228] B. Zhang, X. Hu, E. Liu, J. Fan, Novel S-scheme 2D/2D BiOBr/g-C3N4 heterojunctions with enhanced photocatalytic activity, Chin. J. Catal. 42 (2021) 1519–1529, https://doi.org/10.1016/S1872-2067(20)63765-2.
[229] Y. Xi, W. Chen, W. Dong, Z. Fan, K. Wang, Y. Shen, G. Tu, S. Zhong, S. Bai, Engineering an interfacial facet of S-scheme heterojunction for improved photocatalytic hydrogen evolution by modulating the internal electric field, ACS Appl. Mater. Interfaces 13 (2021) 39491–39500, https://doi.org/10.1021/acsami.1c11233.
[230] B. Zhang, D. Wang, S. Jiao, Z. Xu, Y. Liu, C. Zhao, J. Pan, D. Liu, G. Liu, B. Jiang, Y. Li, L. Zhao, J. Wang, TiO2-X mesoporous nanospheres/BiOI nanosheets S-scheme heterostructure for high efficiency, stable and unbiased photocatalytic hydrogen production, Chem. Eng. J. 446 (2022) 137138, https://doi.org/10.1016/j.cej.2022.137138.